

**TUNING THE OPTICAL PROPERTIES OF NANOSCALE MATERIALS ON
SURFACES THROUGH CONTROLLED EXCHANGE REACTIONS ON CADMIUM
SELENIDE QUANTUM DOTS AND PATTERNING OF GOLD AND QD
NANOPARTICLE ARRAYS**

A Dissertation

by

ARIKA PRAVITASARI

Submitted to the Office of Graduate and Professional Studies of
Texas A&M University
in partial fulfillment of the requirements for the degree of

DOCTOR OF PHILOSOPHY

Chair of Committee,	James D. Batteas
Committee Members,	Dong Hee Son
	Emile A. Schweikert
	Jaime Grunlan
Head of Department,	David H. Russell

December 2013

Major Subject: Chemistry

Copyright 2013 Arika Pravitasari

ABSTRACT

This work focused on the integration of CdSe quantum dots (QDs) and Au nanoparticles (NPs) as building blocks for the development of quantum dot and plasmonic based optical and sensing devices. The manipulation of nanomaterials was performed to tune their surface and optical properties to study their fundamental chemical and physical processes as well as their applications.

First, the cation exchange reactions between CdSe QDs and Ag^+ cations were explored as the surface properties of the QDs were altered. The surface properties of CdSe QDs were tuned by local exposure of laser through photopatterning. The CdSe QDs with different surface properties altered by photopatterning were then exposed to a solution of increasing Ag^+ concentrations. The decrease in the photoluminescence intensity of CdSe QDs were monitored and used as an indication for the cation exchange reactions taking place. Photoluminescence data confirmed that the cation exchange reactions exhibited different efficiencies for QDs that were photo-altered in comparison to pristine QDs.

The second area of the study employed the use of directed assembly to fabricate pattern arrays of Au NPs. Fabrication of metallic nanostructure arrays using polystyrene (PS) microspheres often required the use of photo-resist, chemical etching and metal evaporation processes, here they were used to direct the assembly of colloidal Au nanoparticles (NPs) by simple evaporative processes. This created an inexpensive and

simple bench-top method for bottom-up fabrication of metallic nanostructure arrays. Optimum parameter for the formation of uniform Au nanoring arrays was achieved by controlling the relative humidity (RH) and the relative concentration of Au NPs to PS microspheres. The fabricated Au nanostructure arrays serve as great platforms not only for future applications in plasmonic based sensing and optical devices but also for the fundamental studies of their localized surface plasmon resonance (LSPR). An alternative method of patterning, a combination between the use of a self-assembled monolayer (SAM) molecular linker and PS mask fabricated via polydimethylsiloxane (PDMS) micro-stamp was also discussed briefly.

Particle lithography is a versatile method and can be used to fabricate pattern array of different nanomaterials with similar surface affinities. It was then modified to reduce the non-specific binding of CdSe QDs forming uniform nanoring arrays. The photoluminescence of the fabricated CdSe nanoring arrays was then altered to locally tune their surface and optical properties. This allowed for the post-fabrication surface modification of each nanoring for the creation of CdSe nanoring arrays of different surface and optical properties.

DEDICATION

To my parents, Arijanto Eddy Pratomo and Dwi Koes Hendaryani,
and to my two sisters: Desiani Poppy Enggina and Stefiana Filia Astari,
thank you for the support and encouragement.

ACKNOWLEDGEMENTS

First I would like to give thank and praise to God for all the opportunities and blessings that He has given me. I could not have gotten through this process without my faith and trust in Him. It has been a very humbling yet amazing experience.

I would also like to thank both of my parents for their support and sacrifices. I very much appreciate their sacrifices they made to make sure I received the best education so I could have a bright future. I am very grateful for the love and support I have received from my mom, dad and sisters.

I would like to thank my advisor James Batteas for his support and guidance. I would also like to thank Agustin Diaz for all of his advice and constant encouragements, and Jixin Chen for his mentoring, suggestions and insights on the project. Also for the current and past members of Batteas' research group for the camaraderie and friendship. I feel blessed to have such supporting and encouraging co-workers.

To my friends for hanging there with me within the past six years or so, Diana, Francisco, Jessica, Samae, Tinh, and Argentina, thank you so much. Each and every one of you played a crucial role in my life and I can't thank you all enough for it.

I appreciate every one of you that were involved in the projects in this dissertation. This has been a long and very much rewarding journey.

TABLE OF CONTENTS

	Page
ABSTRACT	ii
DEDICATION	iv
ACKNOWLEDGEMENTS	v
TABLE OF CONTENTS	vi
LIST OF TABLES	xiv
CHAPTER	
I INTRODUCTION.....	1
1.1 Purpose	1
1.2 General Background.....	4
1.3 Nanofabrication by Conventional and Unconventional Method of Lithography	5
1.4 Immobilization of Nanomaterials on Supported Substrates	8
1.5 Cadmium Selenide (CdSe) QDs.....	13
1.6 Metallic Au Nanoparticles	15
1.7 Atomic Force Microscopy (AFM)	20
1.8 Confocal Microscopy	23
II INFLUENCE OF SURFACE LIGANDS AND OXIDATION ON SILVER (I) CATION EXCHANGE IN CADMIUM SELENIDE QUANTUM DOTS.....	25
2.1 Introduction	25
2.2 Experimental Method.....	28
2.3 Enhanced CdSe Photoluminescence by Laser Photolithography	33
2.4 Locally Photobrightened CdSe QDs Sensitivity to Their Local Environment	38

CHAPTER

2.5	Photoluminescence Quenching on the Locally Photobrightened CdSe QDs by Ag ⁺	45
2.6	Following the Photoluminescence Quenching of CdSe QDs by Using Locally Patterned Array in a Microfluidic Channel	51
2.7	Cation Exchange in CdSe QDs by Ag ⁺	59
2.8	Locally Photobrightened CdSe QDs on the Cation Exchange with Ag ⁺	61
2.9	Conclusions	68
III	PATTERNING OF GOLD NANOPARTICLE BASED ARRAYS USING METHODS OF DIRECTED ASSEMBLY BY CHEMICAL FORCES	70
3.1	Introduction	70
3.2	Patterning Au Nanostructure Arrays via Particle Lithography	70
3.3	Patterning Array of Au NPs via 3-Aminopropyltriethoxy Silane (APTES) by PS Stamp	91
3.4	Conclusions	97
IV	EFFECT OF SURFACE WETTING ON THE FORMATION OF CdSe QUANTUM DOT RINGS AND THE FABRICATION OF MULTICOLOR ARRAY CdSe RINGS	99
4.1	Introduction	99
4.2	Experimental Method	101
4.3	Step by Step Surface Wetting for a Cleaner CdSe QDs Nanoring Arrays	103
4.4	Employing Laser Photolithography to the CdSe QDs Nanoring Arrays	108
4.5	Binding of a Thiol Tethered Porphyrin to the CdSe Nanorings	110
4.6	Conclusions	113
V	SUMMARY AND OUTLOOK	115
5.1	Summary	115
5.2	Outlook	118
	REFERENCES	123

LIST OF FIGURES

	Page
Figure 1. 1 Schematic of conventional lithography methods by photolithography and e-beam lithography.....	7
Figure 1. 2 Schematic of layer-by-layer assembly of negatively-charged CdS QDs supported on a metal/ glass/ plastic substrate by electrostatic interaction between the QDs and polycations.....	9
Figure 1. 3 Schematic for the adsorption of citrate-stabilized Au NPs into a SiO ₂ substrate by APTES and MPTES SAM.....	11
Figure 1. 4 Schematic illustration of particle lithography displaying a hexagonal closed-pack array of self-assembled nanospheres as masks, and representative AFM image of Ag nanoparticles after thermal evaporation of Ag and masks removal.....	12
Figure 1. 5 Density of states in semiconductor materials as a function of dimension....	14
Figure 1. 6 Schematic of localized surface plasmon resonance (LSPR).....	15
Figure 1. 7 Electromagnetic field enhancement image of 100 nm Ag nanosphere.....	17
Figure 1. 8 An energy-level diagram describing the plasmon hybridization in metallic nanorings resulting from the interaction between the sphere and cavity plasmons.....	19
Figure 1. 9 Schematic of an AFM working principle. Inset shows topographical AFM image of a CdSe QDs immobilized on a substrate.	20
Figure 1. 10 Schematic of confocal fluorescence microscopy comparing the in-focus and out-of-focus signal from the sample.	24
Figure 2. 1 (A) TEM and (B) high resolution (HR-TEM) images of 3.6 nm CdSe QDs and their particle size distribution.....	30

Figure 2. 2 (A) Schematic of laser photolithography on thin film of CdSe QDs immobilized on Si (100). (B) Photoluminescence intensity and (C) photoluminescence peak maxima images of the CdSe QDs after laser photolithography performed with decreasing laser raster speed from 4 to 0.1 $\mu\text{m/s}$.	35
Figure 2. 3 Photoluminescence time series studies of 11-MUA capped CdSe QDs taken (A) in air (B) with free 5 mM 11-MUA dissolved in ethanol performed by the same laser power of $\sim 20 \mu\text{W}$.	37
Figure 2. 4 Photoluminescence images of CdSe QDs. (A) Shortly after lithography (B) after ethanol rinsing and (C) after water rinsing of the same area and the corresponding photoluminescence spectra of the (D) photobrightened box area and (E) background.	41
Figure 2. 5 Photoluminescence images of CdSe QDs. (A) Shortly after lithography (B) after water rinsing of the same area and the corresponding photoluminescence spectra of the (C) photobrightened box area and (D) background	42
Figure 2. 6 Photoluminescence images of CdSe QDs (A) after ethanol rinsing followed by five consecutive scans and the corresponding photoluminescence spectra (B) of the photobrightened box area and (C) background.	44
Figure 2. 7 Schematic of the photoluminescence measurement where the micro cover glass containing the CdSe QDs is set facing down on top of a PDMS well containing the different concentrations of AgNO_3 .	46
Figure 2. 8 Photoluminescence image of CdSe QDs (A) shortly after photolithography and imaged in ethanol (B) after the exposure of increasing concentrations of AgNO_3 and imaged in $1 \mu\text{M AgNO}_3$. (C) Photoluminescence spectra of averaged intensity from the background area as the concentration of Ag^+ is increased.	48
Figure 2. 9 Quenching plot of CdSe QDs as a function of Ag^+ concentrations.	50
Figure 2. 10 Schematic of the experimental set-up. The CdSe QDs thin film was deposited on a micro cover glass slide inside a microfluidic channel. Photolithography was performed with a 488 nm Argon ion laser with a power of $\sim 115 \mu\text{W}$, while the confocal fluorescence imaging using was performed with a laser power of $\sim 20 \mu\text{W}$.	52

- Figure 2. 11 (A) Photopatterned array script with a range of patterning speeds used to create patterns in the CdSe QDs with different surface properties. (B) Photoluminescence spectra of CdSe QDs after patterning. The background is an unpatterned area of the pristine CdSe film, while lines 1, 2, 3 are the areas of CdSe QDs that underwent patterning with different scan rates of 7 $\mu\text{m/s}$, 1 $\mu\text{m/s}$ and 0.1 $\mu\text{m/s}$ respectively.54
- Figure 2. 12 (A) Photoluminescence images of thin film CdSe QDs immobilized inside a microfluidic channel after patterning at different rates with increasing AgNO_3 concentrations, PL intensity images on the different Ag^+ concentrations are scaled individually for a better image contrast. (B) The photoluminescence spectra of the background with the different AgNO_3 concentration.....56
- Figure 2. 13 Control experiment showing (A) fluorescence images of CdSe QDs inside a microfluidic channel on 7 different regions of lithography imaged under ethanol with $\sim 20 \mu\text{W}$ 488 nm Ar ion laser, (B) average fluorescence intensity spectra of the images in (A).57
- Figure 2. 14 (A) Normalized photoluminescence spectra of CdSe QDs with the presence of AgNO_3 normalized at the CdSe excitonic peak. (B) Plot of the normalized photoluminescence intensity of the small shoulder at 650 nm with increasing concentration of AgNO_358
- Figure 2. 15 AFM AC mode topography images and cross section profiles of (A). Si-PDADMAC. (B) Si-PDADMAC-CdSe 11-MUA capped. (C) Si-PDADMAC-CdSe 11-MUA capped after 100 μM AgNO_360
- Figure 2. 16 XPS spectra of CdSe QDs film in the Cd(3d), Ag (3d), Se(3d), S(2p) regions of CdSe QDs A) After exposure to pure water (upper row) and B) 100 μM Ag^+61
- Figure 2. 17 Quenching plots of the CdSe QDs photoluminescence by AgNO_3 . The background is given by the unmodified CdSe film, while lines 1 through 3 are CdSe QDs that have been photo-oxidized with a laser power of $\sim 115 \mu\text{W}$ at speeds of 7, 1, and 0.1 $\mu\text{m/s}$63
- Figure 2. 18 XPS spectra of Se(3d) before and after UV-ozone treatment. The shoulder signal centered at 58 eV is corresponding to the formation of SeO_2 . 64

Figure 2. 19 Ratio of Cd/Ag and Ag/Se calculated from the XPS data of CdSe QDs after partial cation exchange with 10 μM AgNO_3 for samples without UV-ozone oxidation, with 2 minutes of UV-ozone oxidation (photobrightened), and with 7 minutes of UV-ozone oxidation (oxidized).	66
Figure 2. 20 Photoluminescence intensity spectra normalized to the I_0 at λ_{max} peak position of the different lines of CdSe QDs with increasing AgNO_3 concentrations.	67
Figure 3. 1 (A) Optical image and (B) AFM image. Of the self-assembly of 2.5 μm in diameter polystyrene microspheres dropcasted on micro cover glass #2.	75
Figure 3. 2 Schematic of particle lithography. (1) A 1:1 mixture of Au NPs and PS MS dispersed in water was dropcasted on a PVP modified glass substrate; (2) as the mixture is dried the PS MS self-assembled into a close packed hexagonal array with the smaller Au NPs arranging themselves around the larger microspheres; (3) scotch tape is then used to peel the larger microspheres, (4) leaving the Au nanostructure arrays on the substrate.	76
Figure 3. 3 (A) UV-visible spectra of Au NPs stabilized with 11-MUA and its localized surface plasmon resonance (LSPR) at 525 nm. (B) TEM images of the 20 nm Au NPs.	77
Figure 3. 4 Au nanoring arrays fabricated using particle lithography.	78
Figure 3. 5 Atomic Force Microscopy (AFM) images of Au nanoring structures with concentration of 40×10^{11} Au NPs/mL under 45% RH and their corresponding cross sections before rinsing treatment with ethanol.	79
Figure 3. 6 AFM AC topography image showing Au NPs donuts array on PVP modified glass substrate.	81
Figure 3. 7 AFM images of Au nanodnut arrays using a lower Au NPs concentration of 7×10^{11} Au NPs/ml at 65% RH before rinsing with ethanol.	82
Figure 3. 8 AFM image from AFM scratch experiment showing the thickness of the PVP polymer layer as shown in the corresponding cross sections graph with an average of 8 ± 1 nm.	82
Figure 3. 9 AFM image of nanodonut structure assembled on bare glass without PVP after ethanol rinse.	83

	Page
Figure 3. 10 Schematic using a hard sphere contact model approximation to calculate r_{ring}	84
Figure 3. 11 Schematic of Au nanodonut arrays formation showing Au NPs partially embedded in the PVP matrix.....	86
Figure 3. 12 Schematic diagram showing the forces involved in dragging the Au nanoparticle to polystyrene spheres. Note that the drawing is not to scale. Moreover, there is almost certainly a hydration layer that covers the entire hydrophilic Au nanoparticle, which has not been explicitly drawn.	87
Figure 3. 13 AFM images of Au nanostructures as the humidity and Au NPs concentrations are varied.	89
Figure 3. 14 (A) Nanoring structure modeled by MATLAB MNPBEM and (B) its corresponding calculated LSPR.....	91
Figure 3. 15 Schematic of the fabrication of Au NPs patterned array using PS stamp via APTES.	95
Figure 3. 16 AFM AC image of PS stamp with its corresponding cross section.	96
Figure 3. 17 AFM image of Au NPs array fabricated by PS stamp via APTES molecular linker.	97
Figure 4. 1 AFM images of CdSe QDs ring on a PVP modified glass substrate.	104
Figure 4. 2 Photoluminescence images of CdSe nanoring arrays on a PVP modified glass substrate.	104
Figure 4. 3 Schematic experimental procedures of the step-by-step surface wetting for the modified particle lithography method.....	106
Figure 4. 4 AFM images of CdSe QDs nanorings fabricated using the modified particle lithography method by employing condensation process.....	106
Figure 4. 5 (A) Photoluminescence image of CdSe nanoring arrays and (B) photoluminescence spectra of CdSe nanorings and background signal.	107
Figure 4. 6 (A) AFM image and (B) photoluminescence image of CdSe nanodots array due to overwetting.	108

Figure 4. 7 Photoluminescence peak emission of CdSe nanorings area. (A) Before and (B) after laser photolithography with increasing laser dwelling time. (C) Photoluminescence spectra of CdSe rings before photolithography (dark blue at 0.0s) and after photolithography with increasing laser dwelling time (0.1, 0.3, 0.6, 1.2 s integration time) showing the blue shift of the photoluminescence peak.	109
Figure 4. 8 Chemical structure of a free base porphyrin TPy ₃ PF ₄ -SC ₅ SH.	110
Figure 4. 9 Photoluminescence intensity and peak position images of CdSe nanoring arrays before and after lithography, and after immersion to TPy ₃ PF ₄ -SC ₅ SH.	112
Figure 4. 10 (A) Photoluminescence intensity image of TPy ₃ PF ₄ -SC ₅ SH on CdSe nanoring arrays. (B) Photoluminescence spectra of TPy ₃ PF ₄ -SC ₅ SH and CdSe nanoring arrays. Image (A) was taken by integrating the photoluminescence signal from 630-730 nm.	113
Figure 5. 1 AFM contact mode images of Au nanoring structure before and after AFM nanoshaving.	120
Figure 5. 2 Au nanostructure arrays after AFM nanoshaving, showing different morphologies of the structures as the individual ring is partitioned into an increasing number of segments.	121

LIST OF TABLES

	Page
Table 2. 1 XPS table of the ratio of elemental analysis of pristine CdSe QDs film, CdSe QDs after partial cation exchange with 10 μM AgNO_3 with varying UV ozone exposure time, and CdSe QDs after complete exchange with 100 μM AgNO_3	65
Table 3. 1 Au nanorings and nanodunuts dimensions tabulated from AFM images, units are in nm.	84

CHAPTER I

INTRODUCTION

1.1 Purpose

The studies in this dissertation focus on the development of nanomaterials specifically cadmium selenide quantum dots (CdSe QDs) and Au nanoparticles (NPs), as building blocks for designing QD and plasmonic-based devices for future use in sensing, and optical applications. This dissertation will discuss the integration of these nanomaterials on supported substrates by different methods including: 1) thin film deposition via polyelectrolytes, 2) self-assembled monolayer (SAM) of a molecular linker, and 3) particle lithography. Also discussed will be the exploitation of the nanomaterials' physical properties and a basic understanding of the mechanism behind those properties with respect to their potential application.

The first method of immobilization discussed above utilized the layer-by-layer assembly of a water-soluble, 11-mercaptopundecanoic acid (11-MUA) capped CdSe QDs, and a positively charged polyelectrolytes poly(diallyldimethylammonium chloride) (PDDA) modified substrate. The electrostatic interaction between the negatively charged carboxylic acid group from the native ligand, and the positively charged PDDA stabilizes the QDs on the substrate.^{1, 2} The next method explored the use of a SAM of 3-aminopropyltriethoxy silane (APTES) to immobilize citrate-stabilized Au NPs. The interaction between the positive charges of the protonated amine and the negative

charges of the citrate was used to immobilize the Au NPs on an APTES modified substrate.^{2,3} Lastly, the use of polystyrene microspheres (PS MS) to direct the assembly of Au NP and CdSe QD arrays will also be discussed. Brief introduction on each method described above is discussed in more detail in the next section of this chapter.

Chapter II will discuss the use of CdSe QDs for a highly sensitive Ag^+ detection by exploiting cation exchange reactions in CdSe. The cation exchange reactions of CdSe QDs by Ag^+ , followed by the decrease of the photoluminescence intensity, was monitored by confocal fluorescence microscopy and confirmed by X-ray photoelectron spectroscopy (XPS). In this chapter, the surface properties of CdSe QDs were altered by photolithography technique, utilizing a 488 nm Ar-ion. The changes in the efficiency of cation exchange reactions were found to be influenced by the surface properties of the nanocrystals and will be discussed in detail.

Chapter III centers on methods to fabricate Au NP array by directed assembly by manipulating surface forces and surface chemistry. In this chapter, two different methods will be discussed. The first is by particle lithography. Here, the experimental conditions such as the humidity and the relative concentration of Au NPs to polystyrene microspheres (PS MS) were altered. It was found that the formation of the nanostructures by particle lithography was affected. The second used that combined the use of a self-assembled monolayer (SAM) of 3-aminopropyltriethoxy silane (APTES) and microcontact printing with polydimethylsiloxane (PDMS) and PS mask to direct the assembly of the Au NPs. Both of these methods were shown to be great alternatives for

the patterning of Au nanostructures for potential use in sensing and surface enhanced Raman spectroscopy (SERS) studies.

Chapter IV focuses on the modification of particle lithography technique by the incorporation of a condensation method, to reduce the non-specific binding of CdSe QDs, for the formation of a 2-D array of CdSe QDs nanorings, and the use of laser photolithography to manipulate the emission color of the individual rings. In this chapter, the photolithography technique described previously in Chapter II was performed on the prefabricated CdSe nanoring arrays. This allowed for the manipulation of the photoluminescence signal of each CdSe ring. By controlling the laser dwelling time, an array of CdSe nanorings with a range of emission's color was created. This post-synthetic photochemical modification can be foreseen as a more simple and economical ways to pattern QDs with different optical and surface properties on the same platform. This could be beneficial for the development of some QD based devices, such as: QD based light emitting diodes (LED), where each emitted color can be represented by originally the same QDs, tuned individually by photopatterning.

Finally, Chapter V states the summary and future direction of the project. This includes the manipulation of the prefabricated Au nanostructure arrays by atomic force microscopy (AFM) to study how these structural changes would influence their localized surface plasmon resonance (LSPR) property. The junctions between the Au nanostructure created by AFM can serve as hot spots with potential applications in SERS, near infra-red (NIR) surface enhanced spectroscopy. The general introduction of the nanomaterials used in the study, CdSe QDs and Au metallic NPs, the methods of

fabrication used to immobilize these nanomaterials, as well as the characterization techniques used for this study including AFM and confocal microscopy, will be discussed in the next following sections of this chapter. A more detailed introduction of their specific properties, mechanism and potential applications will be discussed in Chapters II-V.

1.2 General Background

The vast development in the field of nanotechnology in the past few decades is spurred by the promising and unique properties that nanomaterials possess when compared to their counterpart bulk materials. Their unique electrical, optical, catalytic properties arise from their nano-scale dimensions. The wide range of nanomaterials used includes: noble metal nanoparticles,^{4, 5} semiconductors,⁶⁻⁹ organic molecules,^{10, 11} polymers^{12, 13} and carbon based materials such as carbon nanotubes and graphene.^{14, 15} Therefore, the potential applications for these materials are limitless. Their applications include: chemical sensing,⁴⁻⁶ plasmonic devices,^{4, 5} transistors and electronics,^{10, 13, 15, 16} photovoltaics,^{8, 17, 18} and bio sensing/ biomedical fields.^{9, 14, 19, 20} Because of that, it is crucial to integrate these nanomaterials for device fabrication.²¹ For the purpose of this dissertation, materials discussed will be CdSe QDs and Au NPs. The synthesis, characterization, self assembly and unconventional lithography of these materials will be discussed in detail for the development of nanomaterial based sensing and optical devices.

Several different surface characterization and analytical techniques were employed for the purpose of this study, such as atomic force microscopy (AFM), confocal fluorescence microscopy, X-ray photoelectron spectroscopy (XPS) and transmission electron microscopy (TEM). The importance and need for these techniques arise from the requirement to fully understand the physical and chemical properties of the nanomaterials incorporated. In this work, the manipulation of nanomaterials' properties at the nano and micro-scale were probed by AFM and confocal fluorescence microscope. To better understand the process, the working principle of those instruments will be discussed in the next sections of this chapter.

1.3 Nanofabrication by Conventional and Unconventional Method of Lithography

Nanofabrication is the process of making functional structures with arbitrary patterns having well defined dimensions to be <100 nm.²¹ The conventional, or well developed, methods for patterning are photolithography and e-beam lithography. Both methods of lithography are similar in a sense that they require the use of a sensitive polymer resist to be exposed by either light or electron beams and the development of the resist with a suitable chemical developer to reveal negative or positive image on the substrate depending on the type of resist (positive or negative) used. Aside from the source of energy used for resist exposure, photolithography requires the use of a mask, while e-beam lithography does not. In e-beam lithography, a scanning electron beam irradiates the surface of the resist sequentially, point by point, through a computer

controlled program where a mask is patterned. Schematic of the basic principle of both methods is shown on Figure 1.1 While optical lithography is reaching the diffraction limit of light, the resolution for e-beam lithography has been reported to make significant progress towards the atomic scale.²² But nonetheless, because these techniques are highly developed and optimized for semiconductor fabrication, the cost of purchasing, installing, and maintaining the tools are still considered costly.²³

The unconventional route to nanofabrication refers to the newly developed or under-developed method of patterning. This method of fabrication is particularly appealing for the use in research, aside from the low-cost factor, it is also more versatile. The conventional method is incompatible with nonstandard problems in fabrication such as patterning nonplanar surfaces, or reactive organic polymers. Therefore, unconventional lithography offers an alternative to create pattern of sensitive materials that are not photoresist such as organic and biological materials, and can be tailored to meet a specific need. Some examples of unconventional lithography methods are: soft lithography, replica molding, microcontact printing, particle lithography and scanning probe lithography (SPL).^{21, 23} Several unconventional lithography methods such as particle lithography, microcontact printing and scanning probe lithography were employed for the purpose of the studies in this dissertation, and will be discussed in detail in the course of this dissertation.

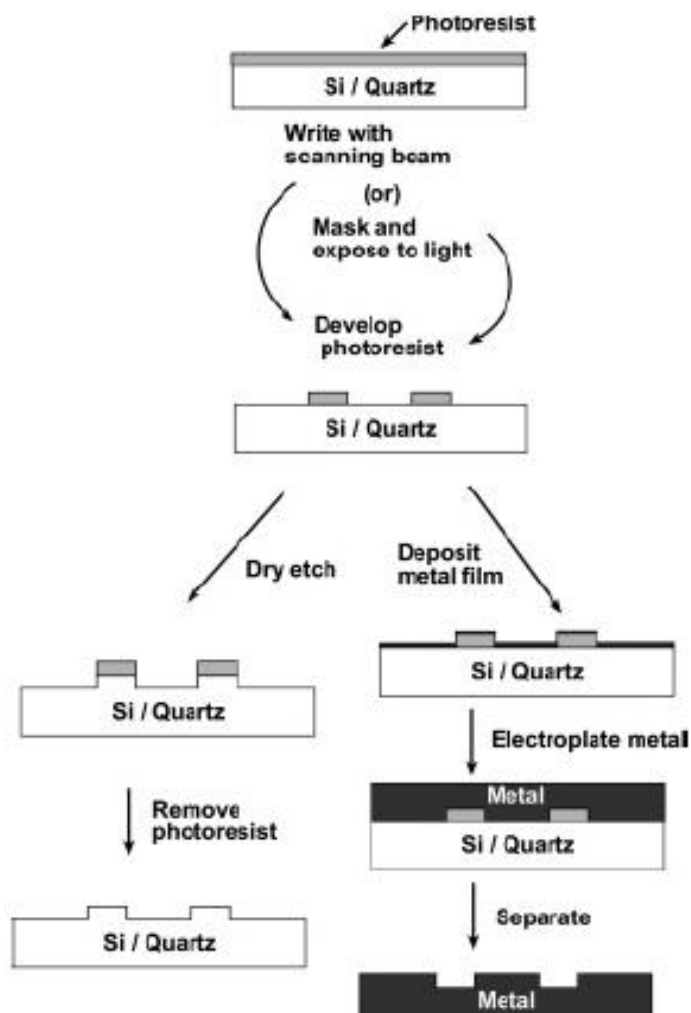


Figure 1. 1 Schematic of conventional lithography methods by photolithography and e-beam lithography. Reprinted from ref [21] with permission of Copyright (2005) from American Chemical Society.

1.4 Immobilization of Nanomaterials on Supported Substrates

The need to immobilize nanomaterials on supported substrates has increased greatly in the past decades along with the development in integrating them into nanomaterials based devices.²¹ Some methods of immobilization include the use of: layer-by-layer assembly,^{1, 2, 24, 25} self-assembled monolayer (SAM) of a molecular linker,^{2, 3, 26-31} microcontact printing,³²⁻³⁵ spin-coating,^{36, 37} dip-coating,^{38, 39} and particle lithography.^{16, 40-43} The stability of the supported nanomaterials on the substrates depends upon the interaction between the surface properties of both the nanomaterials and the substrates. Often times, to induce a strong interaction between the substrates and the adsorbing nanomaterials, surface modifications of either or both materials are needed. In this work, methods utilized for nanomaterials immobilization utilized the layer-by-layer assembly using polyelectrolytes, SAM of a molecular liker, and particle lithography.

1.4.1 Layer-by-Layer Assembly by Polyelectrolytes

In this method of deposition, electrostatic interactions between the polyelectrolytes and the surface of the nanomaterials are the main driving force for the nanomaterials' attachment to the substrate. This method is used commonly to immobilize water-soluble nanomaterials. Depending upon the surface properties of the nanomaterials of interest, whether they bare positive or negative charges, polyelectrolytes baring the opposite charges will be used. Such method is demonstrated on Figure 1.2. Negatively-charged CdS QDs with surface ligands of thiolactic acid

(TLA) and ethylmercaptane (EM), were immobilized by layer-by-layer deposition using a positively-charged polyelectrolytes poly-(diallylammmonium chloride) (PDDA). The structure was expanded by immobilizing altering layers of the polycations, and CdSe QDs. A modification of the polyelectrolytes layer-by-layer assembly method, using both of the positively and negatively-charged polyelectrolytes alternatively to immobilize negatively-charged and water-soluble QDs was also observed in the literatures.^{1,2}

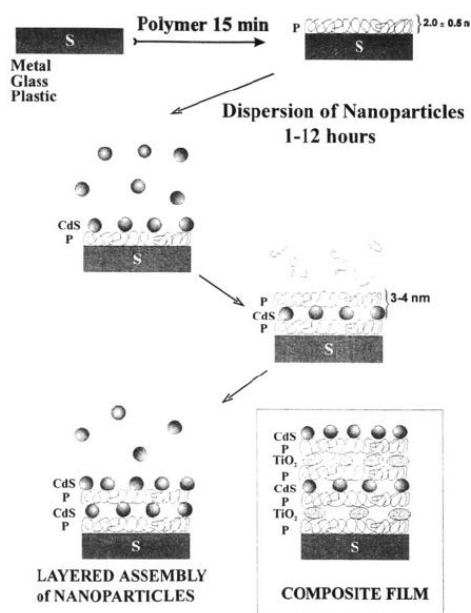


Figure 1. 2 Schematic of layer-by-layer assembly of negatively-charged CdS QDs supported on a metal/ glass/ plastic substrate by electrostatic interaction between the QDs and polycations. Reprinted from ref [24] with permission of Copyright (1995) from American Chemical Society.

1.4.2 Self-Assembled Monolayer (SAM) of a Molecular Linker

Self-assembled monolayer is a very powerful tool for surface modification. It allows for the tailoring of surface properties for adsorption of nanomaterials with complementary surface properties. Their chemical functionality and thermodynamic stability make it versatile yet robust to be utilized for various types of substrates. The formation and characterization of SAM of alkylchlorosilane, alkylalkoxysilanes, and alkylaminosilanes on silanol-terminated surfaces *via* strong Si-O-Si covalent bonds have been widely studied recently.⁴⁴

Molecular linker has been used to immobilize nanomaterials on various supported substrates. Some examples for this include the use of molecular linkers such as: mercaptopropyltrimethoxy silane (MPTMS),²⁶ and mercaptopropionic acid (MPA)²⁷,²⁸ for immobilization of CdSe, CdS QDs and Au NPs,^{29, 30} 3-aminopropyltrimethoxy silane (APTES) for attachment of Au NPs.^{2, 3, 29, 31} Figure 1.3 shows the schematic of the adsorption of citrate-stabilized Au NPs via APTES and mercaptopropyltriethoxy silane (MPTES) molecular linkers.³¹ When APTES was used, the electrostatic interaction between the negatively-charged citrate-stabilized Au NPs and the positively-charged protonated amine group stabilized the substrate-NPs interaction. When MPTES was used, the thiol group at the end of the linker formed covalent bonding to the Au surface. Therefore in this case, the S-Au covalent bond stabilized the substrate-NPs interaction. For the purpose of the study to be discussed later in this dissertation, the first interaction between APTES and Au NPs was used.

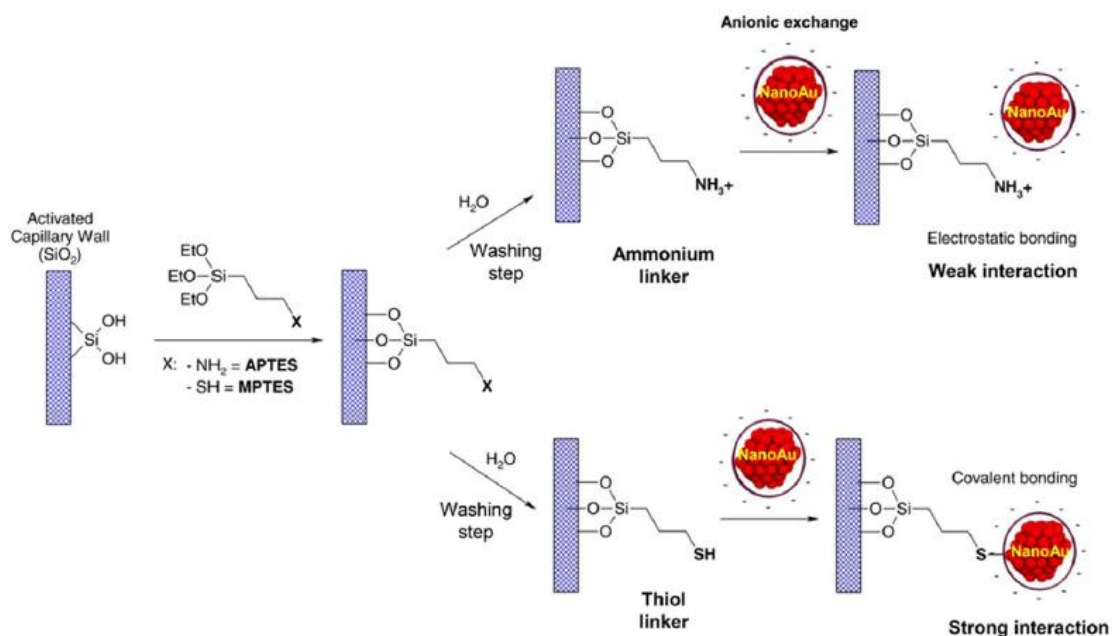


Figure 1. 3 Schematic for the adsorption of citrate-stabilized Au NPs into a SiO₂ substrate by APTES and MPTES SAM. Reprinted from ref [31] with permission of Copyright (2013) from Elsevier.

1.4.3 Particle Lithography

Particle lithography, sometimes known as nanosphere or colloidal lithography is a less expensive nanoscale lithography technique developed as an alternative for electron-beam lithography. As early as 1981, Fischer and Zingsheim introduced the concept by using polystyrene nanospheres as a mask for contact imaging.⁴⁵ In 1982 Deckman and co-workers integrated their concept and used the monolayer of nanospheres as both material deposition and mask.⁴⁶ Van Duyne later coined the term nanosphere lithography (NSL) and expanded the development into a double layer mask

and performed studies and characterization by AFM.⁴² His work is shown in Figure 1.4, where pattern arrays of Ag NPs were created by Ag thermal evaporation using microspheres as masks.

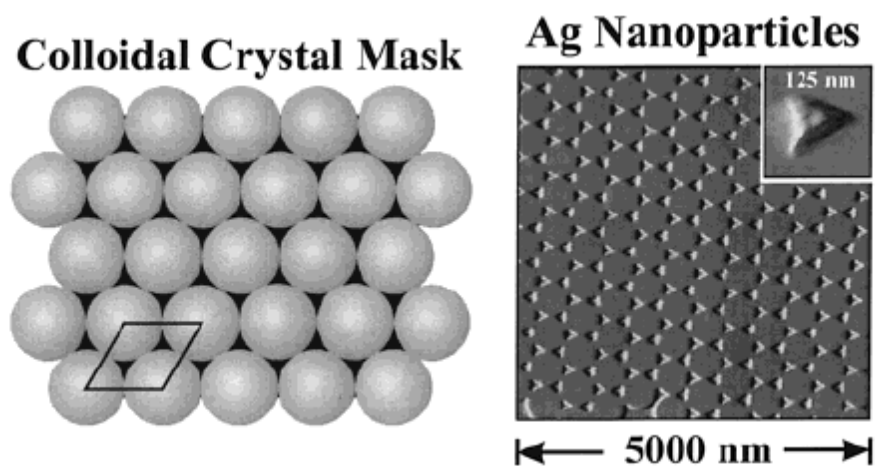


Figure 1. 4 Schematic illustration of particle lithography displaying a hexagonal closed-pack array of self-assembled nanospheres as masks, and representative AFM image of Ag nanoparticles after thermal evaporation of Ag and masks removal. Reprinted from ref [42] with permission of Copyright (2001) from American Chemical Society.

Since then, the use of nanospheres as aids for nanolithography have been used to pattern different morphologies of nanostructures from a wide variety of materials, including the patterning of self assembled monolayers (SAM) and metallic nanostructures.^{16, 40-43} In our recent paper we have demonstrated the use of PS MS as templates for the formation of CdSe QDs ring array.² In this dissertation, particle lithography was used to create Au nanostructure pattern arrays for future study of their

plasmonic properties, and multi-colors CdSe nanoring arrays probed by photolithography using a 488 nm Ar-ion laser.

1.5 Cadmium Selenide (CdSe) QDs

Semiconductor nanocrystals, e.g. quantum dots (QDs), have attracted a great deal of interest over the past decades because of their size dependent optical properties. When the size of the material approaches the exciton Bohr radius, the motion of the electrons and holes are confined spatially to the dimensions of the particle. In quantum dots, electrons are confined in all three dimensions, and creates a discrete atomic-like density of states as depicted in Figure 1.5.⁴⁷ The confinement effect becomes more significant as the radius becomes smaller. As the size of the quantum dots decreases, the energy gap increases, leading to a blue shift of the emission wavelength. This can be explained by a simple particle in the box theory, where the band gap of the QDs is described as:

$$E_{QDs} = E_{bulk} + \frac{\hbar^2 \pi^2}{2R^2} \left(\frac{1}{m_e} + \frac{1}{m_h} \right) - \frac{1.8 e^2}{4 \pi \epsilon_0 \epsilon R} \quad (1)$$

Where \hbar is the reduced Planck constant, R is the radius of the particle, and m_e, m_h is the effective mass for electron and holes, while ϵ and ϵ_0 are the dielectric constants of the solid and medium respectively. From this equation we can see that the band gap of the QDs is that of the bulk material, modified by the quantum approximation of particle in the box. The band gap of semiconductor QDs is therefore inversely proportional to the square of the QDs particle radius. As the size of the QDs increases the term coming from

the particle in the box is less significant resulting in a smaller E_{QDs} . For example, the band gap of CdS QDs can be tuned from 4.5 eV to 2.5 eV as the size of the QDs is varied.⁴⁸

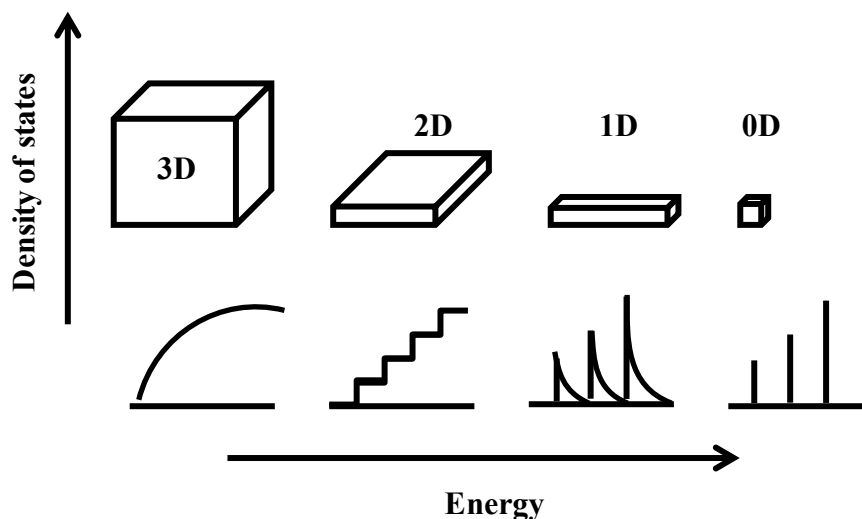


Figure 1. 5 Density of states in semiconductor materials as a function of dimension. Reprinted from ref [47] with permission of Copyright (1996) from Science.

Aside from their size dependent optical properties, QDs are considered material of interest due to their high quantum yield, sharp luminescence peak⁴⁹ and outstanding stability against photobleaching as compared to organic fluorophores.⁵⁰ Applications of QDs have emerged in numerous areas such as bio-imaging,⁹ labeling and sensing,⁵¹ solar cells,^{7, 18, 52} and light emitting diodes (LEDs).^{16, 53-59} CdSe QDs were chosen for the interest of this study. They were synthesized by adapting a well-known solvothermal method.⁶⁰ The QDs were synthesized using CdO as a precursor and were made water

soluble via ligand exchange to bind 11-MUA to the surface. Details on the synthesis of this material will be discussed on chapter II.

1.6 Metallic Au Nanoparticles

Metallic nanoparticles have made significant contributions to the field of nanotechnology because of their localized surface plasmon resonance (LSPR). When light interacts with particles much smaller than the incident wavelength, the oscillations of the conductive surface electrons of the particles are excited by the electromagnetic (EM) field, resulting in a localized surface plasmon at a certain frequency known as LSPR. This is demonstrated in Figure 1.6.

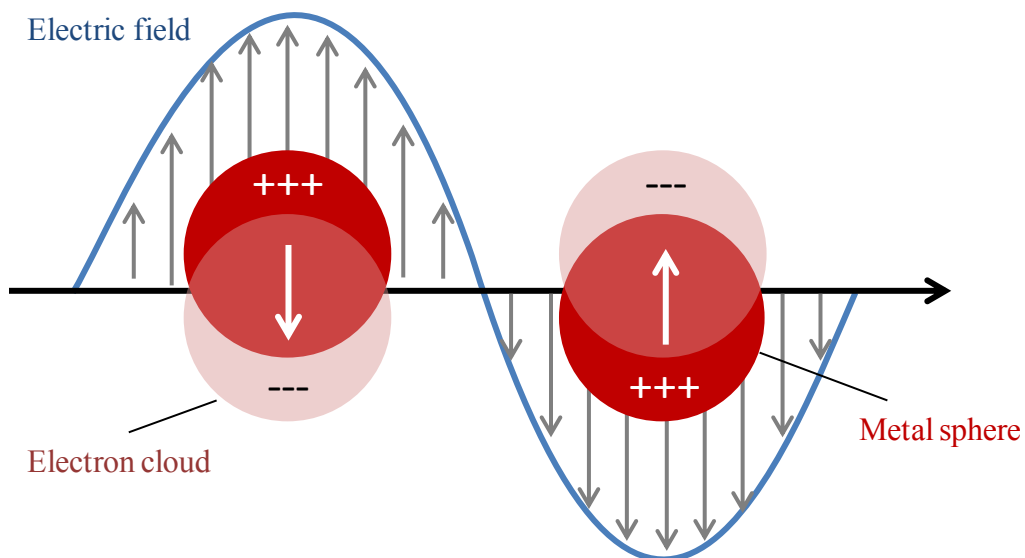


Figure 1. 6 Schematic of localized surface plasmon resonance (LSPR).

For this to occur, the materials need to possess a negative real and small positive imaginary dielectric constant. As stated by Brus:⁶¹

$$P = 4\pi \left(\frac{\varepsilon-1}{\varepsilon-2} \right) a^3 E_0 \quad (2)$$

where P is the total dipole of the particle, E_0 is the electric field of the incoming light wave, a is the particle radius, and ε is the complex, wavelength-dependent particle dielectric constant. Noble metals such as gold and silver have a large negative real part of the dielectric constant, along with a small imaginary part. For example, the value of ε for Ag at 380 nm is: $-2 + 0.2i$. Substituting this value to equation (2) gives rise to a maximum P value. Therefore, at the interface between a noble metal and a dielectric, such as glass or air, localized modes at the metal-dielectric interface can exist.^{61, 62}

LSPR induces a strongly localized evanescent electromagnetic fields, which can be exploited for bringing light down to the nanoscale, thereby overcoming the diffraction limit of light and bridging between the micrometer length scale of optics and the nanometer length scale of nanostructures.⁶³ Therefore, LSPR gives rise to an increased localized magnetic field at the surface of the nanoparticle, but that effect decays rapidly away from the particle as shown on Figure 1.7. The diagram shows an increase in the of electromagnetic field surrounding the 100 nm Ag nanosphere.⁶⁴ This enhanced electromagnetic field is the working foundation for most of plasmonic-based devices. For example, the LSPR of metallic nanoparticles is known to increase the intensity of Raman signals, known as surface enhanced Raman spectroscopy (SERS).^{65, 66} It is also known to increase the photoluminescence intensity of a fluorophore, known as plasmon enhanced fluorescence.^{1, 2} SERS is a phenomenon where the localized surface plasmon

of metallic nanoparticles is shown to increase the Raman intensity the adsorb molecule.^{65, 66} This is due to the enhancement of the dipole induced by the localized surface plasmon. Because of those phenomena the LSPR of metallic nanoparticles has been exploited for the used in chemical as well as biological sensors,⁶⁷ optical devices and medical treatments.¹⁹ The metallic nanoparticles of interest of this study are ~20 nm Au NPs synthesized by a citrate reduction method of a gold precursor salt (HAuCl₄), previously developed by Turkevich.⁶⁸

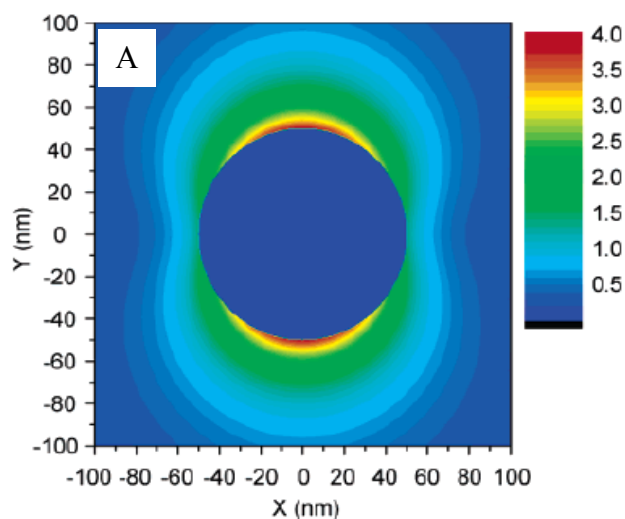


Figure 1. 7 Electromagnetic field enhancement image of 100 nm Ag nanosphere. Reprinted from ref [64] with permission of Copyright (2007) from American Chemical Society.

Link and co-workers showed that near-field coupling of closely spaced nanoparticles in an assembly has shown to produce red-shifted multipolar plasmon modes that were highly polarized. They observed that closely spaced Au NPs arranged in one-dimensional assembly exhibited long-range collective plasmonic properties similar those of metallic nanowires.⁶⁹ In chapter III, the arrangement of closely spaced Au NPs in nanoring arrays assembly will be discussed. The near-field coupling between each Au NP will facilitate the long-range collective surface plasmon, hence it is expected to exhibit the LSPR of nanoring structures. In Au nanoring structures, there is a strong electromagnetic coupling between the inner and outer ring walls when the wall thickness is small compared to the ring radius. Therefore the plasmonics of the metallic nanoring structures can be described as the interaction of “hybridization” of the plasmons of metallic nanostructures of more elementary shapes. The LSPR of metallic nanoring can be described as the interaction between plasmons of nanosphere and cavity as shown in Figure 1.8 with two new resonances, one lower energy of symmetric or “binding” mode, and one occur at a higher energy of anti-symmetric or “anti-bonding” mode.⁷⁰

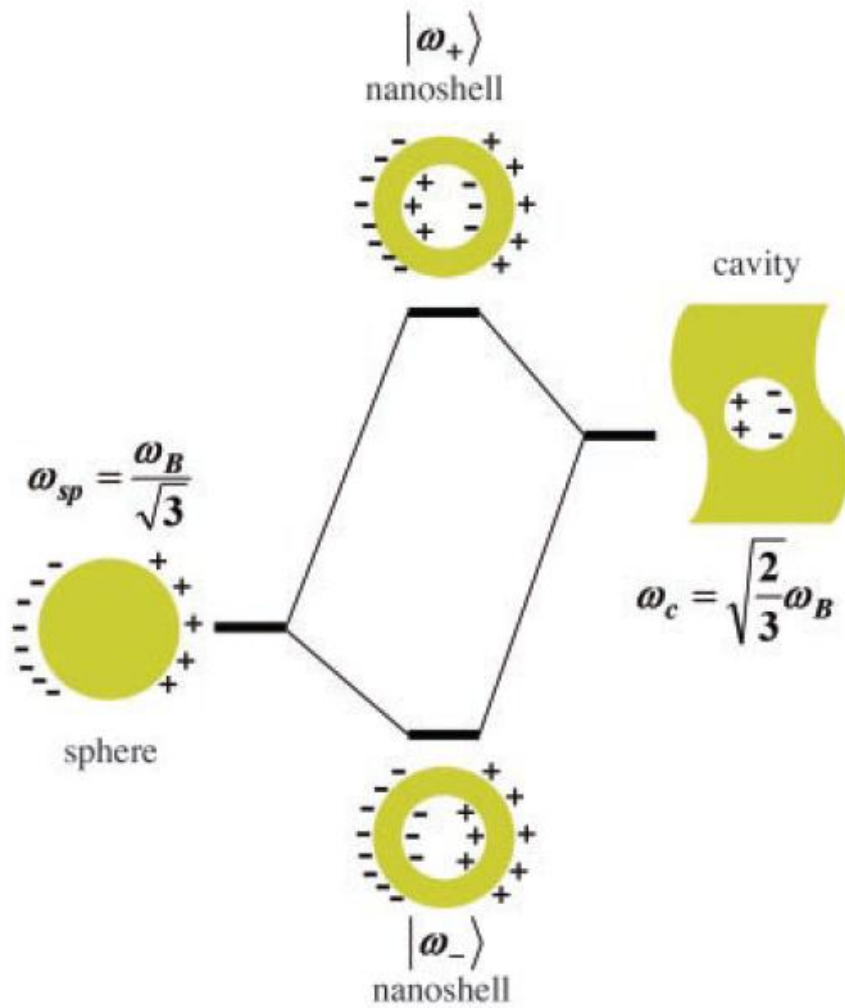


Figure 1. 8 An energy-level diagram describing the plasmon hybridization in metallic nanorings resulting from the interaction between the sphere and cavity plasmons. Reprinted from ref [70] with permission of Copyright (2003) from Science.

1.7 Atomic Force Microscopy (AFM)

AFM is a high-resolution scanning probe microscopy technique invented in 1986 by Binnig, Quate and Gerber.⁷¹ This finding was revolutionized by the invention of a scanning tunneling microscopy STM that earned Binnig the Nobel Prize in Physics in 1986.⁷² Unlike the STM that requires a conductive sample, AFM measurements can be taken in an ambient environment without significant sample restriction. This makes it a practical, yet a powerful surface-characterization technique. The working principle of AFM relies upon the interaction between the sharp AFM probe, tip, normally in the order of tens of nm radius of curvature, and the analyzed sample.

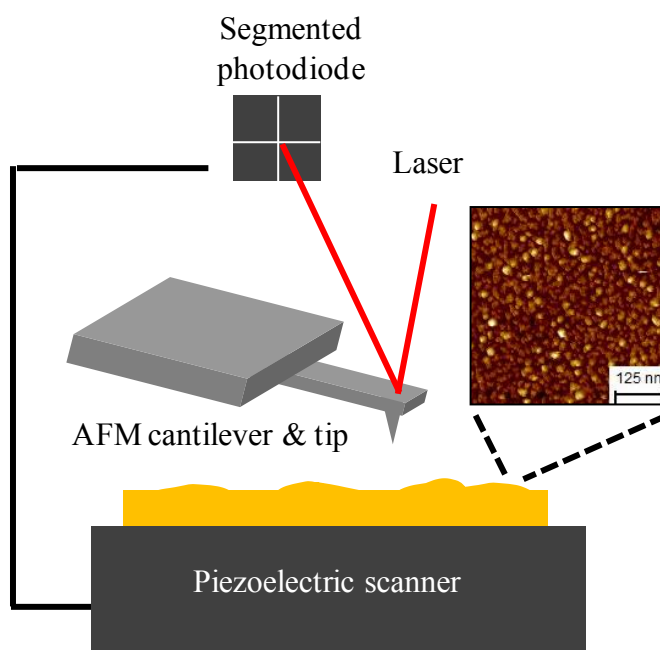


Figure 1. 9 Schematic of an AFM working principle. Inset shows topographical AFM image of a CdSe QDs immobilized on a substrate.

The main components of an AFM as shown in Figure 1.9 consist of an AFM tip as a probe, a laser, piezoelectric scanner, and a segmented photo diode with a feedback loop to control the instrument. The laser is focused on the backside of a cantilever, where the probe is attached. The laser reflection from the cantilever is detected by the segmented photodiode. As the tip approaches the sample, the various interactions between the two that can be originated from van der Waals force, capillary, electrostatic, and/or magnetic forces can bend the cantilever and cause a displacement in the laser deflection on the photodiode. The deflection of the laser is detected by the photodiode, combining with the feedback loop that connects the photodiode and the piezoelectric scanner. This is how the surface topography of the sample material is traced.

The main modes of AFM imaging are contact mode and intermittent or tapping mode. In contact mode AFM, the force used to control the z position of the tip in respect to the sample or set point, is kept constant. Therefore, when the tip is in contact with the sample while scanning, the displacement in the z direction of the tip (as moved by the piezo), represents the surface topography. This z displacement signal is in response to the bending of the cantilever as the tip scans through the sample's surface corrugation, resulting in the shift of the laser position on the top and bottom segments of the photodiode. Aside from surface topography, frictional information of the surface can also be obtained by contact mode AFM imaging. The friction information is gathered from the torsion of the cantilever, which results in a shift of the laser deflection on the left and right segments of the photodiode. In this imaging mode, the tip is always in contact with the surface where the applied force between the sample and the tip depends

on the spring constant of the cantilever. Because the tip is in contact with the surface as it is scanning, the lateral force exerted by the tip to the sample is quite large. One limitation of this method is that it can lead to sample damage, or dragging of weakly bound particles that reduce the scanning quality. For contact mode scanning, the probe used typically has a low spring constant of less than 1 N/m.

The intermittent mode, also known as tapping or AC mode, is one that employs a stiff cantilever that is oscillated at its resonance frequency with a given amplitude, as the probe moves across the sample, intermittently contacting the surface. The amplitude of the AFM cantilever is at its maximum when the tip is freely vibrating away from the sample surface, known as the free amplitude A_0 . As the tip is brought into contact to the sample, the amplitude is damped to A , which depends on the distance to the surface. The ratio:

$$r = \frac{A}{A_0} \quad (3)$$

represents the damping of the amplitude while the tip is in contact with the surface that is proportional to the force. In essence, in this mode, the feedback loop is maintaining a constant force gradient. Surface topography information is gathered by keeping the damping of the amplitude constant. For AC mode imaging, the probe used is stiffer than that used for contact mode imaging. This allows the detachment of the cantilever from the surface with resonance frequency far above the resonance frequency of any other mechanical parts of the instrument (>50 kHz). Since the interaction between the tip and the sample is mostly vertical, this mode is considered to be a less-invasive imaging mode

due to a lower applied lateral force suitable for the imaging of soft samples, films of nanoparticles to avoid particles dragging, and polymers.

Since the first commercialization of AFM in 1989, there have been many developments for the different AFM modes to investigate the different surface properties of a specific substrate. These developments include magnetic force microscopy (MFM),^{73, 74} which is utilized to image sample with magnetic properties in conjunction with a magnetized AFM probe, electrostatic force microscopy (EFM),⁷⁵ and photo-thermal induced resonance AFM.⁷⁶ Aside from imaging, AFM has also been explored as a tool to perform nanoscale surface manipulations. AFM based nanolithography techniques include bias induced⁷⁷, dip-pen⁷⁸, nanografting^{79, 80} and nanoshaving.^{81, 82} At the conclusion of this dissertation, AFM nanoshaving will be demonstrated to manipulate the morphology of a prefabricated Au nanostructure arrays. The versatility of AFM as a nanoscale imaging, characterization and lithography tools makes it desirable and powerful tool for nanomaterials research.

1.8 Confocal Microscopy

Confocal microscopy is an optical imaging technique that employs a spatial pinhole to increase contrast and optical resolution. Confocal microscopy was patented in 1957 by Marvin Minsky. In a conventional wide-field fluorescence microscopy, the entire sample is excited by the light source, and all the signals coming from the sample are detected, including those that originate from the unfocused background. In a

confocal microscope, the spatial pinhole on the laser aperture and the detector aperture allow for sample illumination only at the focal plane and elimination of the out-of-focus signal. This method increases contrast, allowing for high-depth sensitivity and enhancement in lateral resolution as illustrated in Figure 1.10. The image resolution is increased, but only the fluorescence signal that is on the focal plane is detected, so the total signal intensity is decreased. To compensate, a higher integration time, as compared to wide-field microscopes, is needed.

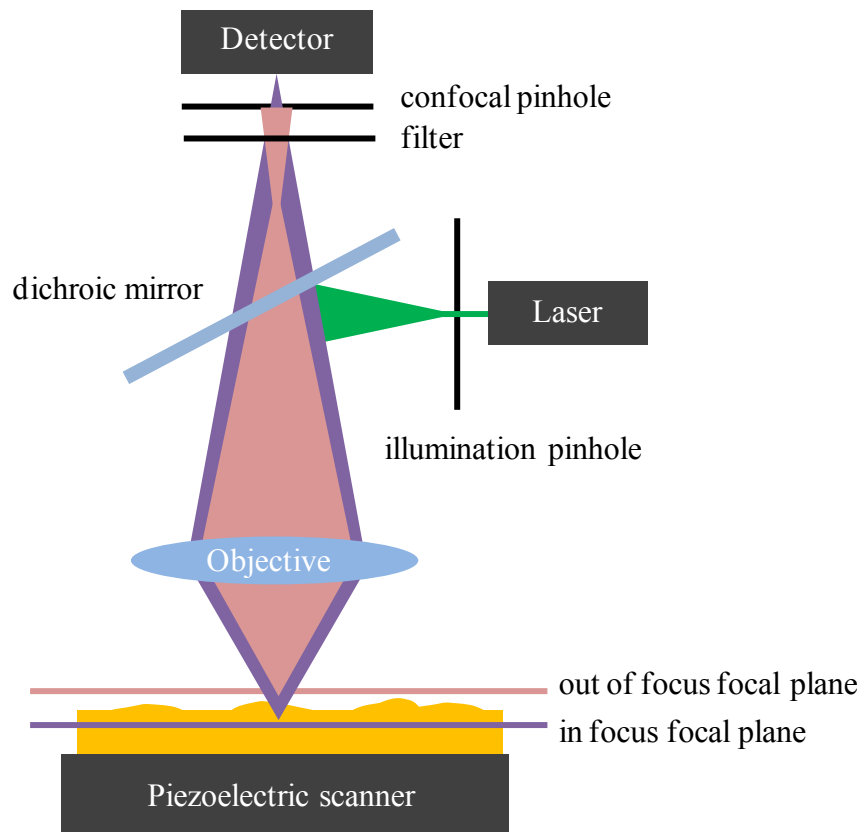


Figure 1. 10 Schematic of confocal fluorescence microscopy comparing the in-focus and out-of-focus signal from the sample.

CHAPTER II

INFLUENCE OF SURFACE LIGANDS AND OXIDATION ON SILVER (I)

CATION EXCHANGE IN CADMIUM SELENIDE QUANTUM DOTS

2.1 Introduction

Quantum dots (QDs) have been explored for a broad range of applications including bio-labeling,^{43, 83, 84} bio-sensing,^{20, 50, 85, 86} optical and electronic devices such as, photo-detectors, light emitting diodes (LED), lasers, and solar cells,^{2, 54, 87-92} because of their exceptional photophysical properties such as their high quantum yield,^{93, 94} narrow luminescence and outstanding stability against photobleaching.^{50, 95} QDs also readily lend themselves for use in chemical sensing, as their interactions with their local environment can result in dramatic changes to their luminescent properties. To tune these interactions, capping agents can be used to alter their solubility in various solvents and to create specific binding sites on the surface. Work from the Weiss group has shown that photochemical processes such as electron and energy transfer reactions can be dramatically impacted by the ligand shell density. They found that the accessibility of acceptor or donor molecules to the surface is impacted by factors such as the extent of ligand shell disorder,⁹⁶ as well as the surface coverage of the capping agents, which can increase the number of surface sites available for the adsorption of other molecules.⁹⁷

Our own studies on the use of CdSe QDs for the chemical sensing of Cu(II) have shown that the photoluminescence response of the CdSe QDs could be dramatically

impacted by the altering of the surface ligand density. This allows a simple chemical platform with high sensitivity and large dynamic range to be developed based on a cation exchange reaction.⁶⁷ Tuning the surface chemistry of QDs presents a facile approach to control many desirable processes. These include the directed doping of QDs with a specific ion to ultimately tune the physical-chemical properties of such nanocrystals.

Cation exchange reactions on CdSe QDs, such as those with Cu(II), present a simple approach for exploring how tuning the surface properties of the QDs influences their interactions with the local environment. While the interactions between the Cu ions and the CdSe QDs have been found to alter only the outermost surface, the cation exchange of Cd-chalcogenide QDs by Ag^+ has been shown to undergo both complete and partial exchange reversibly within the QD lattice.^{88, 98} It has been observed that CdSe QDs react spontaneously with Ag^+ via an ion exchange mechanism that yields Ag_2Se , in a reaction with a thermodynamic driving force of about -1000 kJ/mol in bulk.^{99, 100} This reaction is favored by the large solubility product difference between Ag_2Se ($K_{\text{sp}}: 1 \times 10^{-54}$) and CdSe ($K_{\text{sp}}: 4 \times 10^{-35}$).¹⁰¹⁻¹⁰³

Norris and co-workers recently have succeeded in lightly doping these CdSe QDs with Ag^+ , showing that the ion behaves as an n-type dopant at low doping level and a p-type dopant at high doping level.¹⁰⁴ With the presence of many similar cation exchange reactions involving different QDs such as other Cd-chalcogenides, Zn-chalcogenides and Pb-chalcogenides, and different cations such as Cu^+ , Sb^{3+} in the literature,^{41, 101, 103-105} there has been great interest in exploring the nature of this reaction for a facile synthesis

of Ag-doped chalcogenides, promoting the study of the electronic properties of the incorporation of atomic impurities within the QDs.

We have previously shown that photolithography could be used to spatially tune the surface properties of thin films of CdSe QDs, creating regions of locally photobrightened CdSe QDs. This phenomenon is due to the partial removal of the mercaptocarboxylic acid capping agent, along with regions of locally photodarkened QDs that result from extensive surface oxidation.² In this chapter, photolithography was used to alter the CdSe QDs by creating a locally photobrightened and photodarkened film. The photoluminescence properties of these different areas of QDs were examined as they were exposed to different local environments. In this work, the CdSe QDs were immobilized inside microfluidic channels and used as a platform to perform an *in situ* study of the cation exchange reaction with Ag(I). A patterned array of CdSe QDs on the microfluidic channels created by photolithography was developed to overcome the issue of a mild photobrightening or photodarkening caused by consecutive scanning processes.

The exchange process could be followed by monitoring the steady-state photoluminescence of the CdSe QDs, which is quenched following Ag^+ cation exchange.^{88, 98, 101, 106, 107} Through the use of photopatterned arrays of QDs, generated *in situ* within the microfluidic channels, the associated changes in luminescence as a function of ligand loss and surface oxidation could be readily followed as a function of the concentration of Ag^+ concentration. Those values could then be compared to those of the unmodified CdSe QD background film.

2.2 Experimental Method

2.2.1 Synthesis of CdSe QDs

Trioctylphosphine oxide (TOPO)-passivated CdSe QDs of $3.6 \text{ nm} \pm 0.4 \text{ nm}$ in diameter were synthesized from a well-known solvothermal method.⁶⁰ The QDs were synthesized using CdO as a precursor and were made water soluble via ligand exchange to bind 11-MUA to the surface.

In brief, 250 mg of CdO with 2.85 g hexadecylamine, 1.15 g TOPO and 1.09 g tetradecylphosphonic acid were degassed under reduced pressure at 110 °C for one hour. Then, under nitrogen, the solution was heated to 300 °C until it became optically clear. At that point, 0.5 g tri-n-butylphosphine (TBP) was injected and the temperature was reduced to 260 °C. Then 0.8 g of a 10% by weight Se powder in TBP solution was quickly injected. When the desired size was reached, the flask was cooled down to 60 °C and 10 g of nonanoic acid was added. Methanol was used to clean the solution and the nanocrystals were subsequently resuspended in toluene. Cleaning with methanol was repeated three times.

The exchange of surfactant group from TOPO to a water-soluble group was performed as follows: first 20 mg of 11-Mercaptoundecanoic acid (11-MUA) was dissolved in 15mL of methanol. The pH of the solution was adjusted to 10 - 11 using tetramethylammonium hydroxide. Then 20 mg of CdSe nanocrystals were added to this solution. The mixture was refluxed under nitrogen atmosphere for 6 hours. To clean the nanocrystals, a mixture of ethyl acetate and ether was used to precipitate the particles

which could then be resuspended in methanol. Subsequent cleanings used only ethyl acetate to precipitate the particles. After the final cleaning, the 11-MUA-passivated CdSe were re-suspended in water. Figure 2.1 shows typical TEM images of CdSe QDs as well as the particle size distribution. The TEM images as well as the particle size distribution of the synthesized CdSe QDs.

2.2.2 Substrate Preparation

Two substrates were used for this experiment: glass micro cover glass #2 from VWR (Radnor, PA USA) adhered onto a microfluidic channels device or Si (100). Fabrication of the microfluidic channels is described in the next section. Procedures for the immobilization of the CdSe QDs on oxidized silicon wafers and glass substrates have been described previously in detail¹⁰⁸. Briefly, the Si (100) wafers or glass substrates were cleaned with a base piranha solution ($\text{NH}_4\text{OH}:\text{H}_2\text{O}_2:\text{H}_2\text{O} = 1:1:4$ parts by volume) for 15 min. The substrates were then used for layer-by-layer deposition of polymer poly(diallyldimethylammonium chloride) (PDDA, 20 wt. % in water, MW 100,000-200,000) purchased from Sigma Aldrich and used as-is. Once the substrate was modified with the positively charged PDDA, it was then immersed into a solution of water soluble CdSe QDs capped with the negatively charged 11-mercaptoundecanoic acid (11-MUA). In this system, the QDs are immobilized in the substrate via electrostatic interaction. Figure 2.1 shows the AFM images of the Si (100) substrate before and after CdSe QDs immobilization.

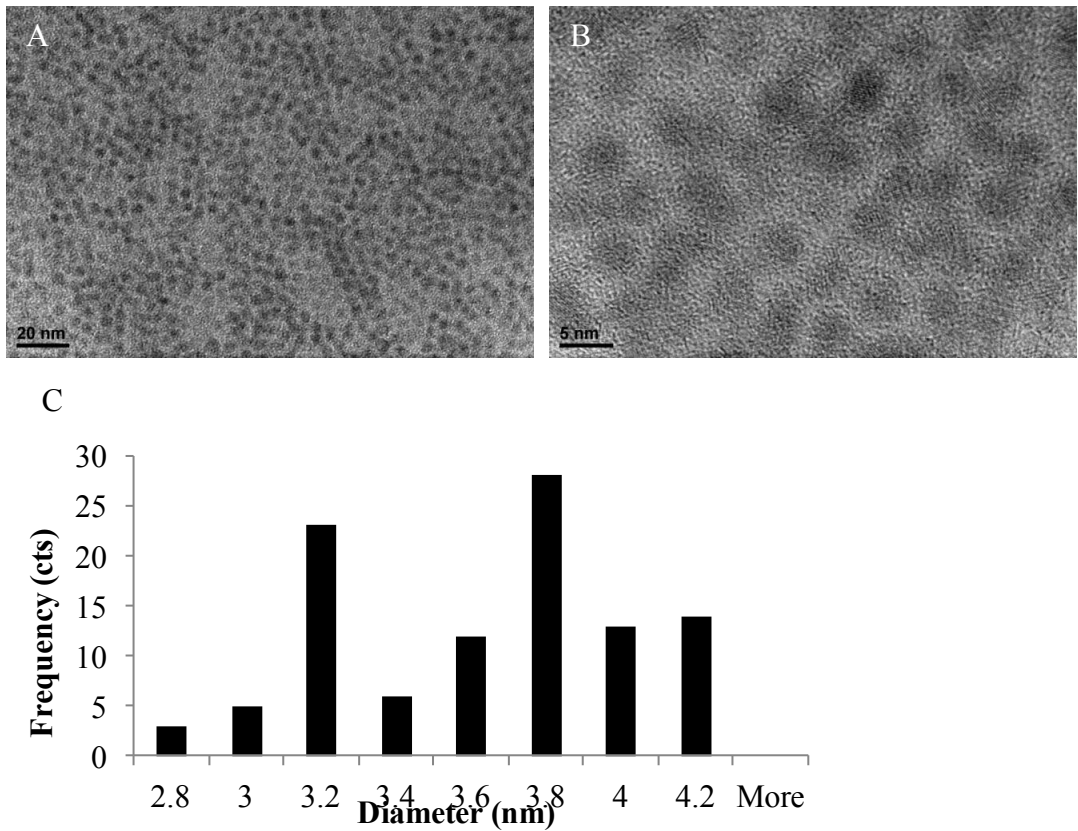


Figure 2. 1 (A) TEM and (B) high resolution (HR-TEM) images of 3.6 nm CdSe QDs and their particle size distribution.

A cleaned and oxidized surfaces of doped Si(100) substrates were used to immobilize the CdSe QDs for the samples used to obtain XPS measurements. The cleaning and immobilization procedures used mimicked those described in the previous section. After the substrate was modified with the polyelectrolyte polymer PDDA, the sample was immersed in a solution of water soluble CdSe QDs for about 8 hours. After CdSe immobilization, the sample was washed with ultrapure water and immersed in a 10

mM 11-MUA/EtOH solution. To mimic the effect of photobrightening and photooxidation, the samples were exposed to UV-ozone for 2 and 7 minutes, respectively, before cation exchange treatments.

2.2.3 Fabrication of Microfluidic Channels and CdSe QDs Immobilization

The fabrication the microfluidic channels is adapted from a previously developed procedure.¹⁰⁹ A glass master was first generated by photolithography using Shipley 1813 photoresist followed by HF etching. *Caution: appropriate protective equipment for HF must be worn, and Ca gluconate gel must be available at all times to treat any burns, followed by immediate medical attention.* PDMS was cured overnight on the mask to form a stamp containing concave grooves. The PDMS stamp was then peeled off of the mask, and holes were drilled for tubing connection with a syringe needle. The stamp was then adhered onto a cleaned cover slip after UV-ozone treatment for 50 minutes using a Novascan PSD-UV Surface Decontamination System ($\lambda_{em} = 185$ and 254 nm). The completed microfluidic structures consisted of 7 channels of 1 to 2.5 cm in length, 30 μm deep and 80 μm wide. Immobilization of the QD films inside the microfluidic channels was carried out by the same processes previously described for making QD films on substrates, except that the solutions were injected into the channels by syringes through 0.018 inch diameter PTFE (Teflon) tubing (Small Parts, Inc.). *Caution: goggles must be worn to protect the eyes especially during the base piranha cleaning steps and HF etching steps above.* Note also that air bubbles in the syringe must be removed prior to injecting the base piranha into the channels to avoid spillage upon syringe retraction.

Whenever needed, the channels were washed with ultrapure water using a total volume of ~1 mL. After the channels were modified with the polymer, a solution of 5×10^{-5} M CdSe QDs was injected through each channel and left overnight with the attached tubes covered with Parafilm. Humidity was maintained at ~45% to ensure good film quality. After immobilization, the channels were washed and injected with 10 mM 11-MUA/EtOH solution for 10 minutes to ensure maximum capping agent coverage on the surface of the CdSe QDs. Uniform CdSe films were obtained inside the channels after washing the channels with ethanol and drying the channels with argon.

2.2.4 Photolithography and Photoluminescence Imaging

A combined confocal fluorescence/atomic force microscopy (AFM) (WITec Alpha300R, Germany) coupled with an argon ion laser (488 nm) and an Andor Peltier cooled (-66°C) CCD detector was used for sample patterning and luminescence measurements. Slightly different experimental set-up will be used throughout this project and will be discussed in detail in the following sections.

Objective lenses of 20, 40 or 100 X, with 0.40, 0.75 and 0.90 N.A. respectively were used to focus the 488 nm Ar ion laser. The objective lenses were used to perform both the laser lithography and imaging processes. The laser power was measured out-of-focus of the objective by a Thorlabs PM100 Optical Power Meter (Thorlabs GmbH, Karlsfeld Germany) equipped with a Thorlabs S130A silicon (power range of 5 nW - 5 mW and wavelength range of 400 nm - 1100 nm). Photolithography was carried out with a laser power of ~120 μ W on the CdSe QDs inside the microfluidic channels that

were filled with ethanol. This was then followed by fluorescence imaging by the same objective with a much lower laser power of $\sim 20 \mu\text{W}$. The laser was reduced to minimize further photochemical changes to the quantum dots during analysis.

2.2.5 X-ray Photo Electron Spectroscopy (XPS) Measurement

XPS data was acquired with a Kratos Axis ULTRA X-ray photoelectron spectrometer equipped with a 165 mm hemispherical electron energy analyzer. The incident radiation was the monochromated Al K α X-ray line (1486.7 eV) with a source power of 120 W (12 kV, 10 mA). The analysis chamber was maintained at a steady base pressure of $\sim 6 \times 10^{-9}$ Torr during sample analysis. Survey scans of up to 1400 eV were carried out at an analyzer pass energy of 160 eV with 1.0 eV steps and a dwell time of 300 ms. Multiplexed high resolution scans of Cd(3d), C(1s), S(2p), Se(3d), and Ag(3d) regions were taken at a pass energy of 40 eV with 0.1 eV steps and a dwell time of 150 ms. The survey and high resolution spectra were obtained with averages of 5 and 20 scans, respectively. The C(1s) peak at 284.8 eV was set as a reference for all XPS peak positions to compensate for any energy shifts due to the spectrometer work function.

2.3 Enhanced CdSe Photoluminescence by Laser Photolithography

It is known that the photoluminescence of 11-MUA capped CdSe QDs can be altered when exposed to laser.² From figure 2.2 we can see that by keeping the laser intensity constant but varying the laser raster speed, the photoluminescence of CdSe

QDs can be altered as a function of laser raster speed. The photoluminescence intensity of the CdSe QDs that are altered by a fast laser raster speed was increased when compared to the background of unmodified CdSe QDs. As the laser raster speed was greatly reduced, the photoluminescence intensity of the locally modified CdSe is lower than the background QDs film. Aside from the changes in their intensity, the photoluminescence maximum peak also shifted the blue lower wavelength emission. This photoluminescence blue shift was more prominent on the CdSe QDs that are altered by a slower laser raster speed.

It is hypothesized that the laser first oxidizes the native 11-MUA capping ligand of the CdSe QDs. It was observed that thiol capping ligand can serve as a hole trap on the nanocrystals surface,⁶⁰ hereby quenching the photoluminescence of the QDs. The oxidation and desorption of these ligands resulted in the increase of the photoluminescence intensity.^{110, 111} This phenomenon supports our experimental data, which demonstrated that the photoluminescence intensity of the CdSe QDs first increases to a maximum value (photobrightening) before it starts to decrease as shown in Figure 2.3 (A). Our previous experiment showed that desorption of the thiol ligands was reversible and can be achieved by exposing the sample to a solution containing free thiol molecules.² Once the capping ligands were oxidized, longer laser exposure began to oxidize the surface of the QDs. This was observed by the decrease of the photoluminescence intensity (photodarkening), and the photoluminescence blue shift, as shown in Figure 2.2 and 2.3. The photoluminescence blue shift can be explained by the

decrease in the effective size of the CdSe QDs, caused by the formation of the oxide layer on the outmost surface.

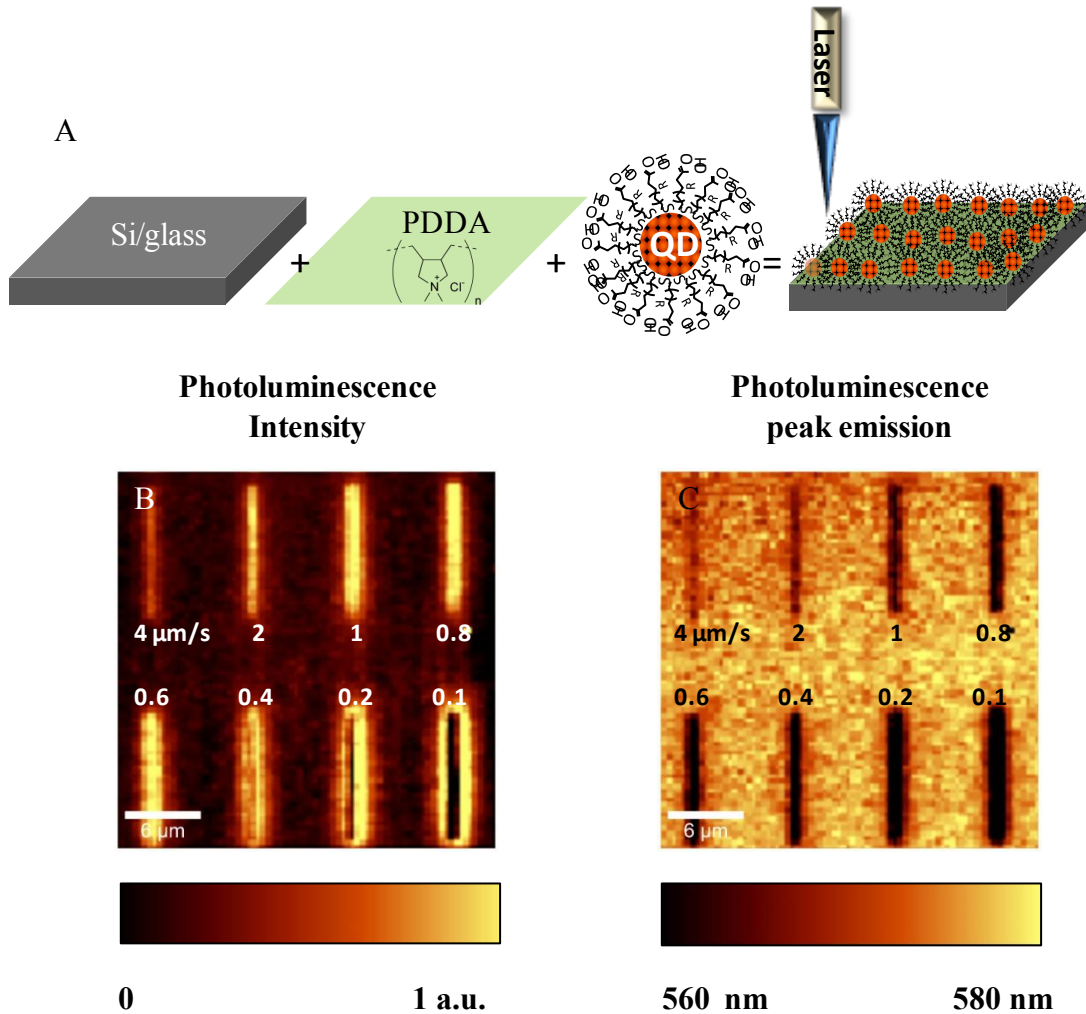


Figure 2. 2 (A) Schematic of laser photolithography on thin film of CdSe QDs immobilized on Si (100). (B) Photoluminescence intensity and (C) photoluminescence peak maxima images of the CdSe QDs after laser photolithography performed with decreasing laser raster speed from 4 to 0.1 $\mu\text{m/s}$.

The effect of the free ligand 11-MUA on the photoluminescence intensity of CdSe QDs is shown on the graph in Figure 2.3. As seen previously from the photolithography experiment conducted in air shown in Figure 2.3, the photoluminescence intensity increased to a maximum intensity before it began to decrease. This can be seen in the graph of Figure 2.4 (A), in which the photoluminescence intensity continued to rise in the first 20 s (photobrightening) before it gradually decreased (photodarkening). This phenomenon was accompanied by a photoluminescence blue shift of about 20 nm.

Using the same laser power to excite the CdSe QDs, when the system was exposed to a solution containing a free 11-MUA capping ligand (B), the increase in the photoluminescence intensity (photobrightening) was also observed, but the photodarkening was not observed within the same collecting time frame. When the measurement was conducted in a 5mM 11-MUA solution, there was an abundant amount of free ligands in the solution that could fill the open vacancy that was created by desorption of the native ligands. Desorption of the oxidized ligands and adsorption of the free ligands prevented further oxidation of the QDs and halted the decrease in the photoluminescence intensity. With this, the photoluminescence intensity of the CdSe QDs was preserved as the photoluminescence peak emission continued to display a blue shift.

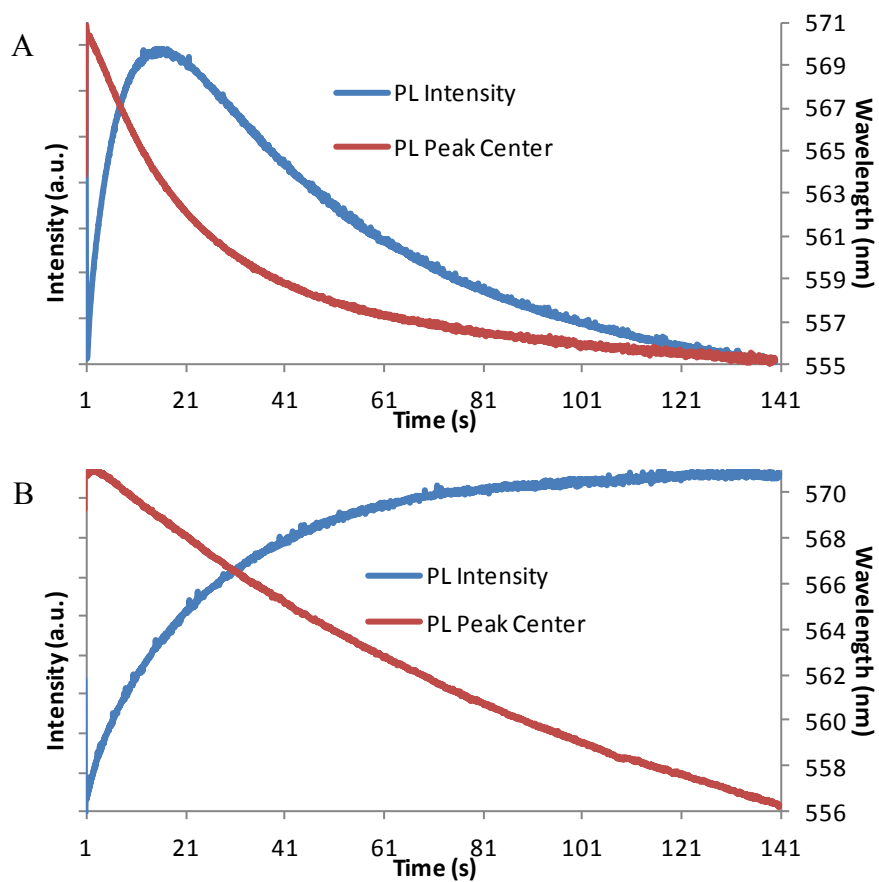


Figure 2. 3 Photoluminescence time series studies of 11-MUA capped CdSe QDs taken (A) in air (B) with free 5 mM 11-MUA dissolved in ethanol performed by the same laser power of $\sim 20 \mu\text{W}$.

2.4 Locally Photobrightened CdSe QDs Sensitivity to Their Local Environment

In the previous chapter, we discussed the fact that the increase in the photoluminescence intensity of the CdSe QDs was due to the partial removal of the oxidized 11-MUA capping agents. Desorption of the capping agents left behind vacant sites on the QDs surface, making it more susceptible as binding sites for other molecules. Our previous study has shown that a thiol tethered porphyrin selectively binds to the locally photobrightened QDs as the emerging of the photoluminescence signal of the porphyrin on the photobrightened CdSe QDs was observed. Also observed was the decrease in the photoluminescence signal of CdSe QDs on the same area due to energy transfer from the CdSe QDs to the porphyrin.²

The removal of the capping agents leaves behind bare, unprotected CdSe QDs surface, thus increasing the QDs' sensitivity to their local environment. Figure 2.5 shows the photoluminescence of locally photobrightened CdSe QDs as they are exposed to different solvents. Figure 2.5 (A) shows the photoluminescence image of the CdSe QDs after the laser photolithography with a power of 120 μW . Note that a rectangular lithography script is used for this experiment instead of the line script. The sample was then further imaged with a much lower laser power of 20 μW . As shown in the previous chapter that discussed line lithography script, the photoluminescence intensity is increased in the area that is altered by laser lithography when compared to the unaltered background CdSe QDs. The photoluminescence intensity spectra of the box area and the background area are plotted on Figure 2.4 (D) and (E) respectively. Figure 2.4 (B) shows the same area as (A) after the sample had been imaged shortly after lithography

and followed by ethanol rinsing. Upon ethanol rinsing, the photoluminescence intensity of the box area was still higher compared to the background area. From the plotted photoluminescence spectra, the intensity of the box area remained unchanged upon ethanol rinsing. The intensity of the background CdSe QDs increases on (B) as compared to (A) as shown on plot (E). This was due to the imaging process required to produce image (A). The imaging process was a mild process of laser photolithography because it was performed with a much lower laser power. Therefore, the photoluminescence intensity of the background CdSe QDs on (B) was a photobrightened version of the same area in (A), which resulted in the increase in the photoluminescence intensity. This also explains the decrease in contrast of the photoluminescence intensity between the box area and the background on (B) as compared to (A). The sample was then rinsed by nanopure water and imaged (C). It was observed that the photoluminescence intensity of the box area appears to be lower when compared to the background; this phenomenon was also observed on the corresponding photoluminescence spectra. From the plot in (D), the photoluminescence intensity of the box area showed a significant decrease as compared to (A) and (B). The photoluminescence intensity of the background CdSe QDs also decreases from that in (B) upon rinsing with water as shown in (E). Note that in this case the background area of CdSe QDs on (C) has undergone a mild laser lithography process caused by imaging, twice. Therefore it was not surprising that the photoluminescence intensity of the background also decreased similarly as the photoluminescence intensity of the box area

decreases. The photoluminescence of the locally altered CdSe QDs via laser photolithography is more sensitive to the exposure of water.

To further prove that the decrease in the photoluminescence intensity was due solely to water exposure and not from oxidation by consecutive scanning processes, a similar experiment was conducted by eliminating the ethanol rinsing process. This was conducted to reduce the effect of mild laser photolithography done by imaging before treatment with water. As shown in Figure 2.5 (A) following photolithography, the photoluminescence intensity of the box area was higher compared to the background as expected. Upon exposure to water the photoluminescence intensity of the box decreased significantly. The photoluminescence of the background slightly decreased in contrast to the data shown previously on 2.4 (B), in which the photoluminescence intensity of the background CdSe increased because of previous scanning process. All of these findings support the idea that the photobrightened CdSe QDs are more sensitive to their environment than the unaltered CdSe QDs.

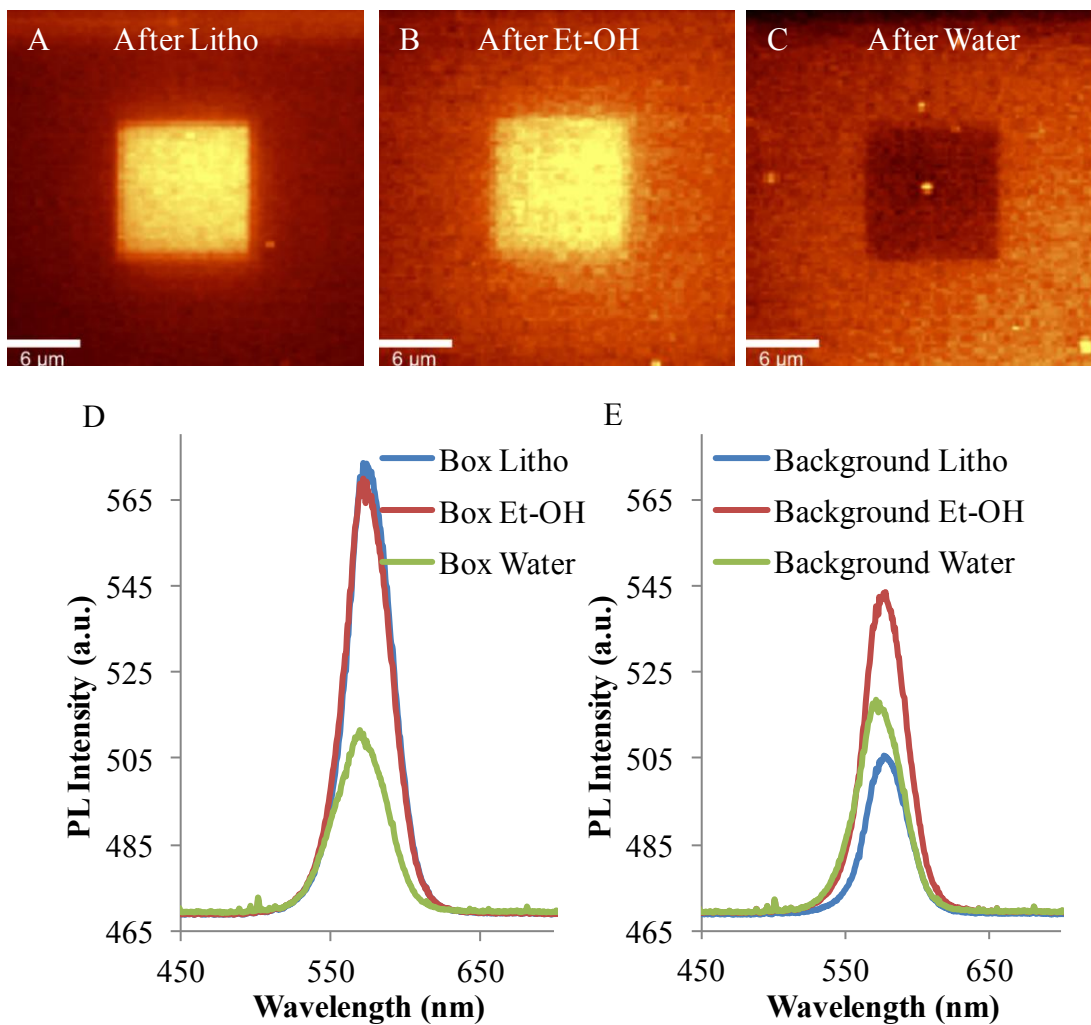


Figure 2. 4 Photoluminescence images of CdSe QDs. (A) Shortly after lithography (B) after ethanol rinsing and (C) after water rinsing of the same area and the corresponding photoluminescence spectra of the (D) photobrightened box area and (E) background.

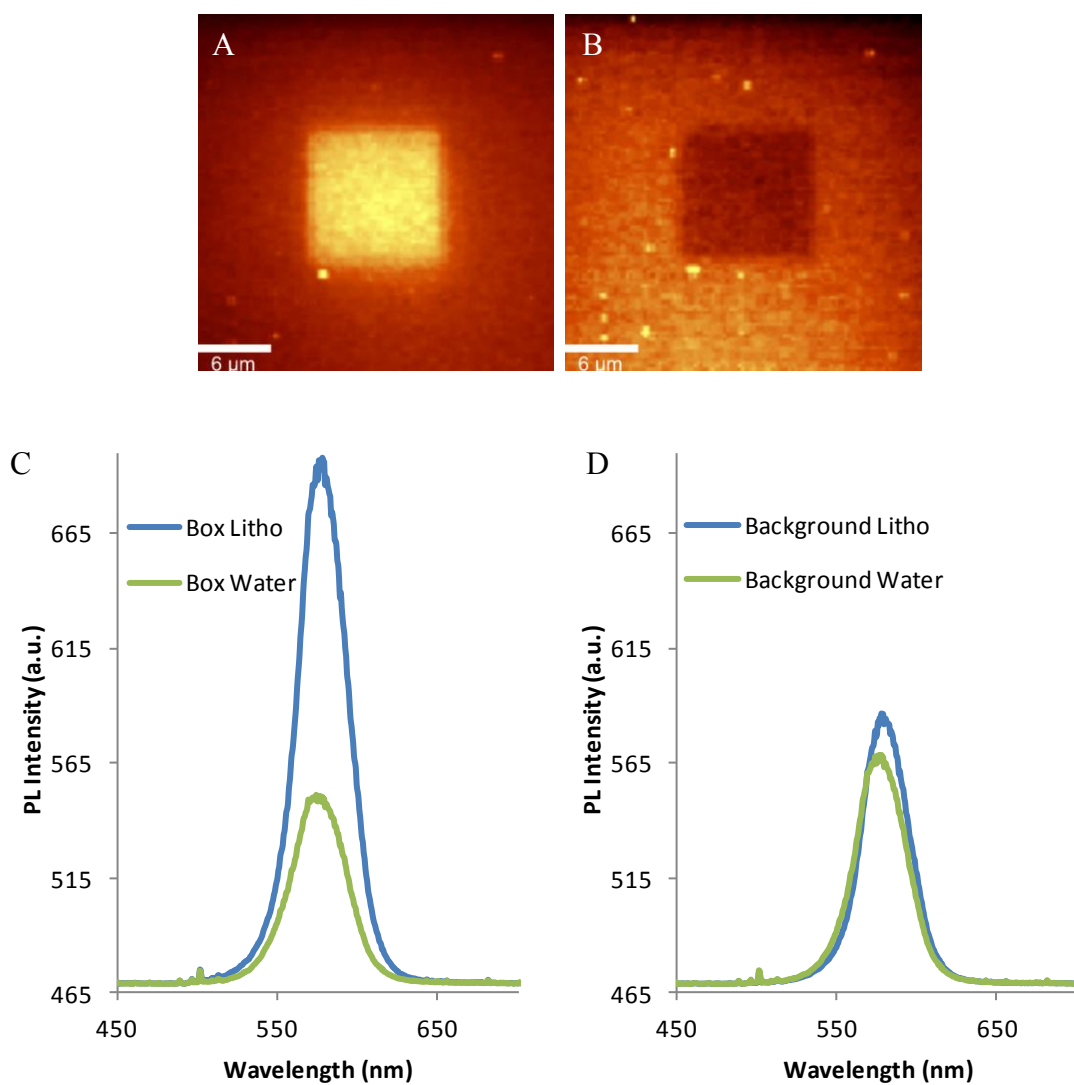


Figure 2. 5 Photoluminescence images of CdSe QDs. (A) Shortly after lithography (B) after water rinsing of the same area and the corresponding photoluminescence spectra of the (C) photobrightened box area and (D) background

To ensure that the decrease in the photoluminescence intensity of the box area was due to water exposure and not due to the oxidation from the consecutive scanning processes, a control experiment was conducted. Similarly, the sample was altered by photolithography. Following ethanol rinsing, the sample was then scanned five times consecutively. As seen in Figure 2.6 (A) the photoluminescence intensity of the box area remained higher as compared to the background after five consecutive scans, although the contrast between the box and the background decreases after scan #2. This was due to the photobrightening of the background caused by previous scan as discussed earlier in this chapter. From plot (B) and (C), the photoluminescence intensity of the box and the background area remained unchanged, aside from the increase after scan #2 on the background area. This data again proves the hypothesis that the scanning process introduced a slight photobrightening effect but did not significantly change the photoluminescence intensity of both the altered and unaltered area. As such, significant photoluminescence intensity decreases were observed due to water exposure and not consecutive scans, as seen in Figures 2.4 and 2.5.

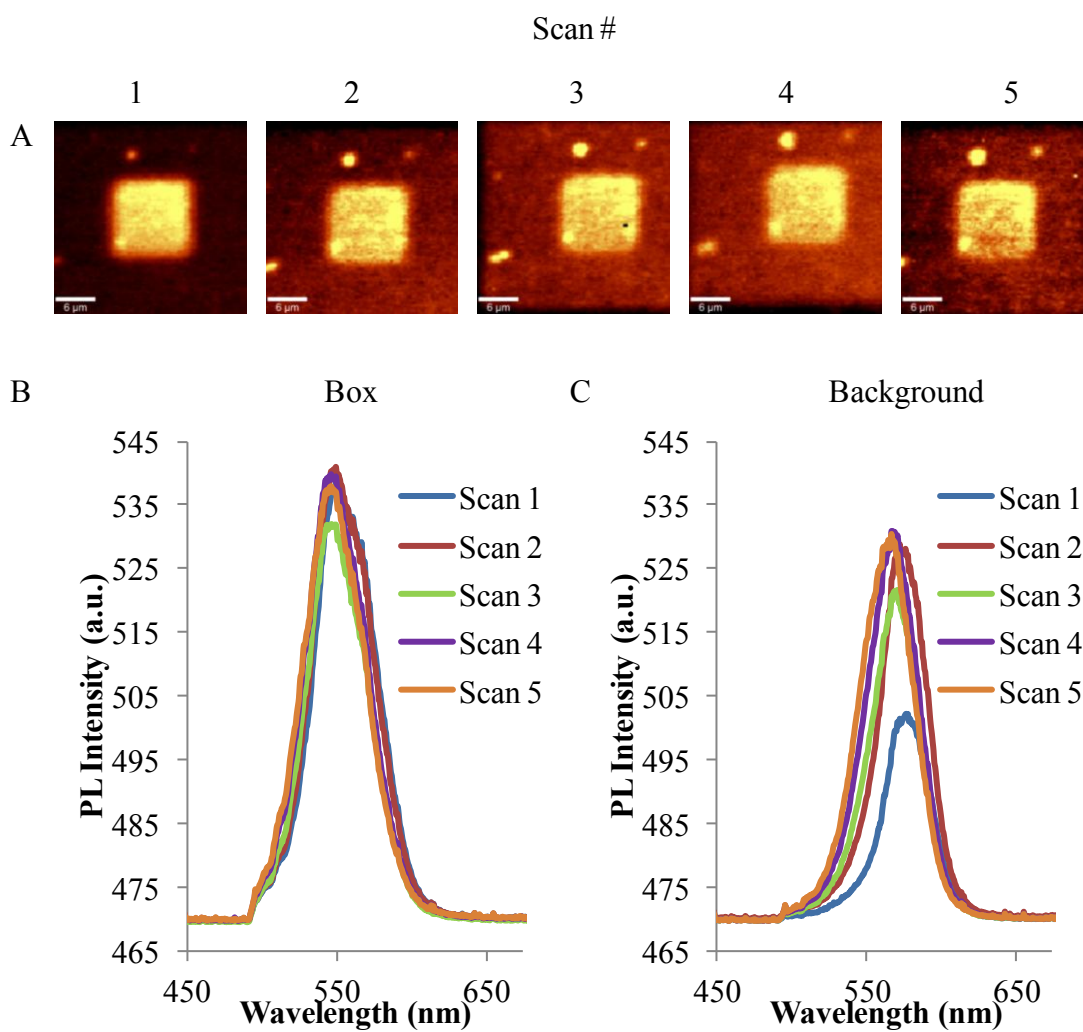


Figure 2. 6 Photoluminescence images of CdSe QDs (A) after ethanol rinsing followed by five consecutive scans and the corresponding photoluminescence spectra (B) of the photobrightened box area and (C) background.

2.5 Photoluminescence Quenching on the Locally Photobrightened CdSe QDs by Ag^+

Previous sections of this dissertation have demonstrated that the locally photobrightened CdSe QDs were more sensitive to their local environment. The exposure of the photobrightened area to water decreased their photoluminescence intensity. Previous work has also shown that the intensity decrease of the locally photobrightened CdSe QDs became more sensitive as they were exposed to Cu^{2+} .⁶⁷ Alivisatos and coworker found that when exposed to a Ag^+ solution, CdSe QDs undergo cation exchange to form Ag_2Se .⁸⁸ This cation exchange process is followed by the decrease of the CdSe QDs photoluminescence signal. In this chapter, the photoluminescence quenching of the CdSe QDs due to Ag^+ on the locally photobrightened CdSe QDs will be discussed.

The experimental set-up for this experiment is slightly different than those described in the previous section. Figure 2.7 shows a schematic of the experimental procedure. A PDMS well was used as a container to hold the solutions containing varying concentrations of AgNO_3 . Laser photolithography was performed on the micro-cover glass containing the QDs facing down as the PDMS well was filled with ethanol. Photoluminescence measurements were conducted with the same manner as previously described, with the PDMS well either filled with ethanol (for control) or AgNO_3 solutions. After each photoluminescence measurement, the well was emptied and rinsed with copious amounts of ethanol as well as the next concentration set of AgNO_3 solution. The #2 micro cover glass containing the CdSe QDs was removed after each

measurement to be rinsed by ethanol and dried by nitrogen gas. The deposition of the CdSe QDs on only one side of the micro cover glass was performed in a similar manner as the photoluminescence measurements. The micro-cover glass slide was adhered to the top of the PDMS well that was filled with the aqueous CdSe QDs solution and allowed to sit overnight. Upon QDs immobilization the micro-cover glass was rinsed with copious amounts of nanopure water and dried with nitrogen.

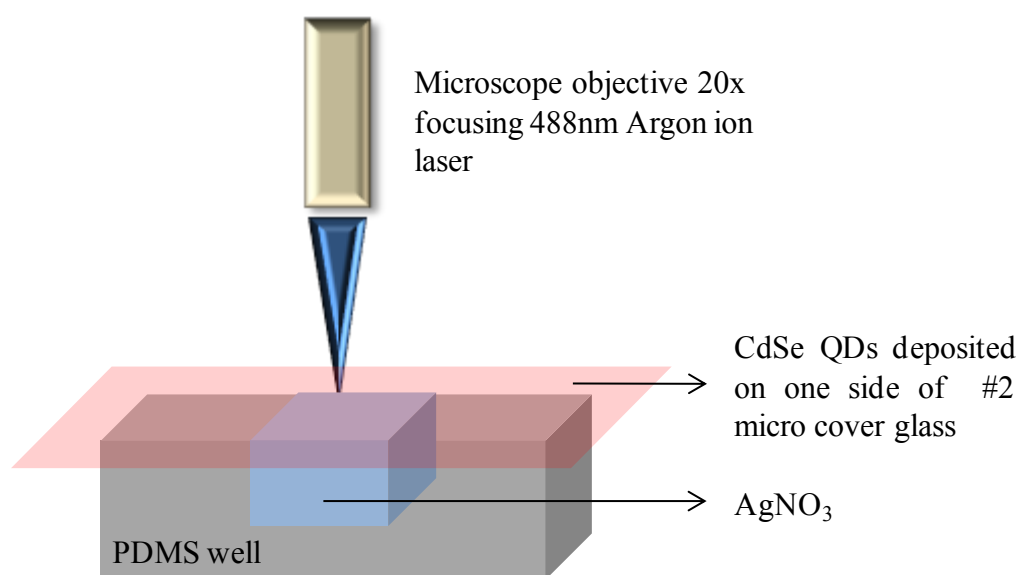


Figure 2. 7 Schematic of the photoluminescence measurement where the micro cover glass containing the CdSe QDs is set facing down on top of a PDMS well containing the different concentrations of AgNO₃.

Figure 2.8 shows the effect of the CdSe QDs photoluminescence when the QDs were reacted with a solution containing Ag^+ . Image 2.9 (A) shows the photoluminescence image taken when the well is filled with ethanol following the photolithography processes. Confirming previous data, the area that was altered with photolithography had an increased photoluminescence intensity when compared to the background. The photoluminescence of the CdSe QDs decreased as the well was filled with increasing concentrations of Ag^+ solutions as shown in (C). This photoluminescence spectrum shows the photoluminescence intensity of the background area as a function of AgNO_3 concentration. Image (B) shows the photoluminescence image of the same area in (A) after exposure to 1 M AgNO_3 . Observations confirmed that the photoluminescence of the box area became lower as compared to the background. These observations lead us to argue that the photoluminescence quenching of the photobrightened box area was greater than that of the background area.

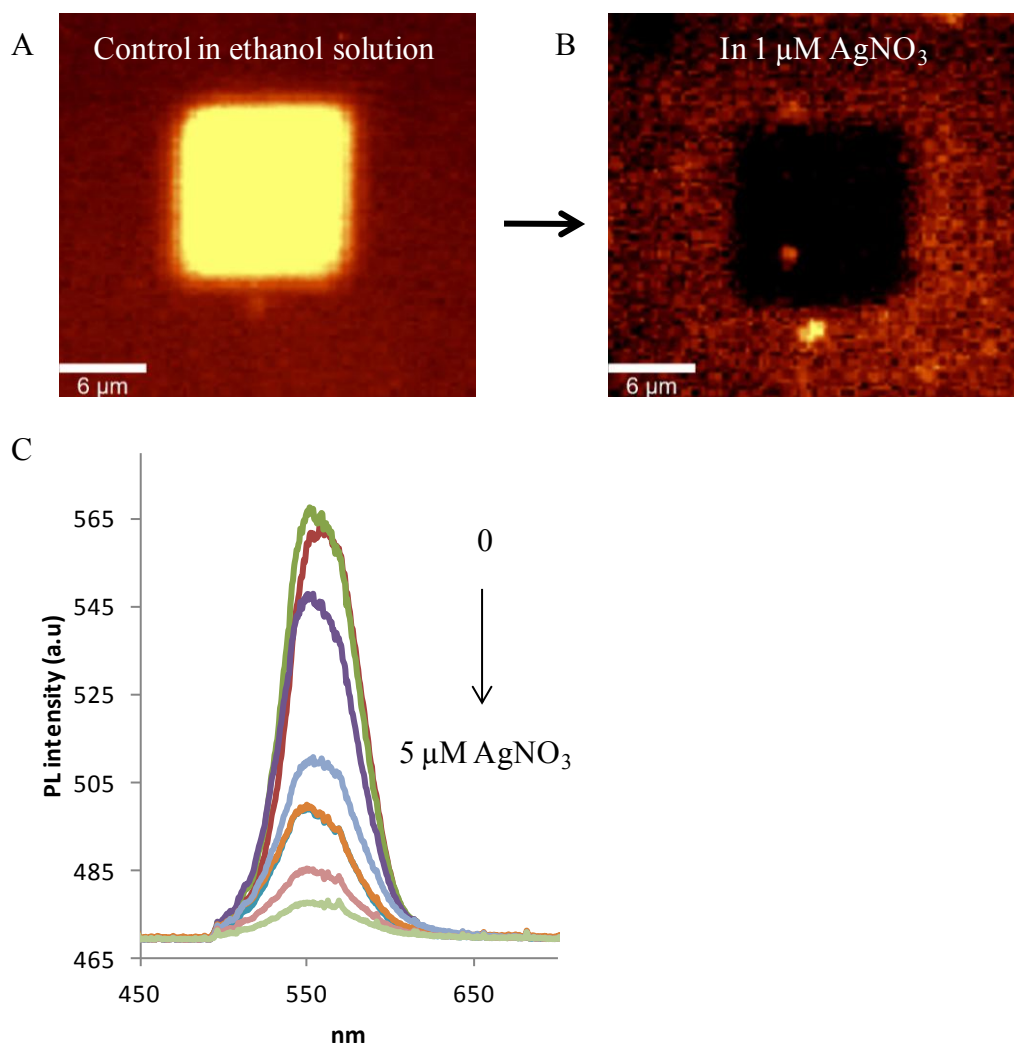


Figure 2. 8 Photoluminescence image of CdSe QDs (A) shortly after photolithography and imaged in ethanol (B) after the exposure of increasing concentrations of AgNO₃ and imaged in 1 μM AgNO₃. (C) Photoluminescence spectra of averaged intensity from the background area as the concentration of Ag⁺ is increased.

The photoluminescence plot I_0/I of both the photobrightened box and the background areas were plotted against the AgNO_3 concentration as shown in Figure 2.9. It was clearly shown that the photobrightened box area was quenched more efficiently when compared to the background area. These sets of data support our previous hypothesis that the locally photobrightened CdSe QDs are more sensitive to their local environment; in this case, we considered the ethanolic solution containing Ag^+ . Still, the experiment contains many complicating parameters that must be considered if we wish to study the effect of photobrightening on this photoluminescence quenching. One of these factors is the photobrightening effect introduced by the imaging process.

Since the area of investigation remained the same, the imaging processes were performed consecutively on the same area, resulting a mild lithography process for each scan. This contributed a limiting factor to the quenching process; depending on the number of consecutive scans, either photobrightening or photodarkening can occur within the CdSe QDs. As seen on the plot in Figure 2.9, the CdSe QDs in the background area experienced photobrightening during the first few scans after the initial control scan, which caused the I_0/I value to be smaller than 1. During the first few scans, the quenching efficiency of Ag^+ was competing with the photobrightening effect from the consecutive scanning process. Since only low concentrations of Ag^+ were introduced at those points, the photobrightening effect was more dominant than the quenching effect, which caused the increase in the photoluminescence intensity. The next section in this chapter will discuss the changes made to optimize the experimental set-up and eliminate the mild photobrightening effect due to consecutive scans.

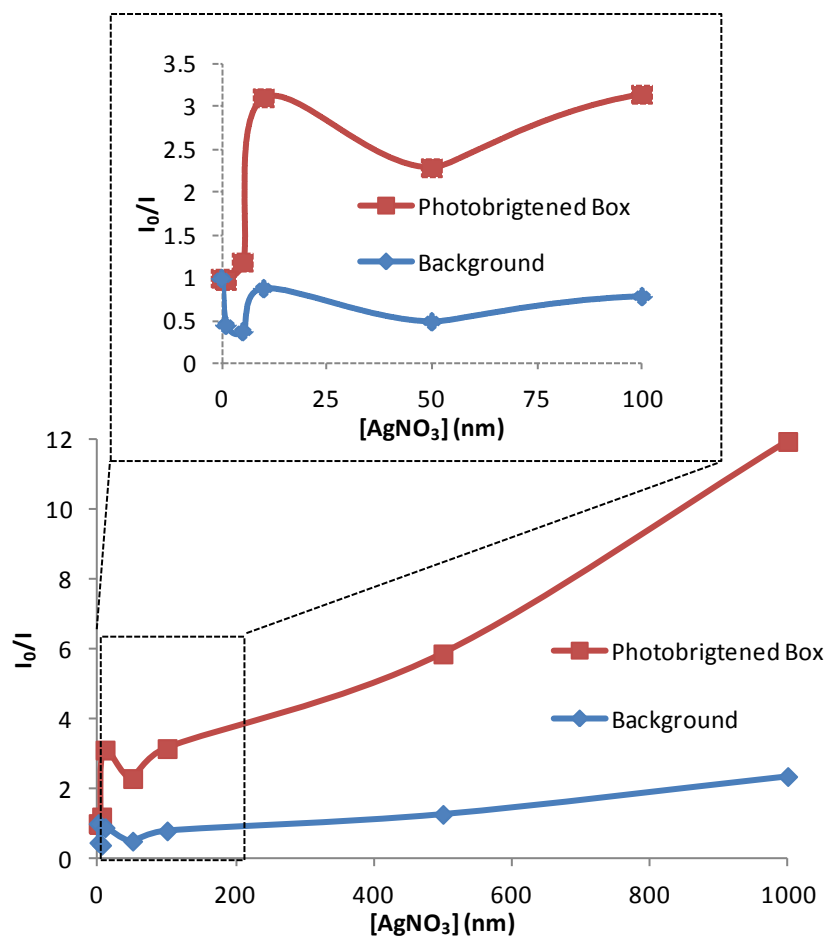


Figure 2. 9 Quenching plot of CdSe QDs as a function of Ag^+ concentrations.

2.6 Following the Photoluminescence Quenching of CdSe QDs by Using Locally Patterned Array in a Microfluidic Channel

Previous sections have shown that laser photolithography can be used to alter the photoluminescence intensity of the CdSe QDs. The resulting altered CdSe QDs can either experience an increase in the photoluminescence intensity (photobrightening), due to the desorption of the oxidized thiol capping agents, or a decrease in the photoluminescence intensity (photodarkening) due to surface oxidation. The CdSe QDs in the locally photobrightened area are shown to be more sensitive to their local environments. It is shown that the QDs in that area are quenched more effectively than the unaltered CdSe QDs in the presence of Ag^+ .

In this section, the effect of photobrightening and photodarkening, which are related to the capping agents (11-MUA) and surface oxidation of the CdSe QDs, will be investigated. To avoid the mild photobrightening effect from consecutive scanning process introduced by the experimental procedure shown in Figure 2.8, a modification to the previous experimental procedure was developed. This method involves the use of microfluidic channels combined with photopatterned array. The schematic of the experiment is shown in Figure 2.10. By employing microfluidic channels, the photoluminescence measurements of CdSe QDs can be performed more efficiently *in-situ*. To monitor the Ag exchange reaction, ethanolic solutions with different concentrations of AgNO_3 were injected into the microfluidic channel and allowed to set for 5 minutes. The channels were then flushed with 1 mL of ethanol. The samples were then imaged. Different concentrations of AgNO_3 can be injected through the channel with

less difficulty compared to the process previously described in Figure 2.8. Using microfluidic channel is advantageous because fewer steps are needed to carry out the experiment. The system's exposure to outside air is also reduced.

Note: not drawn to scale

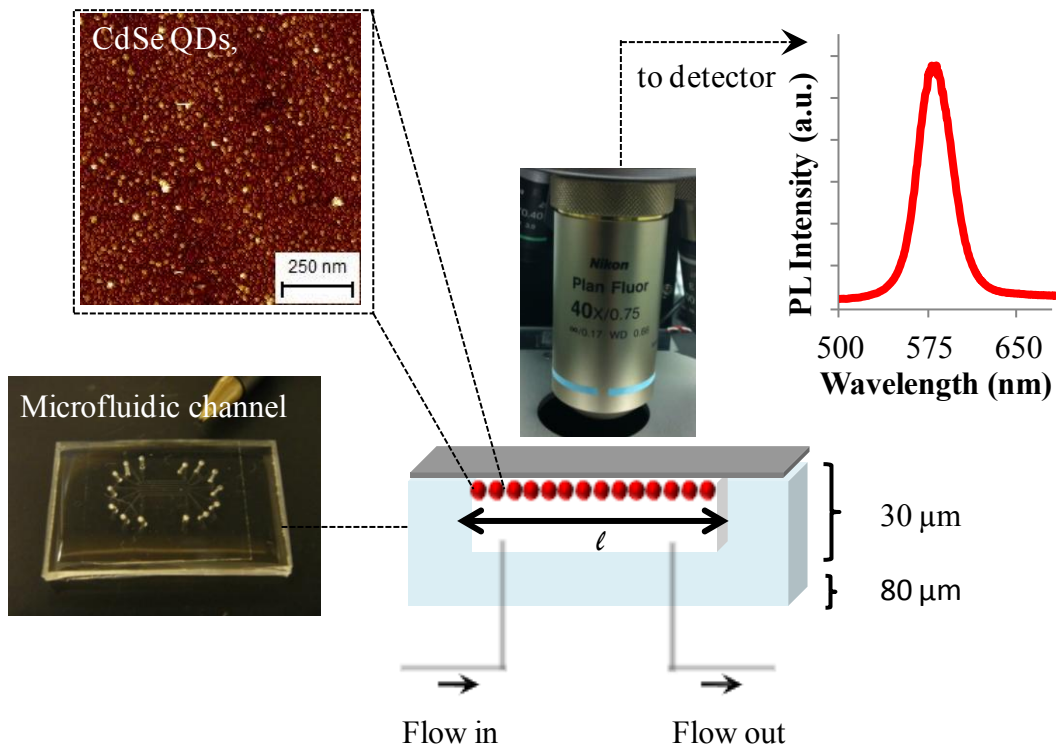


Figure 2. 10 Schematic of the experimental set-up. The CdSe QDs thin film was deposited on a micro cover glass slide inside a microfluidic channel. Photolithography was performed with a 488 nm Argon ion laser with a power of $\sim 115 \mu\text{W}$, while the confocal fluorescence imaging using was performed with a laser power of $\sim 20 \mu\text{W}$.

To systematically follow the impact of surface ligand density and photooxidation on the incorporation of Ag(I) into CdSe via cation exchange, a photopatterned array was used to multiplex the measurements while providing a background reference of unmodified QDs. We have described this overall process in detail elsewhere for spatially tuning QD photoluminescence using lithosynthesis.¹⁰⁸ Here an array was photopatterned with different patterning speeds on the thin film of CdSe QDs inside the microfluidic channels as shown in Figure 2.12 (A). Exposing the QD film to an Ar ion laser in an oxidizing environment (in this case ethanol), lead to the removal of surface bound capping ligands. Longer time exposures, resulted in surface oxidation of the QDs. Varying the patterning speed altered the exposure time of the QDs to the laser and hence the extent of ligand removal and/or surface oxidation.

While a range of patterning speeds were explored, we ultimately limited the experiments to three main ranges to investigate combinations of ligand loss and/or surface oxidation using sample raster speeds of 7 $\mu\text{m/s}$, 1 $\mu\text{m/s}$ and 0.1 $\mu\text{m/s}$, corresponding to lines 1, 2 and 3, respectively in Figure 2.11(A). Consistent with our previous work, and as noted by the spectral changes for the QDs in each line, Figure 2.11(B), the QDs with the shortest exposure were slightly photobrightened and only experienced a small blue shift of ~ 2 nm from their excitonic peak when compared to unexposed QDs in the background. This is indicative of a removal of surface ligands along with a minimal degree of surface oxidation. The QDs in line 2 experienced a larger blue shift of ~ 6 nm and those in line 3 experienced a significant blue shift of ~ 15 nm with significant photodarkening, Figure 2.11 (B) due to increased photooxidation.¹⁰⁸

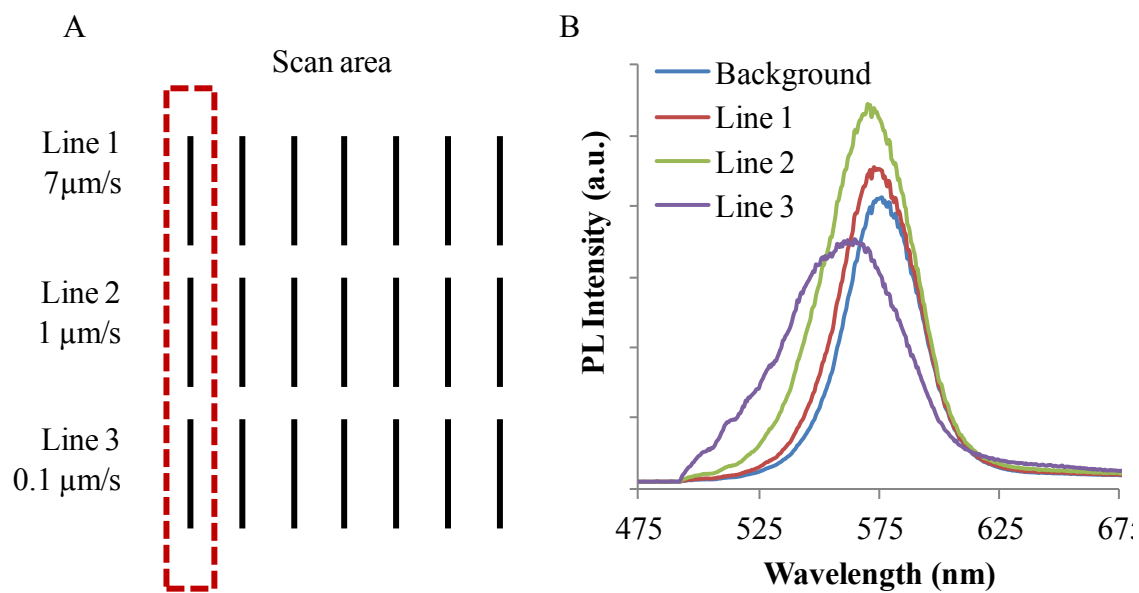


Figure 2. 11 (A) Photopatterned array script with a range of patterning speeds used to create patterns in the CdSe QDs with different surface properties. (B) Photoluminescence spectra of CdSe QDs after patterning. The background is an unpatterned area of the pristine CdSe film, while lines 1, 2, 3 are the areas of CdSe QDs that underwent patterning with different scan rates of 7 $\mu\text{m/s}$, 1 $\mu\text{m/s}$ and 0.1 $\mu\text{m/s}$ respectively.

Beginning with each of these starting conditions, the exchange of Ag(I) was followed by observing the quenching of the photoluminescence intensity of the CdSe QDs through the addition of AgNO₃ at different concentrations in ethanol. The series of images shown in Figure 2.12 (A) show that the ratio of the photoluminescence intensity between the different lines and the background changes as the concentration of Ag⁺ increased. This phenomenon was more prominent in the photoluminescence images of the QDs in line 3. In the case where no Ag⁺ is present, the photoluminescence intensity of line 3 was lower than the the background. But at larger concentrations of Ag⁺, the photoluminescence intensity of the oxidized CdSe QDs appeared brighter than the unmodified CdSe background. This observation suggests that the Ag⁺ cation exchange efficiency of the photoaltered CdSe differs from that of the unmodified CdSe film. To ensure that the variance of photoluminescence intensity is due to the difference in cation exchange efficiency and not internal measurements variations, control experiments were conducted. The same photopatterned array and patterning speeds were used, with photoluminescence imaging of each array carried out under ethanol. Data on the control experiments are shown in Figure 2.13, where the photoluminescence intensity of each array is comparable within the 7 different scan areas.

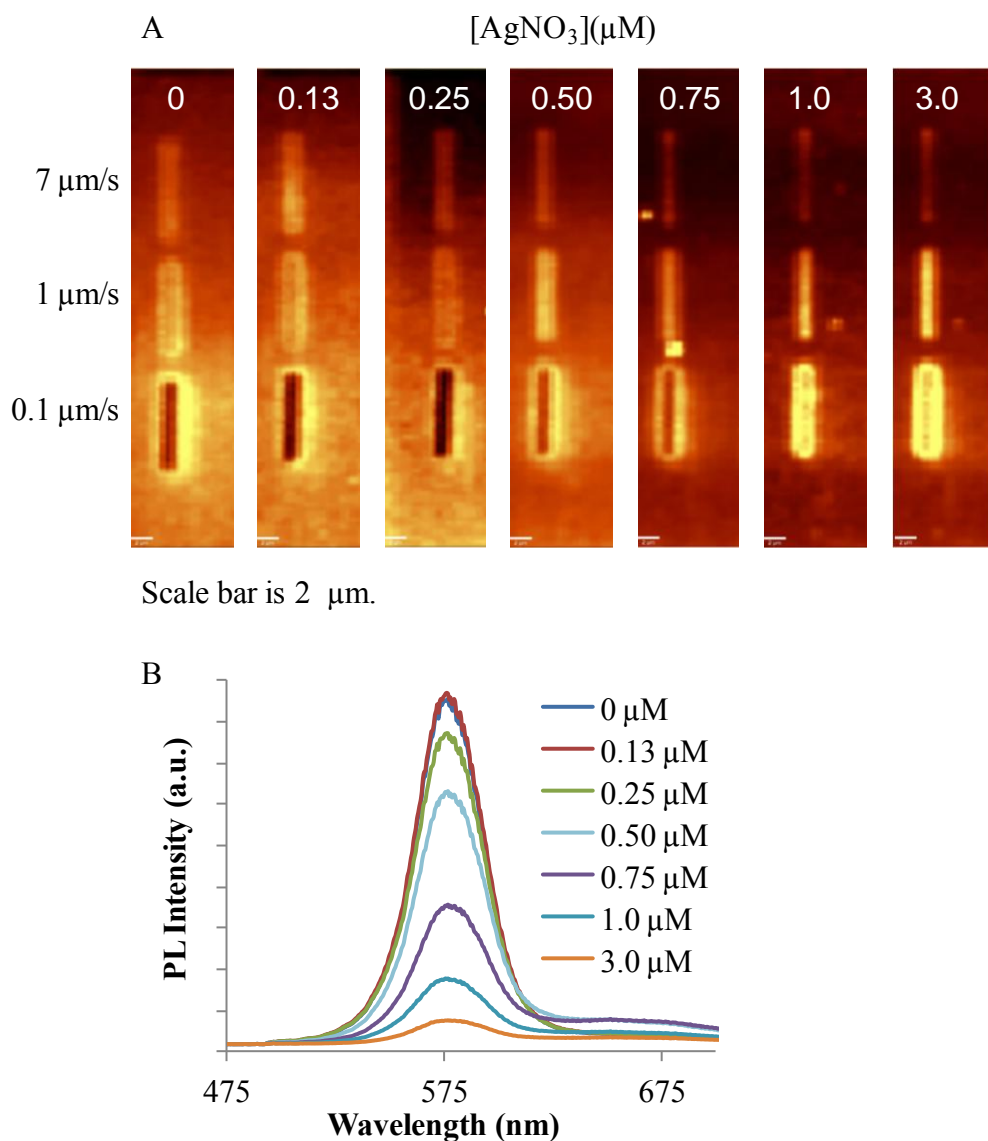


Figure 2. 12 (A) Photoluminescence images of thin film CdSe QDs immobilized inside a microfluidic channel after patterning at different rates with increasing AgNO₃ concentrations, PL intensity images on the different Ag⁺ concentrations are scaled individually for a better image contrast. (B) The photoluminescence spectra of the background with the different AgNO₃ concentration.

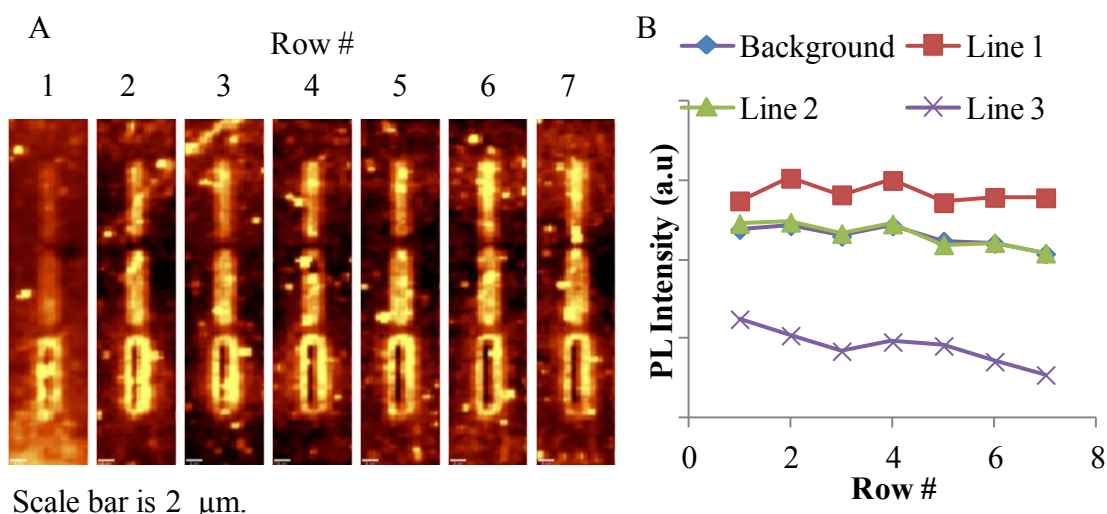


Figure 2. 13 Control experiment showing (A) fluorescence images of CdSe QDs inside a microfluidic channel on 7 different regions of lithography imaged under ethanol with $\sim 20 \mu\text{W}$ 488 nm Ar ion laser, (B) average fluorescence intensity spectra of the images in (A).

This cation exchange reaction is known to be thermodynamically favorable.^{88, 98} As shown in the spectral data in Figure 2. 12 (B), the photoluminescence intensity decreased after the addition of only 250 nM of AgNO_3 , and after the exposure to only 3 μM solutions of Ag^+ the photoluminescence intensity of the CdSe QDs was reduced to almost zero. This suggests that most of the Cd^{2+} were exchanged with the Ag^+ . Hence, the photoluminescence is no longer detected by our spectrometer. Based on these results, luminescence studies above 3 μM Ag^+ were not carried out.

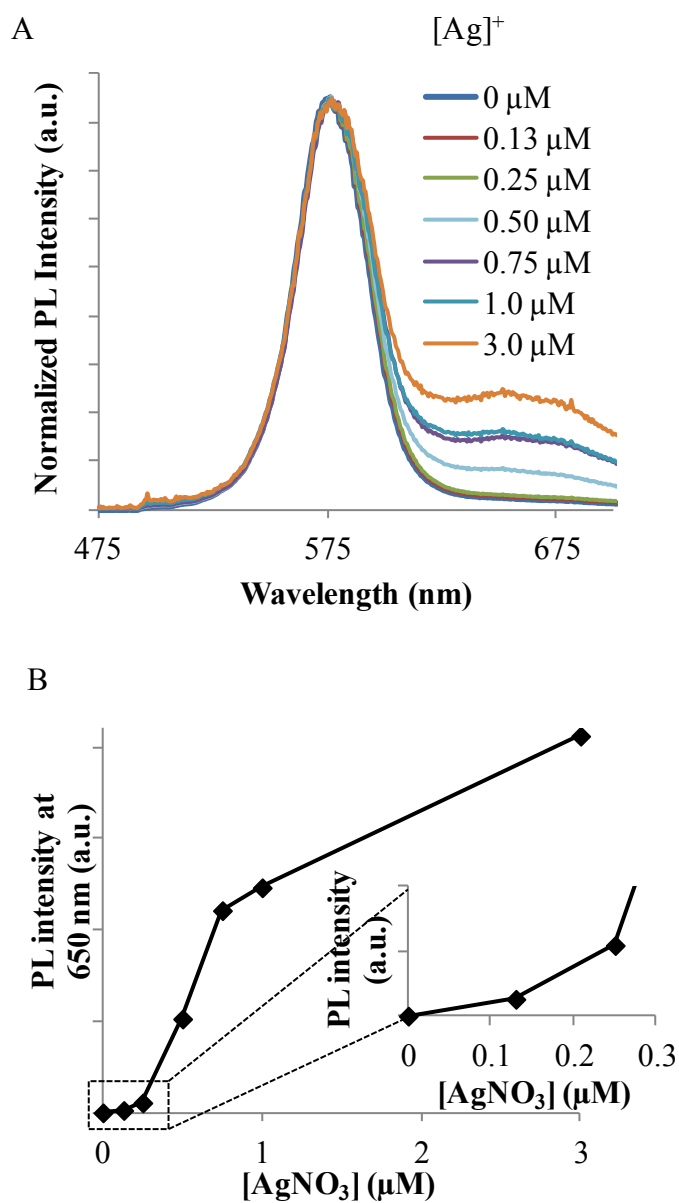


Figure 2. 14 (A) Normalized photoluminescence spectra of CdSe QDs with the presence of $AgNO_3$ normalized at the CdSe excitonic peak. (B) Plot of the normalized photoluminescence intensity of the small shoulder at 650 nm with increasing concentration of $AgNO_3$.

As the concentration of Ag^+ increases, the photoluminescence spectra showed a broad emission shoulder at 650 nm aside from the main band edge emission peak (Figure 2.14 (A)). This small shoulder started to become apparent beginning at a Ag^+ concentration of 500 nM. The intensity of this shoulder increased as the concentration of Ag^+ increases, and could be attributed to a defect peak that corresponds to the recombination of photoexcited electrons with Ag-bound holes, *i.e.* the binding of the photoexcited electrons to Ag^+ .¹⁰⁴ As shown in Figure 2.14 (B), the peak intensity of the photoluminescence shoulder at 650 nm increased only slightly until the Ag^+ concentration reached 500 nM, after which it more dramatically increased till ~ 1 μM , and then proceeded at a slower rate. Measurements were not conducted beyond Ag^+ concentration of 3 μM because the photoluminescence signal of CdSe was hardly detectable at this point.

2.7 Cation Exchange in CdSe QDs by Ag^+

Based on AFM tapping mode topography images, as shown in Figure 2.15, there is no observable change on the CdSe QD film before and after treatment with an excess of AgNO_3 (100 μM). This supports the claim that the reduction in the fluorescence intensity is not caused by the physical removal of CdSe QDs from the surface.

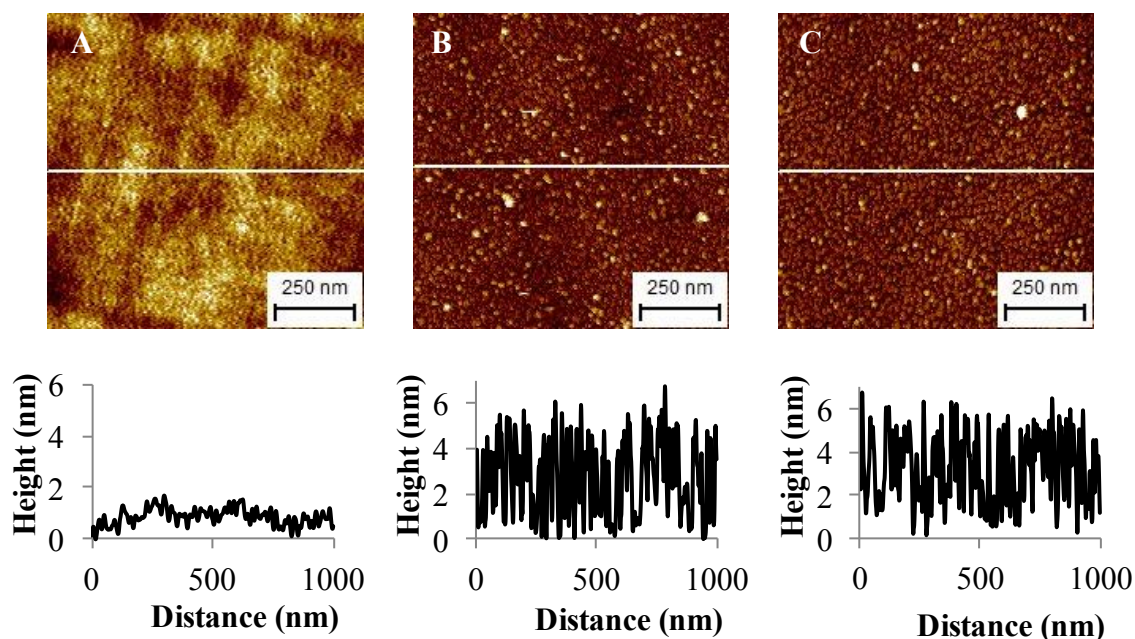


Figure 2. 15 AFM AC mode topography images and cross section profiles of (A). Si-PDADMAC. (B) Si-PDADMAC-CdSe 11-MUA capped. (C) Si-PDADMAC-CdSe 11-MUA capped after 100 μM AgNO_3 .

The XPS spectra of the before and after reacted CdSe QDs (Figure 2.16) further confirms the cation exchange reaction:



These results are in complete agreement with photoluminescence quenching of the CdSe QDs due to the cation exchange reaction. Figure 2.17 shows the high-resolution XPS spectrum of Cd(3d), Ag (3d), Se(3d), and S(2p) after exposing the enhanced CdSe films with ion-free pure water (upper row) and an excess of Ag^+ ion solution (100 μM) to allow complete exchange (bottom row). Before the treatment with Ag^+ ions, the typical doublet of the Cd(3d) from the CdSe QDs can be observed at 404.9 ± 0.1 eV and

411.6±0.1 eV corresponding to the Cd(d_{5/2}) and Cd(d_{3/2}) transitions, respectively. These peaks disappeared upon the addition of 100 μM Ag⁺, while the typical Ag(3d) doublet peaks appear at 368.0±0.1 eV and 374.0±0.1 eV. In addition, upon the complete exchange of Cd²⁺ to Ag⁺, a small shoulder located at 59.2±0.1 eV on the Se(3d) spectrum is observed and which can be attributed to SeO₂, as previously reported for oxidized CdSe QDs.¹¹²

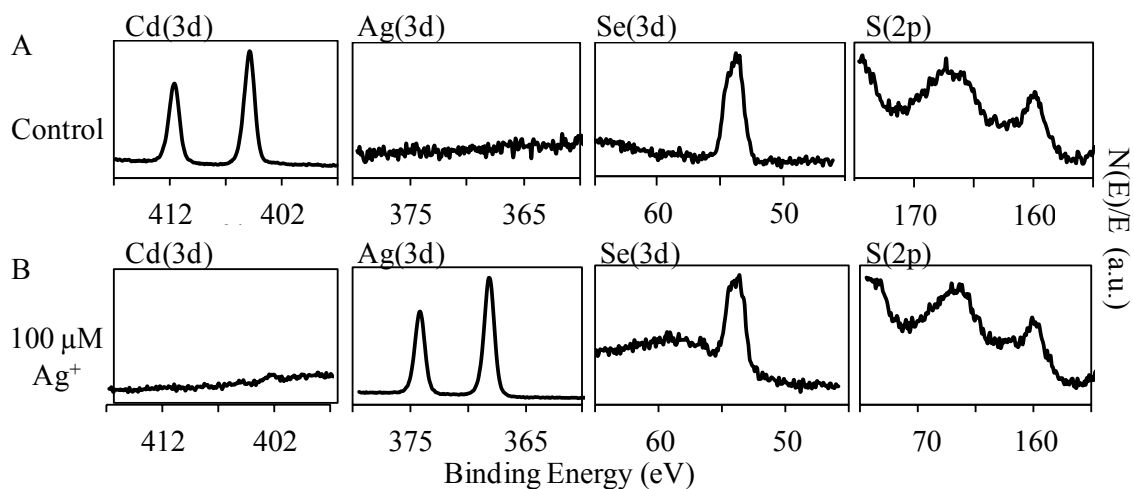


Figure 2. 16 XPS spectra of CdSe QDs film in the Cd(3d), Ag (3d), Se(3d), S(2p) regions of CdSe QDs A) After exposure to pure water (upper row) and B) 100 μM Ag⁺.

2.8 Locally Photobrightened CdSe QDs on the Cation Exchange with Ag⁺

As shown in Figure 2.17, the quenching plot of the CdSe QD photoluminescence, the cation exchange between the background area and the pristine CdSe film were different from the area that has been photobrightened with a minimal degree of oxidation

(line 1), and to the area with a more extensive degree of surface oxidation (line 3). The CdSe QDs that are in line 1 exhibited more efficient quenching compared to the background. As reported in our previous work, the photobrightening induced by the lithography process was due to the partial removal of thiolate surface ligands.² The partial ligand removal of the 11-MUA reduces the ligand packing density and we propose that the observed increase in cation exchange for the photobrightened area of the QDs in line 1 resulted from the increased accessibility of the surface to Ag ions due to the reduced ligand surface coverage.

Recent work by Norris and co-workers employs the addition of trioctylphosphine (TOP), a common capping agent used for non-water soluble CdSe QDs, to slow down the efficiency of the cation exchange reaction.¹⁰⁴ A previous work by Allvisatos and co-worker on the milliseconds kinetic study of the stated CdSe cation exchange, revealed that the reaction proceeded at a slower rate when a high dodecylamine was used. The dodecylamine slowed the reaction kinetics by reducing the availability of free Ag⁺ ions and the accessibility of nanocrystal surfaces.¹¹³ These studies support our argument that the efficiency of the cation exchange reaction is sensitive to the density of the capping agent on the surface of the QDs. The CdSe QDs on line 2 and 3 exhibited a lower cation exchange rate compared to the pristine background CdSe. It is known that the oxidation of CdSe QDs can lead to the formation of SeO₂¹¹² as also seen in our oxidized CdSe QDs samples, shown in Figure 2.18. The formation of the SeO₂ shell on the CdSe surface decreased the accessibility of the Cd²⁺ ion from the Ag⁺. Also note that the shape of the quenching plot in Figure 2.17 resembles the plot shown in Figure 2.12 (B), with

the rise of the photoluminescence shoulder at 650 nm. This indicates that the observed photoluminescence quenching and the incorporation of the Ag(I) in the CdSe QD lattice are related.

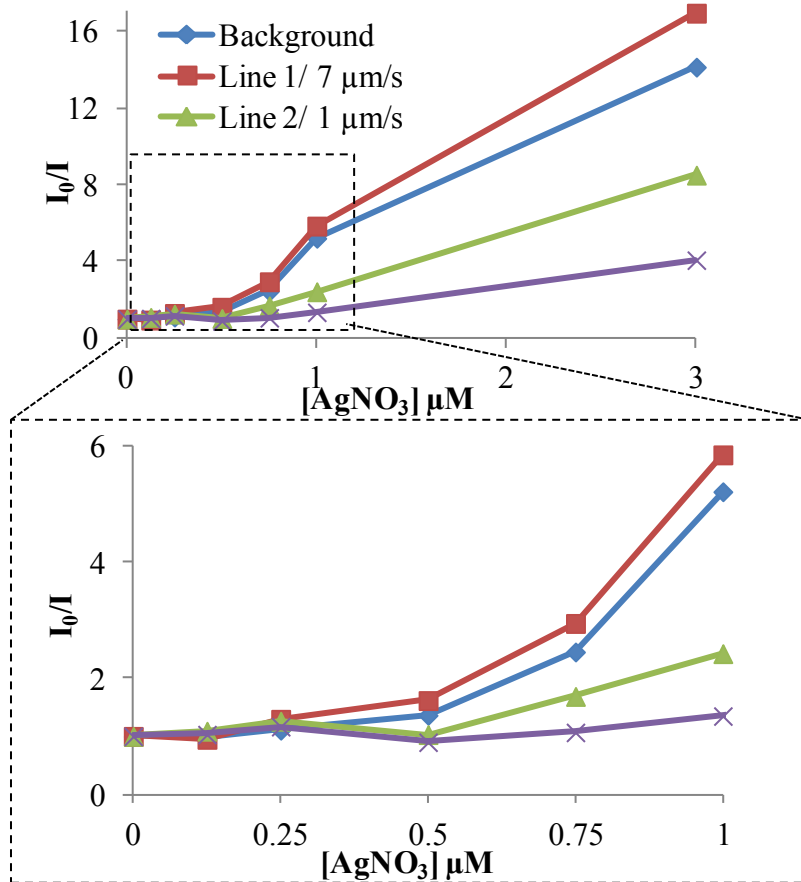


Figure 2. 17 Quenching plots of the CdSe QDs photoluminescence by AgNO₃. The background is given by the unmodified CdSe film, while lines 1 through 3 are CdSe QDs that have been photo-oxidized with a laser power of ~115 μW at speeds of 7, 1, and 0.1 μm/s.

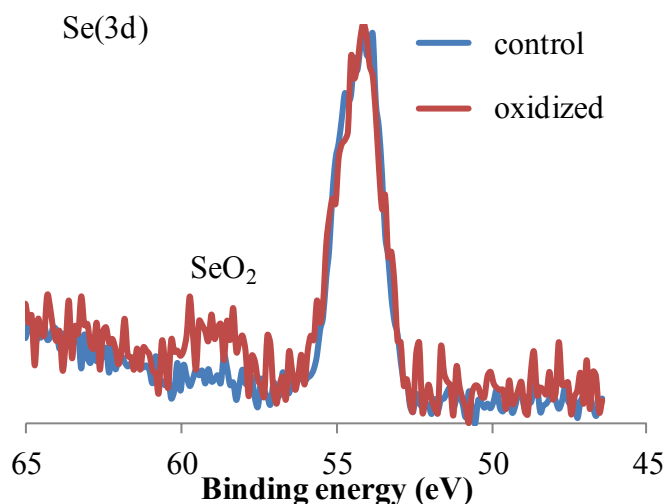


Figure 2. 18 XPS spectra of Se(3d) before and after UV-ozone treatment. The shoulder signal centered at 58 eV is corresponding to the formation of SeO₂.

This was further confirmed by the elemental analysis from XPS measurements reported in Table 2.1. Three different samples of CdSe QDs supported on Si(100) surface were treated with 10 μM AgNO₃ to undergo partial cation exchange. A slightly higher concentration of Ag⁺ was used for XPS measurements, compared to the photoluminescence quenching measurements due to the low intensity of the Ag(3d) peak when samples were treated with 5 μM AgNO₃. To mimic the effect of photobrightening and photooxidation, the samples were exposed with UV-ozone for 2 and 7 minutes respectively. When exposing the surface to UV-ozone, the photoluminescence of the CdSe increased and then decreased in the same fashion as when under laser illumination. This change, however, occurred at a much slower rate than when using the more intense 488 nm Ar ion laser. As such, the same photochemical processes are assumed to be

occurring as under laser illumination as shown in Figure 2.19. The ratio of Ag/Se increased and the ratio of Cd/Ag decreased for the sample that was photobrightened. The opposite was true for the oxidized sample.

Table 2. 1 XPS table of the ratio of elemental analysis of pristine CdSe QDs film, CdSe QDs after partial cation exchange with 10 μM AgNO_3 with varying UV ozone exposure time, and CdSe QDs after complete exchange with 100 μM AgNO_3 .

	Cd/Se	Cd/Ag	Ag/Se	$(\text{Cd}+1/2*\text{Ag})/\text{Se}$	$\text{S}/(\text{Cd}+1/2*\text{Ag})$
CdSe no UV ozone	3.45	N/A	N/A	3.45	2.16
Ag_2Se no UV ozone	1.73	1.73	1.00	2.23	1.74
CdSe 2 min UV ozone	3.97	N/A	N/A	3.97	2.05
Ag_2Se 2 min UV ozone	1.44	0.94	1.54	2.21	2.12
CdSe 7 min UV ozone	1.98	N/A	N/A	1.98	3.37
Ag_2Se 7 min UV ozone	1.79	1.47	1.22	2.40	3.05
Ag_2Se complete exchange	N/A	0.00	2.42	1.21	2.01

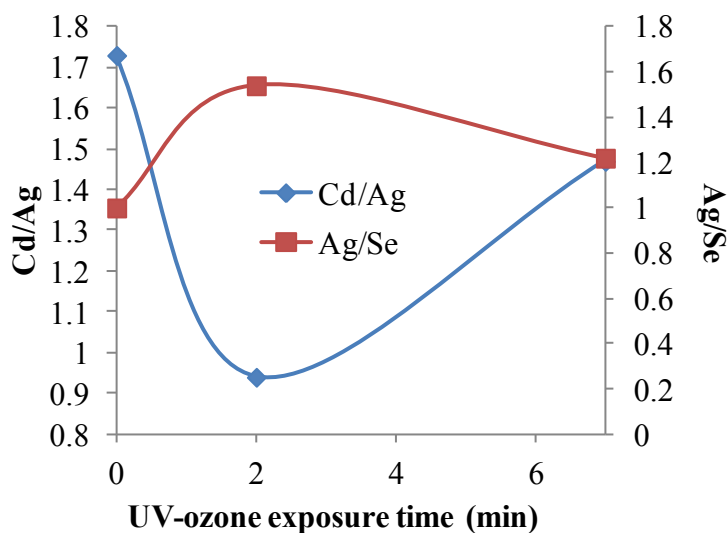


Figure 2. 19 Ratio of Cd/Ag and Ag/Se calculated from the XPS data of CdSe QDs after partial cation exchange with 10 μM AgNO_3 for samples without UV-ozone oxidation, with 2 minutes of UV-ozone oxidation (photobrightened), and with 7 minutes of UV-ozone oxidation (oxidized).

As shown in Figure 2.20 the fluorescence intensity of CdSe QDs that are in lines 2 and 3 increase after the addition of 500 nM of AgNO_3 . This response is unlike the fluorescence intensity of the CdSe QDs that are in the background and line 1; the intensity gradually decreased with the addition of Ag. The addition of only a few Ag^+ ions per nanocrystal can increase the fluorescence intensity of CdSe QDs. This small amount of Ag acts as an electronic dopant with n-type donor behaviour, where the donor electrons are trapped outside the CdSe QDs surface, inducing a positively charged impurity center.¹¹⁴ These positively charged CdSe QDs have been found to exhibit an

unusual brightness as well as a reduced blinking activity.^{115, 116} As we concluded earlier in this paper, the cation exchange was reduced for those CdSe QDs that are in line 2 and 3. It is possible that only a few Ag^+ were able to be exchanged on the oxidized CdSe QDs, and were thus acting as an n-type donor, which accounts for the increase in the fluorescence intensity. This doping behaviour was not observed on either the pristine CdSe QDs nor on the photobrightened CdSe QDs because of the very effective nature of the cation exchange reaction between Cd^{2+} and Ag^+ .

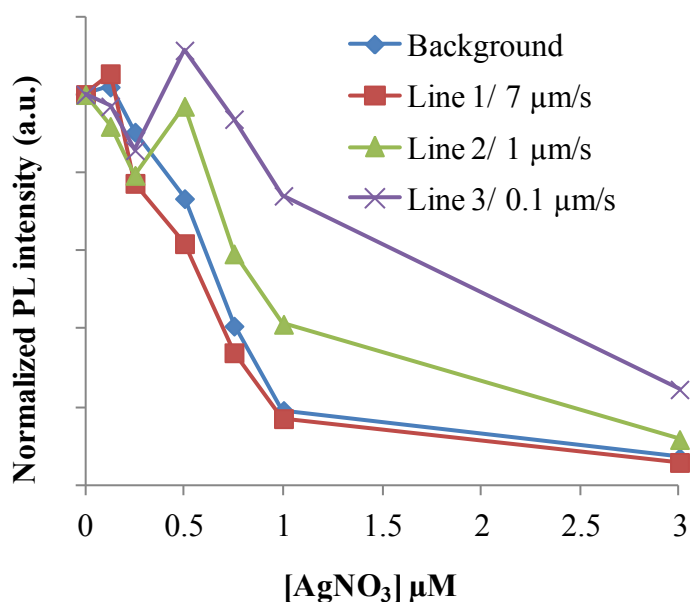


Figure 2. 20 Photoluminescence intensity spectra normalized to the I_0 at λ_{max} peak position of the different lines of CdSe QDs with increasing AgNO_3 concentrations. Background plot represents unmodified CdSe QD film, while lines 1-3 are CdSe QDs that had been altered by laser power of $\sim 115 \mu\text{W}$ with speeds of 7, 1, and 0.1 $\mu\text{m/s}$.

2.9 Conclusions

In this chapter we have discussed, first, how the laser photolithography influenced the photoluminescence of CdSe QDs capped with 11-MUA. The photoluminescence intensity of the locally altered CdSe QDs was enhanced as compared to the pristine QDs. The enhancement in the photoluminescence intensity (photobrightening) was due to the oxidation and desorption of the 11-MUA capping agents. Upon prolonged exposure to the laser source, the photoluminescence of the CdSe QDs decreased (photodarkening) due to surface oxidation. When the photolithography was conducted in a solution containing the free 11-MUA ligand, the photodarkening process slowed due to the re-adsorption of the free ligand in the solution.

We have also shown that the locally photobrightened CdSe QDs altered by photolithography were more sensitive to their local environment. Upon exposure to water the local photoluminescence of the photobrightened CdSe decreased dramatically as compared to the pristine QDs. Taking advantage of those properties the interaction between CdSe QDs and Ag^+ is explored as the surface properties of the QDs are altered.

We then examined the Ag exchange reaction with CdSe using photoluminescence quenching as a function of ligand packing density and surface oxidation. From these studies, we found that the cation exchange efficiency was better on the locally photobrightened CdSe QDs (with reduced ligand coverage) and slower on the photooxidized CdSe QDs. This was confirmed by fluorescence quenching and XPS data. We assert that the partial 11-MUA ligand oxidation and removal reduced ligand packing density allowing for more facile diffusion of Ag^+ to the surface of the QDs to

undergo exchange, while oxidization of the CdSe QD surface hindered the cation exchange reaction due to the formation of insoluble SeO_2 . The n-type doping behavior where the introduction of Ag^+ ions as impurities increases the CdSe photoluminescence intensity, as observed on photooxidized CdSe QDs when reacted with a low concentration of AgNO_3 . This phenomenon was similar to literature observations of CdSe QDs with low doping with Ag^+ .¹⁰⁴ This was possible due to the slower cation exchange rate on these photooxidized CdSe QDs on an otherwise very effective and thermodynamically driven reaction on a pristine CdSe QD film. As such, by controlling capping group density and surface oxidation it is likely that the doping of CdSe can be tuned, affording additional control of their photophysical properties.

CHAPTER III

PATTERNING OF GOLD NANOPARTICLE BASED ARRAYS USING METHODS OF DIRECTED ASSEMBLY BY CHEMICAL FORCES

3.1 Introduction

The patterning of nanoparticles on various substrates has been exploited as the building block for the design of photonic, electronic, and magnetic devices for the use in sensing and optical applications.^{5, 21, 33, 43} The direct integration of these patterns is crucial for the architecture and construction of these devices. In this chapter the patterning of metallic nanoparticles, in this case Au NPs, using two unconventional lithography methods is described. In the first section, the fabrication of Au nanostructure arrays using particle lithography is introduced. Next, the integration of a patterned array of Au NPs using the combination of a self-assembled monolayer (SAM) of 3-aminopropyltriethoxy silane (APTES) as a molecular linker and polystyrene (PS) stamp is discussed. These two methods have proven to be a promising alternative for nanoscale patterning to the otherwise expensive electronic beam (e-beam) lithography technique.

3.2 Patterning Au Nanostructure Arrays via Particle Lithography

Particle lithography, sometimes known as nanosphere or colloidal lithography is a versatile and less expensive lithography technique developed as an alternative for

electron-beam lithography. As early as 1981, Fischer and Zingsheim introduced the concept by using polystyrene nanospheres as a mask for contact imaging.⁴⁵ In 1982 Deckman and co-workers integrated their concept and used the monolayer of nanospheres as both material deposition and mask.⁴⁶ Since then the use of nanospheres as an aid for nanolithography have been used to pattern different morphologies of nanostructures from a wide variety of materials, including the patterning of self assembled monolayers (SAM) and metallic nanostructures.^{16, 40-43} In our recent paper we have demonstrated the use of PS MS as templates for the formation of CdSe QDs ring array.²

Due to their localized surface plasmon resonance (LSPR), metallic nanostructures such as Au and Ag have lent themselves to a wide range of application.^{117, 118} Some of these applications require the shift of the nanostructures' LSPR farther down into the visible near-infrared (NIR) regime.^{119, 120} Therefore it is crucial to tailor the LSPR from the typical ~520 nm of Au NPs and ~450 nm of Ag NPs LSPR frequency.^{121, 122} One limitation for spherical Au NPS is that a red shift of only about 70 nm is observed by changing their sizes from 9 nm to 99 nm, accompanied by LSPR frequency shift from 517 nm to 575 nm respectively.¹²¹ To overcome this limitation, significant efforts have been made to tune the geometrical shapes of such particles into triangles, rods, cages, shells and rings.^{9, 119, 123, 124} Because of that, the fabrication of metallic nanostructures patterned array with different morphologies such as dots, donuts, and non-symmetric ellipses – with variations of parameters such as their

radius, inner and outer ring radius and distance separation – have been explored for the study of their LSPR.^{41, 125, 126}

One of the driving forces for the assembly of these structures via particle lithography is capillary force. For the ring formation to occur the magnitude of the capillary force (F_{cap}) needs to be greater than the sum of the opposing forces such as adhesion (F_{adh}), double layer force (F_{dl}) and frictional force (F_{fric}).² In this paper, 2.5 μm PS MS (6×10^9 microspheres/ml) were used as a template for the formation of Au nanostructure arrays of 20 nm 11-MUA capped Au NPs. Changes in experimental conditions such as the relative humidity, RH, and relative nanoparticle concentration to PS MS, can influence the magnitude of those forces and alter the formation of the pattern array. This paper will discuss how the humidity and the concentration of Au NPs can alter the morphology of these nanostructures assembled by particle lithography.

3.2.1 Experimental Procedure

3.2.1.1 Synthesis of Au NPs

Au NPs were synthesized by the reduction of $\text{HAuCl}_4 \cdot 3\text{H}_2\text{O}$ (Sigma Aldrich) with sodium citrate.¹²⁷ The size of the citrate-stabilized gold NPs was estimated at ~ 20 nm in diameter based on the maximum surface plasmon absorbance in the UV-visible spectra (USB-ISS-UV/vis, Ocean Optics Inc.) at 523 nm. TEM images of isolated Au particles also confirmed the size to be 20 ± 4 nm.

3.2.1.2 Au NPs ligand exchange to 11-MUA

As synthesized citrate stabilized Au NPs underwent further processing to exchange the capping agent to 11-MUA. The procedure is as follow:¹²⁸ 1 mL of 10 mM 11-MUA in ethanol was added to 10 mL of as synthesized Au NPs under vigorous stirring. Stirring was continued for at least 60 hours in the dark. The mixture was then centrifuged at 8000 rpm for 60 minutes (Beckman J2-21), and the supernatant was replaced with 18.2 M Ω .cm nanopure water (NANOpure Diamond, Barnstead) that was adjusted to pH 11 by NaOH. The washing procedure was repeated twice to ensure removal of unbound excess ligand. The resulting Au NPs were characterized by UV-visible spectra and TEM and stored under dark conditions future use.

3.2.1.3 Microspheres preparation

Polystyrene (PS) microspheres of 2.5 μ m in size were purchased from Duke Scientific (Fremont, CA). The spheres were repeatedly centrifuged for 5 minutes at a time before being resuspended in ultrapure water to remove surfactant molecules from the solution. This centrifugation/resuspension process was repeated 8 times.

3.2.1.4 Preparation of substrates

Glass cover slides #2 (VWR) were cleaned by sonication in ethanol for 15 minutes. Next, the clean glass slides were modified with polyvinylpyrrolidone (PVP, Sigma-Aldrich, M_w 55000). PVP-modified surfaces were prepared by soaking freshly prepared glass substrates in a 1% PVP ethanol solution overnight. The samples were

then rinsed sequentially with ethanol and purified water for 1 minute each. Finally, the samples were dried by blowing with nitrogen.

3.2.1.5 Colloidal lithography by 2.5 μm PS microspheres

The 1:1 mixture that contained $\sim 6 \times 10^9$ spheres/ml and $\sim 7 \times 10^{11}$ or 40×10^{11} Au NPs/ml was introduced into the PVP modified cover slip in a dropwise fashion ($\sim 1.5 \mu\text{L}$ droplets). The samples were then placed inside a chamber where humidity was kept constant within 5% overnight. Scotch tape was then used to remove the PS microspheres that were used as a template, leaving array of Au nanostructures on the substrate.

3.2.1.6 Characterization by atomic force microscopy (AFM)

AFM images of the Au nanostructures were taken with a combined AFM/confocal WITec Alpha 400. All AFM images were acquired under ambient conditions in tapping mode using commercially available aluminum-coated silicon AFM tips from Nanoscience Instrument (Phoenix, AZ) with nominal tip radii of less than 10 nm and nominal spring constants of 48 N/m.

3.2.2 Formation of Au Nanostructure Array

In this study, Polystyrene microspheres of 2.5 μm in diameter were used as templates. The microspheres self-assembled into a hexagonal close-pack array as shown in Figure 3.1.

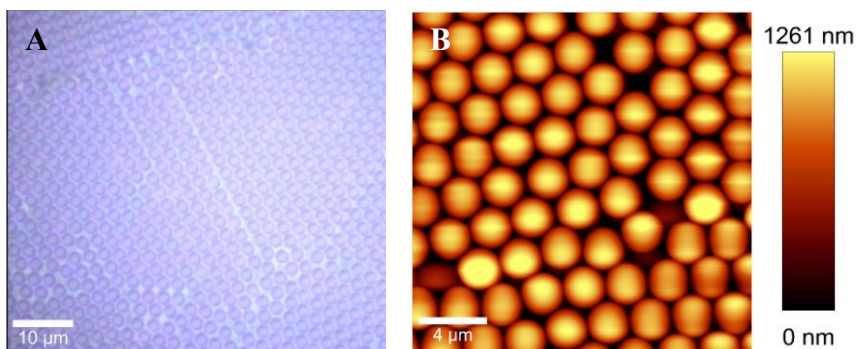


Figure 3. 1 (A) Optical image and (B) AFM image. Of the self-assembly of 2.5 μm in diameter polystyrene microspheres dropcasted on micro cover glass #2.

A hexagonal patterned array of Au nanostructures was fabricated by a previously developed particle lithography method² outlined in Figure 3.2. The concentration of polystyrene microspheres (PS MS) was 6×10^9 microspheres/mL and kept constant throughout the experiment, while two different concentrations of Au NPs solutions were used. These measured at 7×10^{11} and 40×10^{11} Au NPs/mL as determined by UV-Vis spectroscopy.¹²⁹ The 20 nm Au NPs were stabilized with 11-MUA and characterized with UV-Vis spectroscopy and TEM as shown in Figure 3.3. Figure 3.4 shows the Au nanoring arrays formed at 45% RH with the higher Au NPs concentration after rinsing with ethanol. The average height of the rings after the rinsing treatment was 23 ± 5 nm. This height was less than the average height of 36 ± 10 nm from the unwashed sample due to the loss of loosely bound particles as shown in Figure 3.5. Because of the interaction between the Au NPs and the PVP modified glass substrate, the pattern array was conserved after the ethanol rinsing. Without the PVP layer the majority of the fabricated Au nanorings were rinsed away.

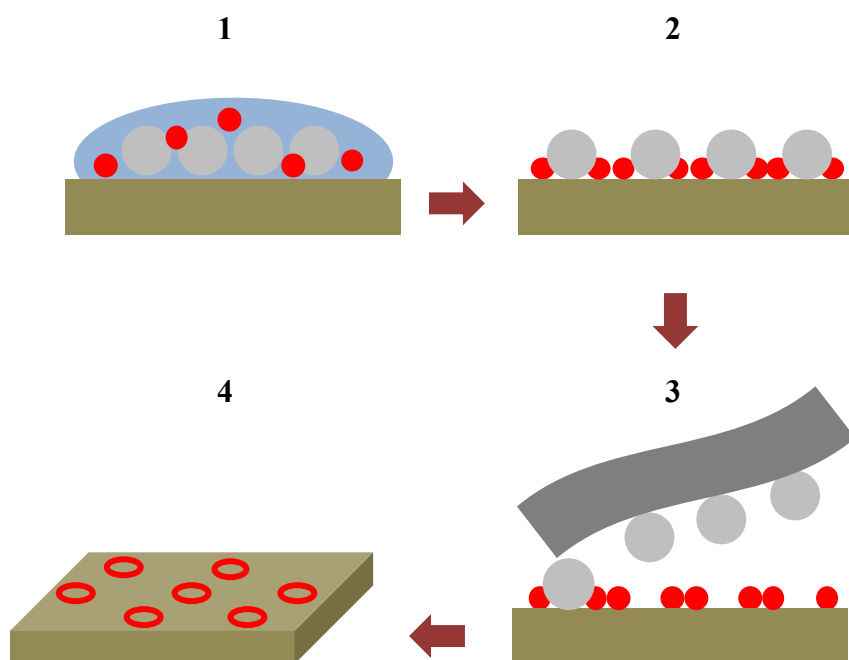


Figure 3. 2 Schematic of particle lithography. (1) A 1:1 mixture of Au NPs and PS M) dispersed in water was dropcasted on a PVP modified glass substrate; (2) as the mixture is dried the PS MS self-assembled into a close packed hexagonal array with the smaller Au NPs arranging themselves around the larger microspheres; (3) scotch tape is then used to peel the larger microspheres, (4) leaving the Au nanostructure arrays on the substrate.

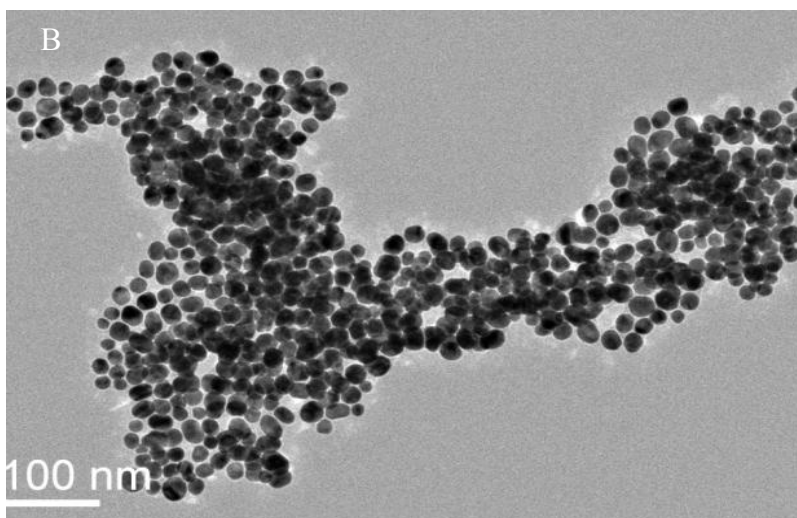
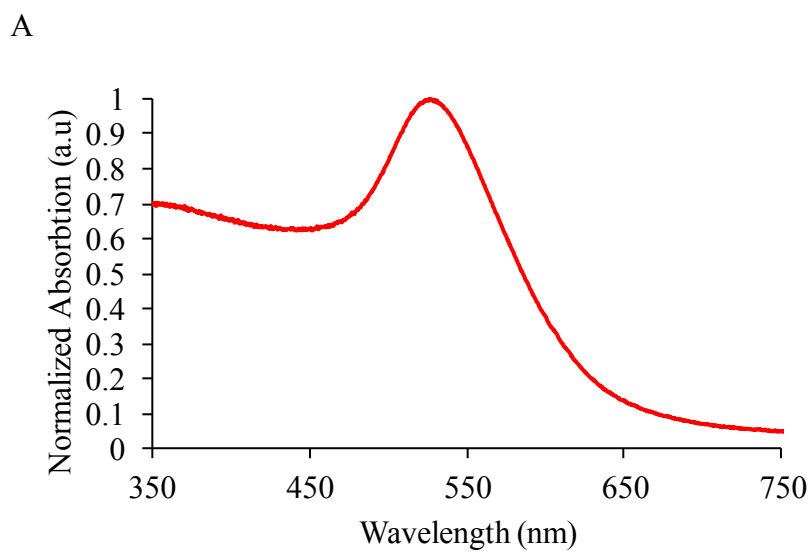


Figure 3. 3 (A) UV-visible spectra of Au NPs stabilized with 11-MUA and its localized surface plasmon resonance (LSPR) at 525 nm. (B) TEM images of the 20 nm Au NPs.

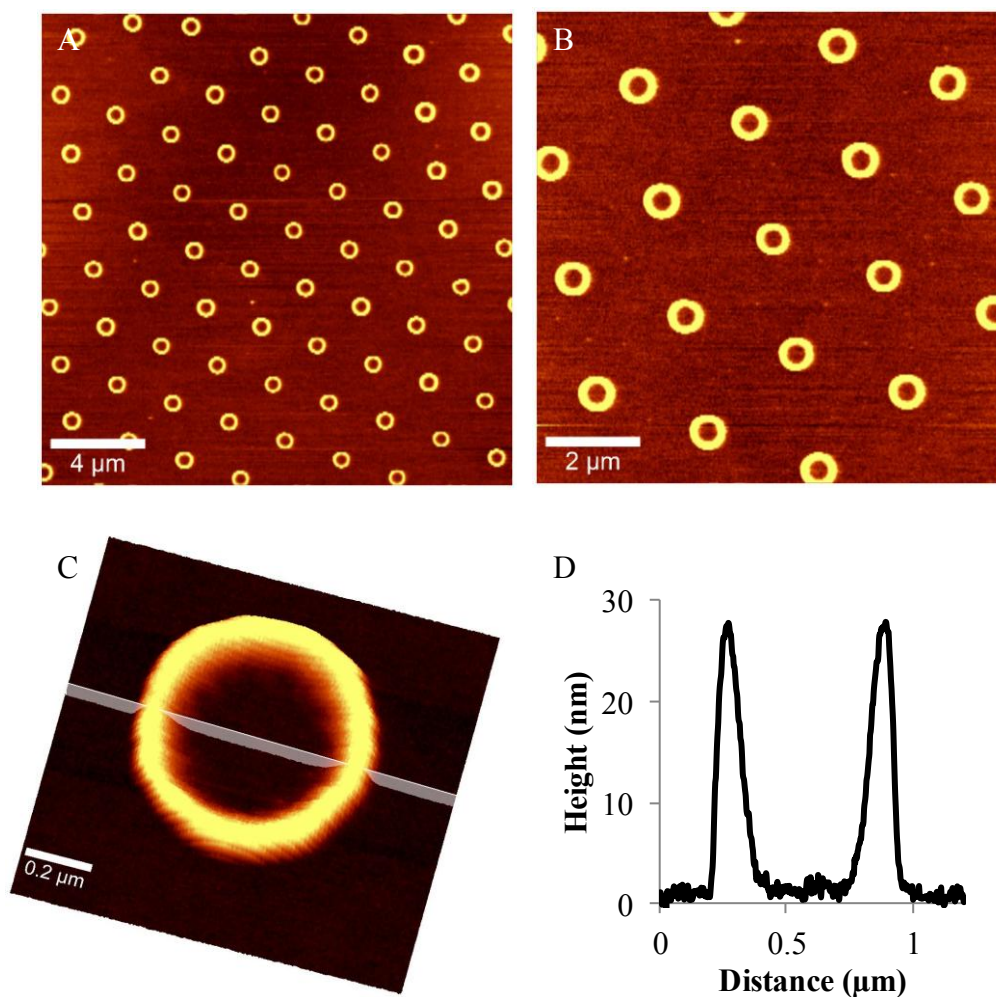


Figure 3. 4 Au nanoring arrays fabricated using particle lithography. (A-C) AFM AC images of Au nanoring arrays assembled on PVP modified glass substrate at 45 % RH with Au NPs concentration of 40×10^{11} Au NPs/mL after scotch tape peel and ethanol rinse. (C) Enlarged image of the Au nanoring with its cross-section (D).

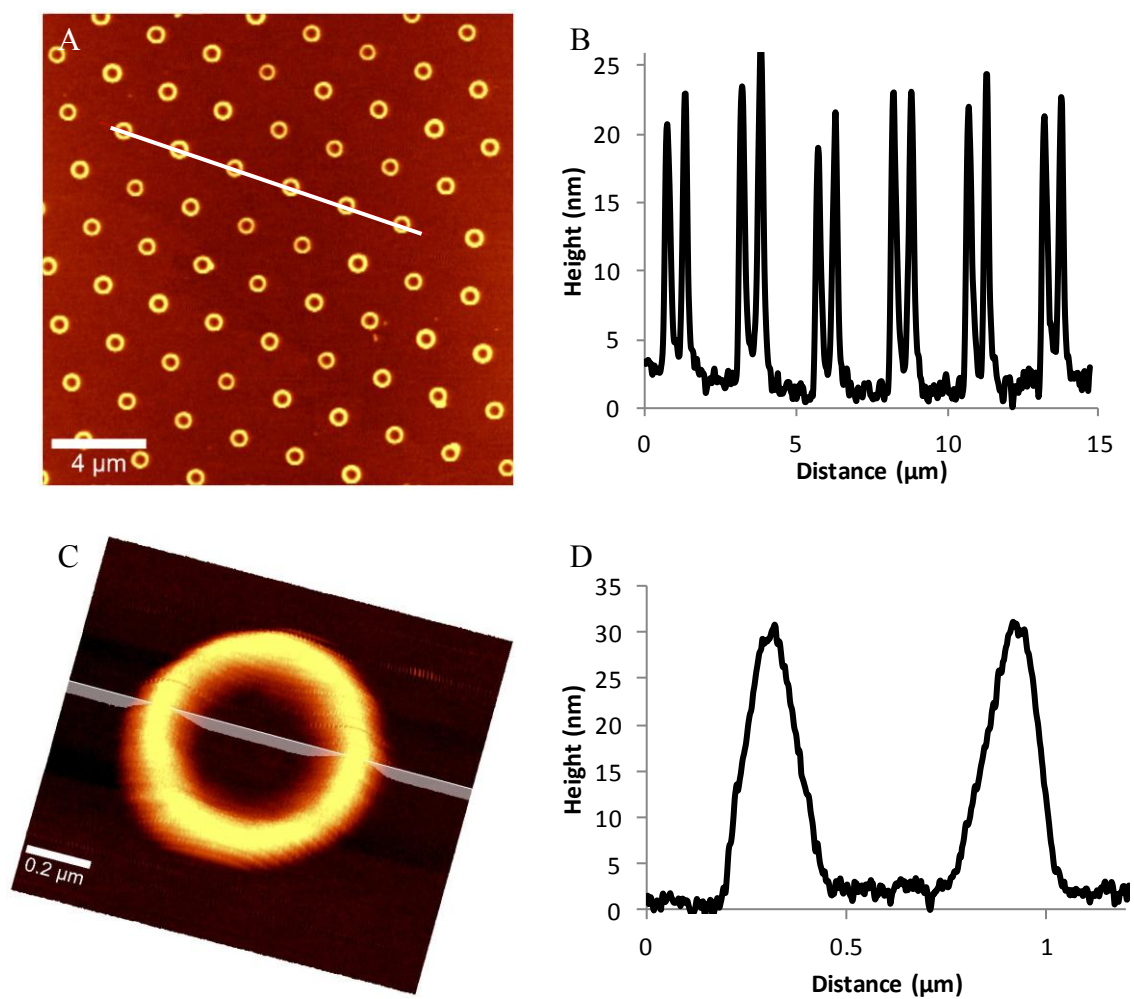


Figure 3. 5 Atomic Force Microscopy (AFM) images of Au nanoring structures with concentration of 40×10^{11} Au NPs/mL under 45% RH and their corresponding cross sections before rinsing treatment with ethanol.

Different morphologies of Au nanostructure arrays were observed when the experimental conditions were altered. Figure 3.6 shows Au nanodonuts formed by using a lower concentration of Au NPs in a 65% RH after the ethanol rinsing treatment. From these images we can see that the structures are composed of what appears to be individual particles, unlike the composition of nanorings structures shown in Figure 3.4 and 3.5, which consist of a condensed agglomeration of Au NPs. The average height of the nanodonut structures is 10 ± 2 nm. Upon washing with ethanol the height of the nanodonuts decreased from 12 ± 2 nm as shown in Figure 3.7. The height of these nanodonuts' structures is slightly smaller than the size of a single Au NPs. It is possible that the Au NPs are partially imbedded in the soft PVP matrix. The height of the polymer matrix is 8 ± 1 nm as determined by AFM scratching (Figure 3.8). When the experiment was conducted using a bare glass substrate without the PVP polymer, the resulting structures that survived the rinsing treatment have an average height of a single Au NPs ~ 20 nm as shown in Figure 3.9

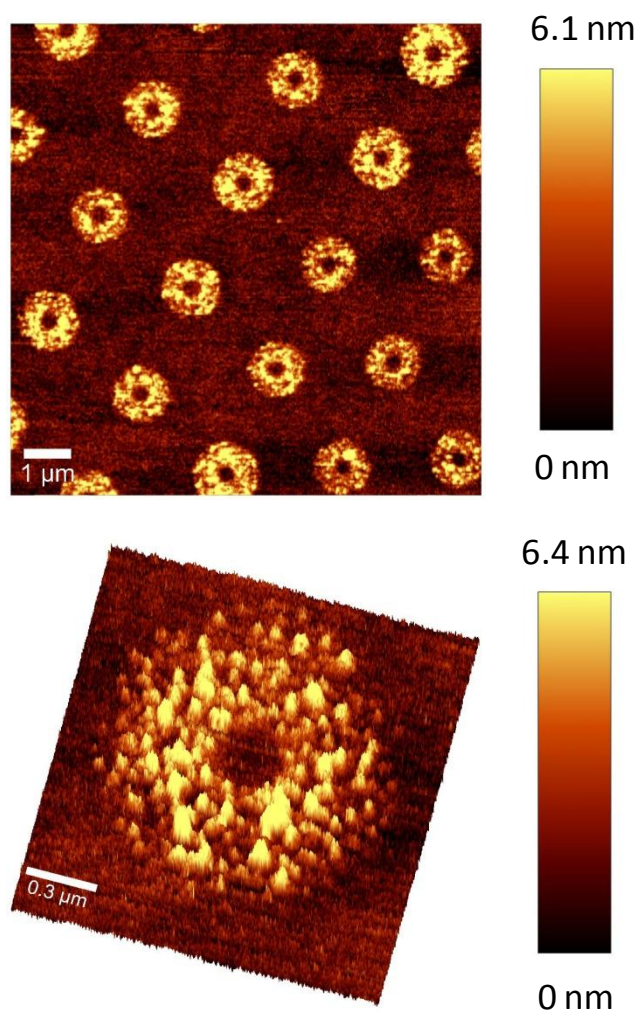


Figure 3. 6 AFM AC topography image showing Au NPs donuts array on PVP modified glass substrate.

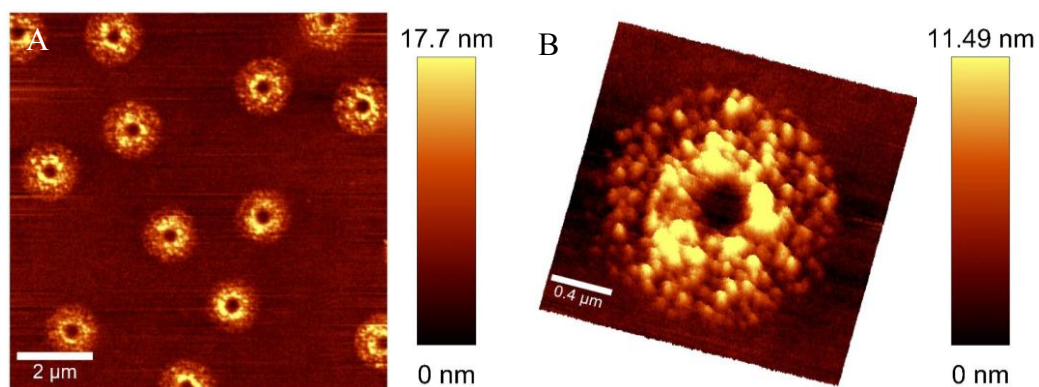


Figure 3. 7 AFM images of Au nanodnut arrays using a lower Au NPs concentration of 7×10^{11} Au NPs/ml at 65% RH before rinsing with ethanol.

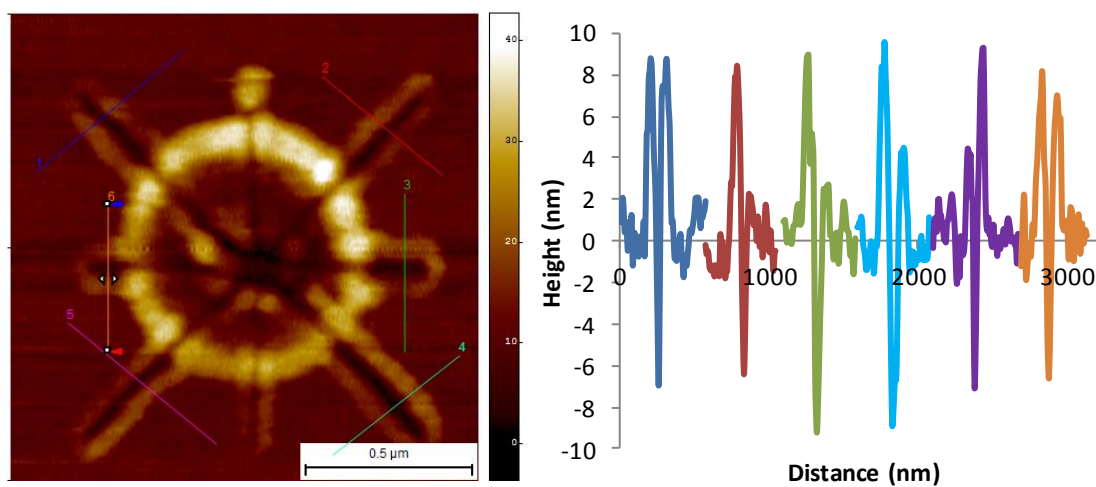


Figure 3. 8 AFM image from AFM scratch experiment showing the thickness of the PVP polymer layer as shown in the corresponding cross sections graph with an average of 8 ± 1 nm.

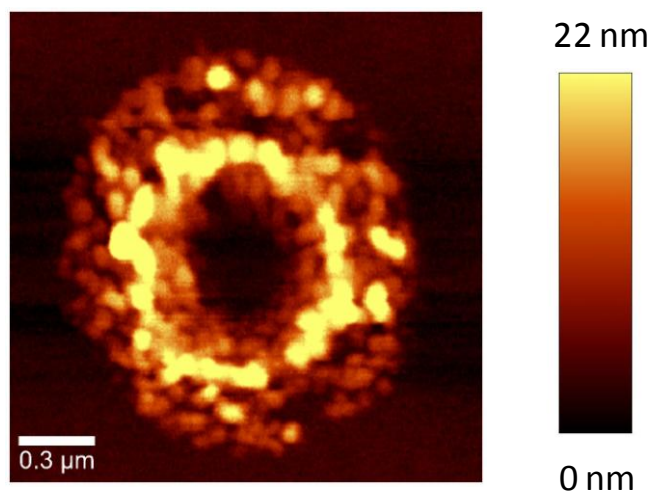


Figure 3. 9 AFM image of nanodonor structure assembled on bare glass without PVP after ethanol rinse.

3.2.3 The Influence of Relative Humidity to the Au Nanostructure Arrays Formation

We are able to calculate the dimensions of the nanostructures from the experimental AFM images and data shown in Table 3.1. The Au nanorings had inner diameters (D_{in}) of 394 nm, outer diameters (D_{out}) of 881 nm, with D_{out}/D_{in} of 2.3. The Au nanodonor arrays dimensions are $D_{in}=250$ nm, $D_{out}=1387$ and $D_{out}/D_{in}=5.6$. The dimensions for the Au nanoring arrays can be approximated using the hard sphere model shown on Figure 3.10 to calculate r_{ring} :

$$r_{ring} = \sqrt{(r_{MS} + r_{Au})^2 - (r_{MS} - r_{Au})^2} \quad (4)$$

With $r_{MS} = 1.25 \mu\text{m}$ and $r_{Au} = 20$ nm, the calculated r_{ring} is 224 nm, giving $D_{in} = 448$ nm, this value matches close to the experimental data of nanoring arrays.

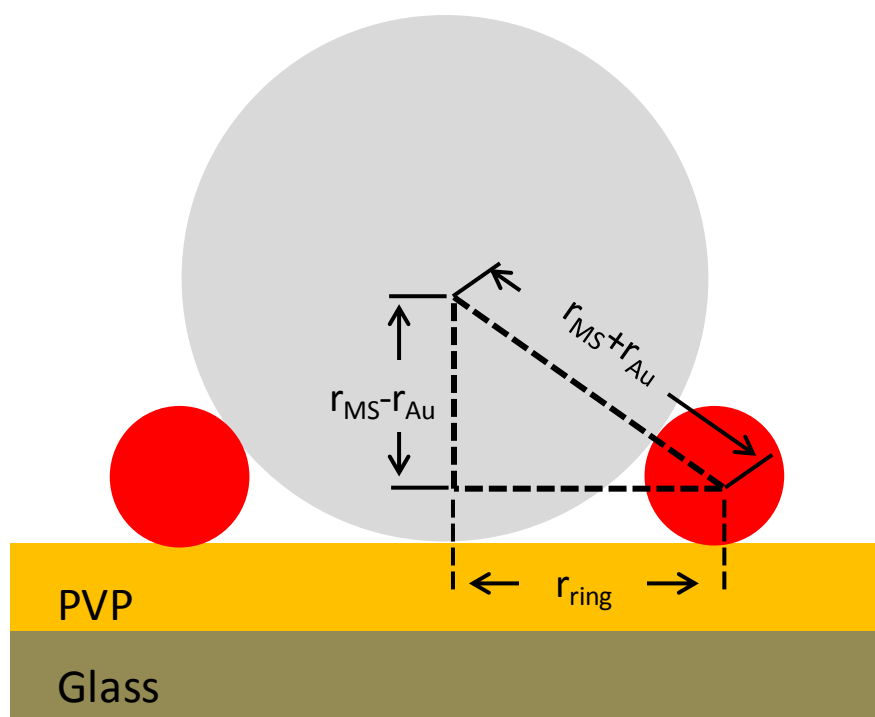


Figure 3. 10 Schematic using a hard sphere contact model approximation to calculate r_{ring} . Note that drawing is not to scale.

Table 3. 1 Au nanorings and nanodunuts dimensions tabulated from AFM images, units are in nm.

	D_{in}	D_{out}	$D_{\text{out}}/D_{\text{in}}$
Au rings	394 ± 51	881 ± 101	2.3 ± 0.3
Au donuts	250 ± 32	1387 ± 112	5.6 ± 0.6

The dimensions of the nanodonuts structures deviated greatly from the r_{ring} calculated by the model shown on Figure 3.10. The much smaller D_{in} of the nanodonut structures indicated that the Au NPs were able to move closer into the PS MS perimeter. Previously shown on AFM measurements data in Figures 3.6 and 3.8, the Au individual Au NPs are partially embedded in the PVP matrix. This failed the assumption made for using hard sphere contact model approximation for this system. Figure 3.11 depicts a much better approximation for the formation Au nanodonut arrays. Using the D_{in} dimensions of the Au nanodonut arrays, the value x and Au AFM as depicted in Figure 3.11 can be calculated using equation (5). The calculated Au AFM value matched the ~ 6 nm experimental value as shown on Figure 3.6.

$$r_{donut} = \sqrt{(r_{MS} + x)^2 - (r_{MS})^2} \quad (5)$$

The discussed phenomenon explained how humidity played a role in the formation of the Au nanorings or nanodonut structures. In addition to the RH, the Au NPs concentration serves as a determining factor into the formation of both structures. The nanodonut arrays only occur when a lower concentration of Au NPs is used under a high RH environment. To explain the experimental data we postulate that:

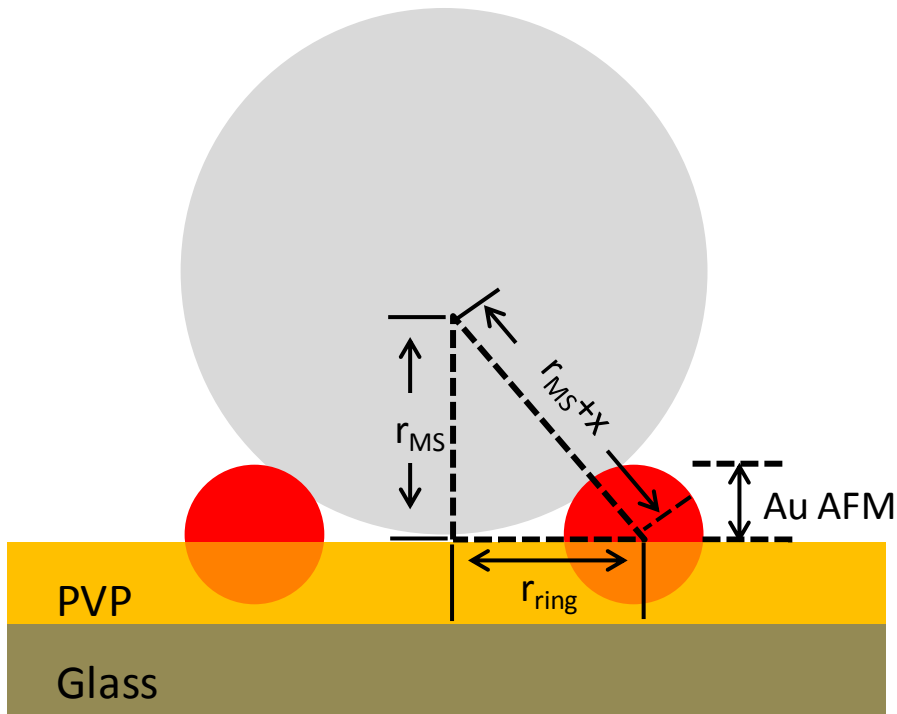


Figure 3. 11 Schematic of Au nanodonor arrays formation showing Au NPs partially embedded in the PVP matrix. Note that drawing is not to scale.

1. At higher RH value, the evaporation of the liquid capillary proceeded at a longer time period in comparison to the system performed at a low RH value. The lower concentration of Au NPs when compared to the high Au NPs solution with the same volume, contained a higher percentage of water in the capillary. In our system, the difference in the concentrations of the Au NPs solutions was five folds. But, as the system evaporates down to the volume of the liquid capillary bridge, the originally five folds more concentrated Au NPs will be more concentrated than the lower Au NPs concentration. The slower evaporation rate combined with the system of lower Au NPs concentration with higher water content, further increased the evaporation of

the system. This allowed for the Au NPs to be partially embedded in the PVP matrix, as shown by the AFM data in Figure 3.11. This also allowed for the individual nanoparticles to move closer into the PS perimeter, resulting in the smaller D_{in} for the nanodonor arrays.

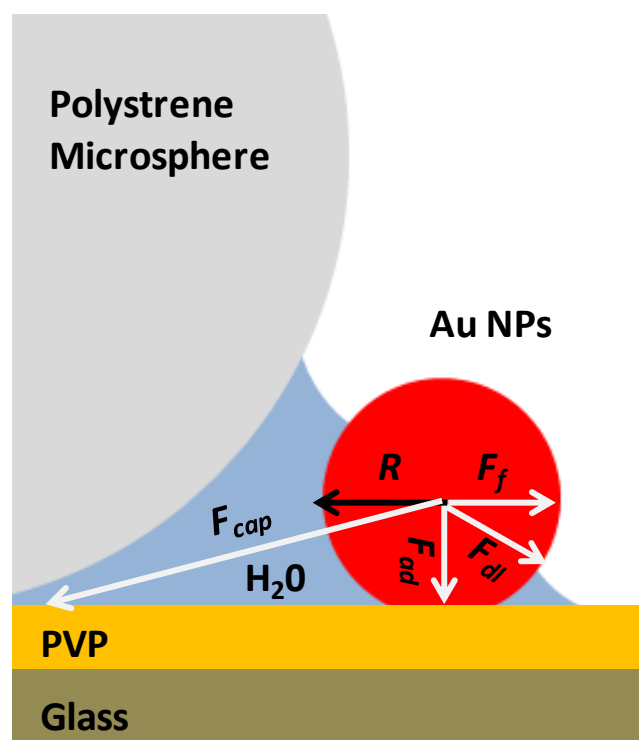


Figure 3. 12 Schematic diagram showing the forces involved in dragging the Au nanoparticle to polystyrene spheres. Note that the drawing is not to scale. Moreover, there is almost certainly a hydration layer that covers the entire hydrophilic Au nanoparticle, which has not been explicitly drawn.

2. The higher concentration of Au NPs has a higher ionic strength originating from the negatively charged 11-MUA ligand, and NaOH in the solution. The ionic strength relates to the Debye length (i.e. electrostatic shielding between the particles), where the Debye length κ^{-1} is inversely proportional to the ionic strength I . The reduced Debye length is due to the screening effect from an increased ionic strength as the Au NPs concentration is increased.¹³⁰ Hence in the case of the lower concentration of Au NPs, the repulsive force between each NP is greater, preventing the formation of a condensed ring structure. As stated previously for the formation of the ring to occur, F_{cap} must be greater than the sum of all the opposing forces ($F_{\text{adh}}+F_{\text{dl}}+F_{\text{fric}}$),¹³¹ as also shown in Figure 3.12. It was possible that in the low concentration system, the repulsive double layer force between the Au NPs was large and counteracted F_{cap} . As also observed, the D_{out} of the nanodonut arrays was also larger in comparison to the nanoring arrays, in agreement with the postulated increasing repulsion force between each individual nanoparticle.

When both the RH and Au NPs concentrations were varied and these two factors could influence the formation of these nanostructures as shown in Figure 3.13. The low concentration of Au NPs appears to form a condensed ring structures for the lower RH value, transforming into donut structures at a higher RH value. While the higher concentration of Au NPs formed uniform ring structures at ambient $\sim 45\%$ RH, at a lower RH of 30%, jagged ring structures are formed. Further, at a higher humidity of 65%, less uniform ring structures were formed. Supporting our previous argument, the lower Au NPs concentration provides an environment for self-assembly into ring

nanostructures at a lower RH when compared to the high concentration of Au NPs. The higher water content in the capillary of the system with the lower concentration requires a lower RH for the ring formation to occur. Conversely, when the higher Au NPs system was assembled under a low 30% RH, the system dried too quickly before the NPs are able to form uniform ring structures around the PS MS. This resulted in jagged ring structures with non-uniform aggregation of Au NPs on its side.

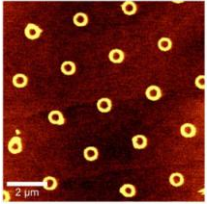
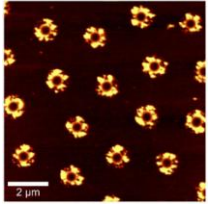
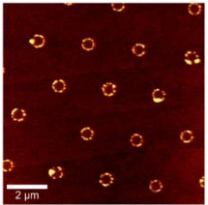
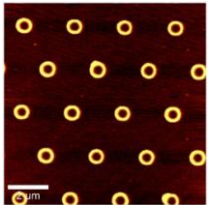
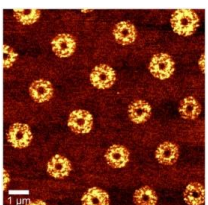
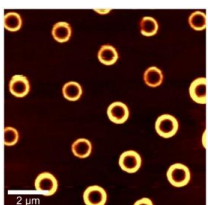
Au NPs Conc. %RH	Low (7×10^{11} Au NPs/ml)	High (4×10^{12} Au NPs/ml)
Dry ~ 30%		
Ambient ~45%		
Humid ~65% RH value is controlled within 5%		

Figure 3. 13 AFM images of Au nanostructures as the humidity and Au NPs concentrations are varied.

3.2.4 Modeling the LSPR of Au Nanoring

Now that we have successfully fabricated the versatile nanostructure arrays, a closer look at their LSPR is needed. Aizpura and co-workers found that as compared to solid gold particles of similar size, nanorings exhibited a redshifted localized surface plasmon that can be tuned over an extended wavelength range by varying the ratio of the ring thickness to its radius.¹²⁴ His experimental data was backed by the simulation data solved with a numerical method using boundary element method (BEM) developed by F. J. Garcia de Abajo and A. Howie.¹³² In Au nanoring structures, there is a strong electromagnetic coupling between the inner and outer ring walls when the wall thickness is small compared to the ring radius. Therefore the plasmonics of the metallic nanoring structures can be described as the interaction of “hybridization” of the plasmons of metallic nanostructures of simpler shapes. The LSPR of metallic nanoring can be described as the interaction between plasmons of nanosphere and cavity.⁷⁰

Metallic nanoparticles boundary element method (MNPBEM) MATLAB toolbox is a developed numerical method using BEM designed for the simulation of plasmonic nanoparticles.^{63, 133, 134} It was designed to solve Maxwell's equations for a dielectric environment where bodies with homogeneous and isotropic dielectric functions are separated by abrupt interfaces. This approach is suitable and tested for metallic nanoparticles with size ranging from a few to a few hundreds of nanometers.⁶³ With this method, only the boundaries between the different dielectric materials is discretized and not the whole volume. Here, MNPBEM was used to simulate the LSPR of our Au nanorings. For the purpose of this study, the value of the dielectric chosen is the average

value between glass and air,¹³⁴ and the dimensions of the rings used are those of tabulated on Table 3.1, with $D_{in} = 394$ nm and $D_{out} = 881$ nm. The simulated Au nanoring structure and its LSPR is shown in Figure 3.14

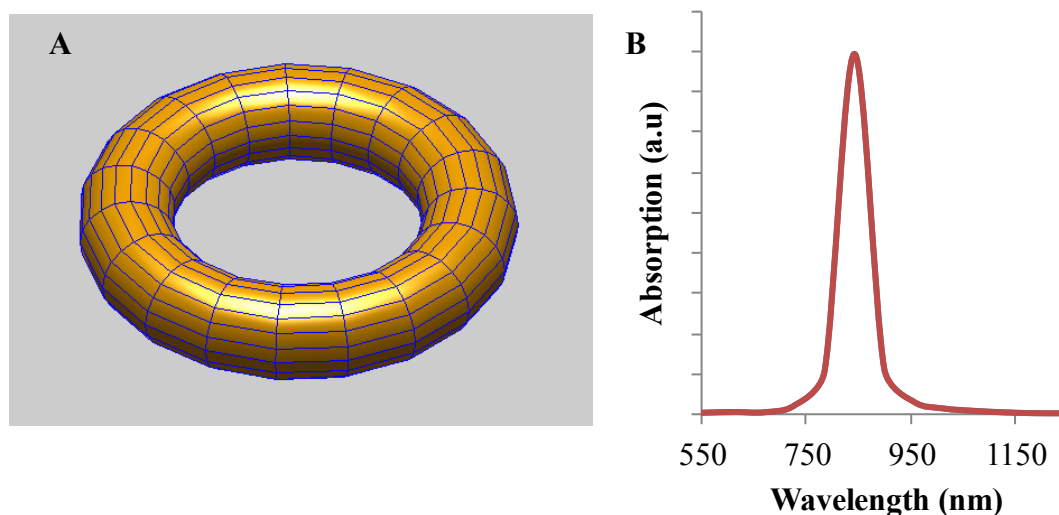


Figure 3. 14 (A) Nanoring structure modeled by MATLAB MNPBEM and (B) its corresponding calculated LSPR.

3.3 Patterning Array of Au NPs via 3-Aminopropyltriethoxy Silane (APTES) by PS Stamp

Molecular linker has been used to immobilize nanomaterials on a substrate. Some examples for this include the use of molecular linkers such as: mercaptopropyltrimethoxy silane (MPTMS)²⁶ and mercaptopropionic acid (MPA)^{27, 28} for immobilization of CdSe, CdS QDs and Au NPs,^{29, 30} 3-aminopropyltrimethoxy silane (APTES) for attachment of Au NPs.^{2, 3, 29} In this section, the use of APTES as a

molecular linker is combined with a PS mask fabricated by polydimethylsiloxane (PDMS) stamp to direct the assembly of Au NPs. The citrate stabilized Au NPs have a specific affinity to the amine group of the APTES allowing for their immobilization. Among other similar nanopatterning techniques involving the use of a PDMS stamp such as microcontact printing, this method of nanopatterning is less sensitive to its experimental condition. This method thus provides a more robust and reliable option. Microcontact printing has been shown to successfully pattern a variety of nanomaterials on a wide range of substrates.³² This is achieved either by direct NPs transfer^{34, 35} or via the transfer of a molecular ink to allow for the specific adsorption of the target nanomaterials.³³ The drawback with the common technique of microcontact print is its sensitivity to experimental parameters that influence the pattern reproducibility.³² Those parameters include relative humidity (RH) value, inking time period, and force applied during microcontact print. The nanopatterning method described in this section can be described as a modification of microcontact printing technique. The PDMS microstamp is used to direct the assembly of the PS mask onto a SAM pre-functionalized substrate. The hybrid between the selective binding by through a molecular linker and the masking process by polystyrene is shown to create a pattern array of Au NPs with minimal non-specific binding.

3.3.1 Experimental Procedure

3.3.1.1 Substrate preparation

For the patterning of Au NPs array via APTES, the substrates glass cover slides #2 (VWR) or Si wafers (100) were cleaned by a standard wafer cleaning method. The substrate was immersed in a mixture of 4:1:1 (v/v) of H₂O:H₂O₂:NH₄OH at 85°C for 15 min, followed by rinsing with copious purified nanopure water.

3.3.1.2 Self-assembled monolayer (SAM) of APTES

The SAM of APTES was prepared by immersing the glass or Si (100) substrate into a 5 mM APTES solution in ethanol overnight. Upon APTES immobilization, the sample was then rinsed with copious amounts of ethanol and dried with stream of nitrogen.

3.3.1.3 Preparation of PDMS microstamp

The PDMS stamp was fabricated by combining a mixture of 10:1 (v/v) of PDMS silicone elastomer base:curing agent (Dow Corning). This mixture was then poured over an AFM z calibration structure TGZ03 with $\Delta Z \sim 500\text{nm}$. (Mikromasch). The PDMS was then cured for 1 - 2 hours at 85°C. Once the PDMS structure hardened, it was then removed from the calibration structure. The resulting PDMS stamp was then cut to size and stored in ethanol to avoid dust contamination.

3.3.1.4 Fabrication of PS mask

The PDMS stamp was placed face down on a freshly prepared APTES modified substrate. Both the substrate and the PDMS stamp were then set on top of a hot heating plate kept at 110°C. A 15 μ L mixture of 1% (w/w) PS *MW*_280,000 in toluene was dropcasted on the corners around the PDMS stamp on the heated stage and left heated for 2 minutes. *Note: The PS solution needed to be dropcasted as soon as the glass slide is placed on the heating stage. Do not let the glass slide get too hot, the toluene will evaporate fast.* The sample was then taken off the hot plate and left to cool for ~20 minutes. Once cooled, the PDMS stamp was then removed, leaving the PS mask behind.

3.3.1.5 Patterning of Au NPs array

The resulting PS mask that was assembled on the APTES modified substrate was then immersed in a solution of Au NPs stabilized by citrate overnight. Upon the immobilization of Au NPs, the sample was then rinsed with copious nanopure water and dried with nitrogen. The PS mask was then removed by immersing the sample in toluene for 2 minutes, followed by toluene and ethanol rinsing, leaving the patterned array of Au NPs.

3.3.2 The Fabrication of Au NPs Patterned Array

In the previous section, we have discussed the use of PS MS to direct the assembly of Au NPs to form nanostructure arrays. Expanding the use of PS as an aid for nanoscale lithography, self-assembled monolayer of APTES can be used in conjunction

with PS stamp for the patterning Au NPs. The schematic of the procedure modified from a published work¹³⁵ is described in Figure 3.15. In brief, upon immobilization of APTES on either a glass or Si (100) substrate, previously fabricated PDMS microstamp, can be used to direct the patterning of PS mask on the surface. The fabricated sample is then immersed in a solution containing Au NPs overnight followed by immersion in toluene for PS lift-off.

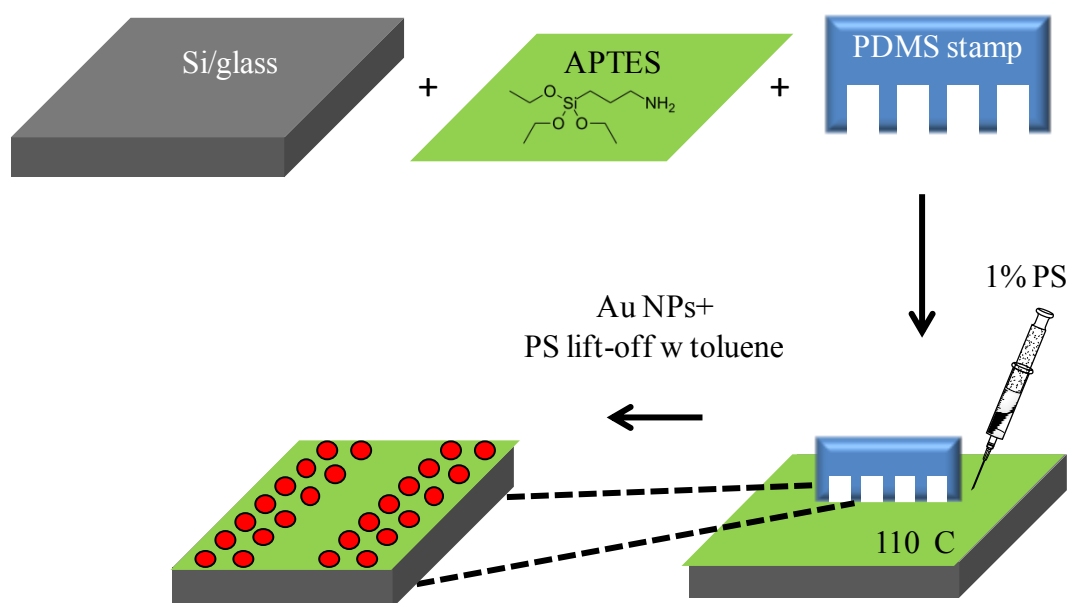


Figure 3. 15 Schematic of the fabrication of Au NPs patterned array using PS stamp via APTES.

Figure 3.16 shows an AFM image of the fabricated PS mask on glass. The height of the PS mask was in agreement with the height of the structure used as a master for PDMS stamp fabrication which is about 500 nm. The area that was protected by PS mask did not have a direct contact to the available Au NPs. Hence, after the immersion to Au NPs and PS mask lift-off by toluene, the Au NPs are selectively immobilized at the area unprotected by the mask. This can be seen in figure 3.17 showing an AFM image of a pattern of monolayer Au NPs.

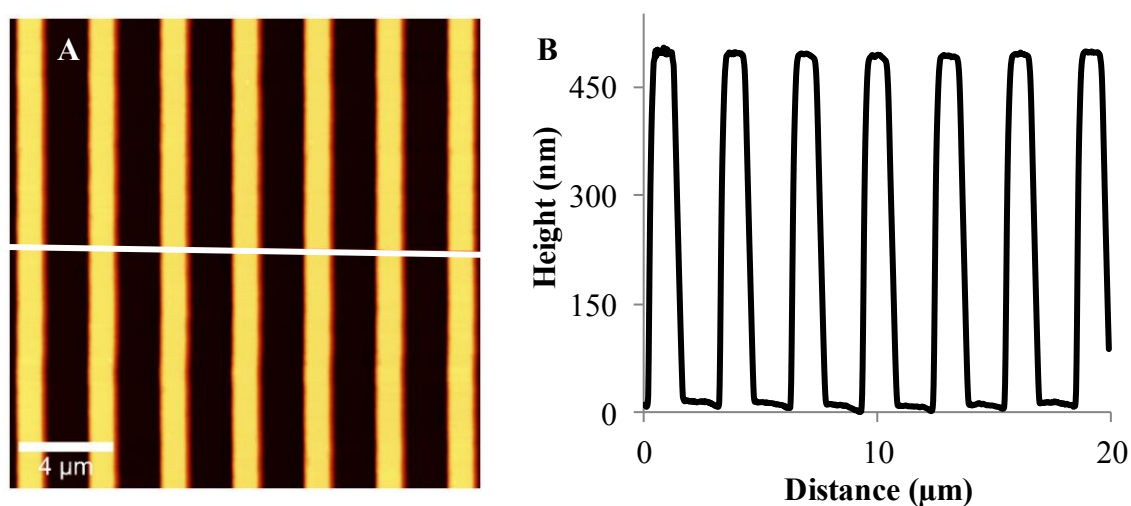


Figure 3. 16 AFM AC image of PS stamp with its corresponding cross section.

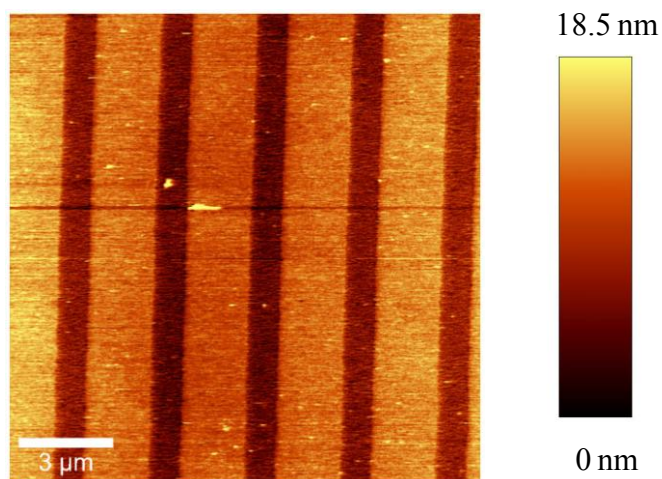


Figure 3. 17 AFM image of Au NPs array fabricated by PS stamp via APTES molecular linker.

3.4 Conclusions

Capillary force is the main driving force for the formation of the Au nanoring arrays via particle lithography. The balance between F_{cap} and the rest of the opposing forces F_{adh} , F_{dl} , F_{fric} plays an important role in the formation of the nanostructures. As the RH and the concentration of Au NPs are varied, the balance between these forces shift, which alters the morphologies of the formed nanostructures. Uniform nanoring structures were assembled at 45% RH by using the 40×10^{11} Au NPs/mL concentration. The lower Au NPs concentration of 7×10^{11} Au NPs/mL formed the nanoring structures at a lower RH of 30%. By increasing the RH to 65% and using the lower Au NPs concentration, the morphology of the nanostructures could be altered from nanorings into nanodonuts. The higher RH value, combined with the lower Au NPs, resulted in

higher water content of the system. This leads to a slower evaporation process of the capillary. This allowed for the Au NPs to be partially embedded in the PVP matrix, as shown by the AFM data in Figure 3.11. This also allowed for the individual nanoparticles to move closer into the PS perimeter, resulting in the smaller D_{in} for the nanodonor arrays, while the larger D_{out} value of the nanodonor arrays as well as the sparsely located NPs in the nanodonor arrays, can be explained by the increase repulsion between each individual nanoparticle. Knowing how the formation of these Au nanostructure array via particle lithography can be affected by changing experimental conditions is crucial to better understand how these nanostructures are formed.

Another method of patterning Au NPs array was also explored. The combination between the use of a molecular linker, APTES, and PDMS stamp to create PS mask were employed to selectively pattern Au NPs with minimal non-specific binding. Citrate-stabilized Au NPs were shown to selectively bind to the area unprotected by PS mask. As discussed in the previous section, experimental conditions that directly affect the capillary force can influence the formation of the nanostructure arrays. The nanoparticle patterning using this method is independent from such parameters. This method was shown to be a versatile, simple and inexpensive method to pattern Au NPs array.

CHAPTER IV

EFFECT OF SURFACE WETTING ON THE FORMATION OF CdSe

QUANTUM DOT RINGS AND THE FABRICATION OF MULTICOLOR

ARRAY CdSe RINGS

4.1 Introduction

As discussed, the formation of Au nanostructure arrays is highly dependent upon the capillary force (F_{cap}) acting on the system. Previous work has shown that particle lithography can also be used to create pattern array of semiconductor QDs.² The self-assembly of the QDs is driven by the capillary force at the front of the drying meniscus under the microsphere. Since the capillary force is weak, QDs often remain behind a meniscus as non-specific binding on the substrate surface. To overcome this issue, we will demonstrate a stepwise wetting and drying process that can eliminate the non-specific binding of CdSe semiconductor QDs during the pattern array ring-formation. As such, the wetting and drying processes was repeated to minimize the non-specific binding. Directly adding water to the dried pattern destroyed the pattern of the microsphere template. Therefore, the wetting procedure was achieved by cooling down the substrate to allow for condensation of a thin layer of water on the glass slides. This thin layer of water will not affect the hexagonal pattern of the microspheres and QD rings. Different condensation time periods as well as condensation cycles were

conducted for this study. In the case of a prolonged condensation period, a case of “over-wetting” is observed causing broken rings, dots as well as dots in the rings structures.

In this chapter, the laser photolithography technique discussed in Chapter II was employed to manipulate the photoluminescence of the CdSe nanoring arrays. As discussed in Chapter II, aside from photobrightening and photodarkening, the photoluminescence blue shift was also observed when CdSe QDs were altered by the laser. The photoluminescence blue shift of the individual CdSe nanorings is explored in detail in this chapter. The shift of the photoluminescence peak maximum to a lower wave number, or blue shift, has been observed for QDs as they are exposed to a laser source. A gradual blue shift of CdSe quantum dots illuminated in air has been previously observed at room temperature by Brus and co-workers as early as 1994.¹³⁶ Since then, the photoluminescence blue shift on CdSe QDs has been observed by many other researchers including our group’s previous work.^{2, 137, 138} Aside from CdSe QDs, a blue shift as large as 100 nm has been observed in PbSe QDs when exposed to a 633 nm HeNe laser in air.¹³⁹ It is widely accepted that this photoluminescence blue shift is attributed to the decrease in the effective core radius of the QDs due to the formation of the outer oxide layer.¹¹² As previously shown in Chapter II, Figures 2.3 and 2.4, a blue shift of approximately 20 - 30 nm was observed for our QDs after lithography process. According to published optical spectra,¹⁴⁰ the 20 - 30 nm blue shift in the photoluminescence peak is attributed to a decrease of 0.6 - 0.8 nm of particle diameter. Taking advantage of their photoluminescence blue shift, post-synthesis modification of larger QDs into smaller QDs has been explored as an alternative synthetic method to

produce small CdSe QDs.¹³⁸ Otherwise, the synthesis of such small CdSe quantum dots with high quality and good quantum efficiency is difficult using traditional synthesis.

In this work the post-synthesis modification of the CdSe QDs was performed after nanostructures fabrication on the substrate. In this chapter specifically, the post-synthesis modification via laser photolithography was employed on the previously fabricated CdSe nanoring arrays. Changing the laser dwelling time created an array of CdSe QDs rings with a range of emission colors. This method allowed for the facile patterning of different sizes of CdSe QDs starting from a certain size distribution of QDs. This provides a facile method to fabricate CdSe nanostructured arrays with specific optical and chemical characteristics, on the same platform. This post-synthetic photochemical modification therefore could be foreseen for the development of some QD based devices, such as: QD based light emitting diodes (LED), where each emitted color can be represented by originally the same QDs, individually tuned by photopatterning.

4.2 Experimental Method

4.2.1 Fabrication of CdSe Nanoring Arrays

The formation of the CdSe nanoring arrays using particle lithography is described in detail in the experimental method section of Chapter III. An aqueous solution of CdSe QDs capped with 11-MUA was used instead of the Au NPs. In brief, a 1:1 mixture which Polystyrene Microspheres (PSMS) was introduced into the PVP modified

cover slip in a dropwise fashion (~1.5 μ L droplets). The samples were then placed inside a chamber overnight where humidity was kept constant within 5%.

4.2.2 Step by Step Wetting Method After Particle Lithography

After dropcasting the 1:1 PS MS and QDs solution mixture as previously described, the sample was set to dry for 2 hours in 45% RH. This was then followed by immersing a glass container with micro cover glass slide containing the sample in an ice bath for ~15 seconds to allow for condensation. This was then followed by an additional drying time of ~1 hour. This was then repeated subsequently for condensation and drying processes to maximize ring formation. After five cycles of condensation process, the sample is set to dry overnight. Scotch tape was then used to remove the PS microspheres that were used as a template, leaving an array of CdSe nanostructures on the substrate.

4.2.3 Photolithography and Photoluminescence Imaging

A combined confocal fluorescence/ atomic force microscopy (AFM) (WITec Alpha300R, Germany) coupled with an argon ion laser (488 nm) and an Andor Peltier cooled (-66 °C) CCD detector was used for sample patterning and luminescence measurements. An objective of 100 X, with N.A. which was used to focus the 488 nm Ar ion laser and was used to perform both the laser lithography and imaging. The laser power was measured out-of-focus of the objective by a Thorlabs PM100 Optical Power Meter (Thorlabs, Karlsfeld Germany) equipped with a Thorlabs S130A silicon (power range of 5 nW - 5 mW and wavelength range of 400 nm - 1100 nm). Photolithography

was carried out with a laser power of $\sim 120 \mu\text{W}$. This was then followed by fluorescence imaging by the same objective with a much lower laser power of $\sim 20 \mu\text{W}$, reduced to minimize further photochemical changes to the quantum dots during analysis.

4.3 Step by Step Surface Wetting for Cleaner CdSe QDs Nanoring Arrays

Figure 4.1 shows AFM images of CdSe nanoring arrays using particle lithography as described in Figure 3.1, replacing the Au NPs solution with CdSe QDs solution. From Figure 4.1 (A) we can see from the topography image demonstrating that there are visible lines that connect the rings together. From the photoluminescence image on Figure 4.2, it can be seen that those connecting lines are composed of CdSe QDs. From these data, we propose that the formation of these lines was caused by the nonspecific binding of CdSe QDs upon the drying process. The self-assembly of the QDs was driven by the capillary force at the front of the drying meniscus under the microsphere. Since the capillary force is weak, QDs were often left behind the meniscus, resulting in their non-specific binding on the substrate surface.

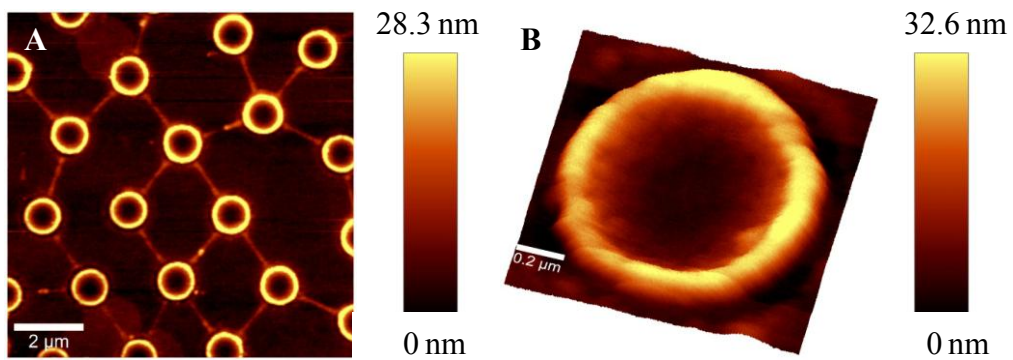


Figure 4. 1 AFM images of CdSe QDs ring on a PVP modified glass substrate.

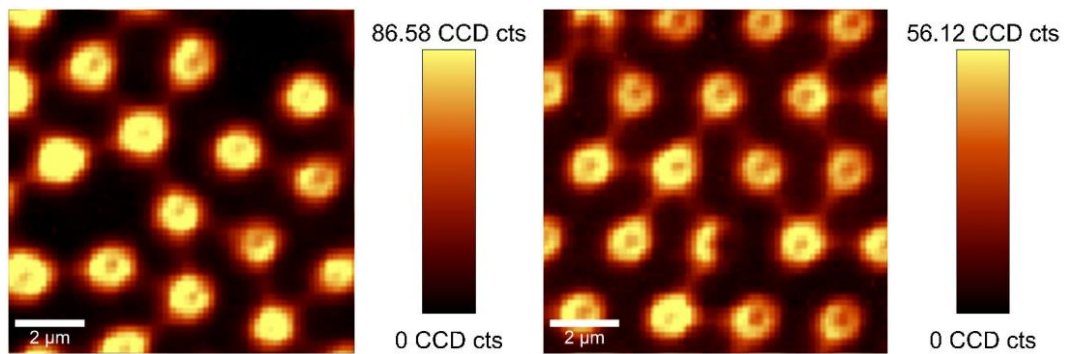


Figure 4. 2 Photoluminescence images of CdSe nanoring arrays on a PVP modified glass substrate.

To overcome the non-specific binding issue of the CdSe QDs, a modification of the particle lithography method was implemented. To eliminate the CdSe QDs that were left behind during the drying process, capillary force was reintroduced into the system. Directly introducing water into the dried system detached the PS MS from the substrate and washed away both the PS MS and the fabricated nanorings structure, therefore disrupting the formation of the nanoring arrays. The reintroduction of the capillary force into the system therefore was performed by cooling down the substrate to allow for the condensation of a thin layer of water on the substrate. This thin layer of water did not affect the hexagonal pattern of the PS MS and the QDs nanorings. As depicted in Figure 4.3 (1,2) after dropcasting the PS MS and CdSe QDs mixture onto the substrate the sample was set to dry for a couple of hours. (3) Capillary force was then reintroduced by cooling down the substrate by placing the system in a water bath for 15 seconds. The system was then allowed to dry for another hour. (3,2) The condensation process was then repeated five times to ensure optimal removal of the nonspecific binding CdSe QDs. Following the last condensation step, the mixture was set to dry overnight and followed by (4) removal of the PS MS by scotch tape (5) exposing the CdSe QDs nanorings.

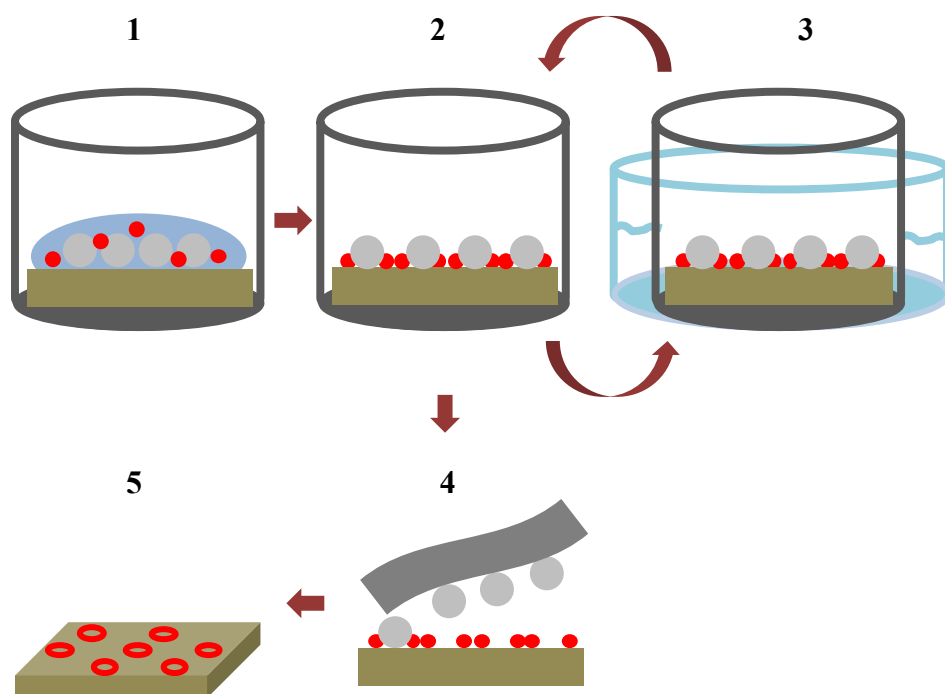


Figure 4. 3 Schematic experimental procedures of the step-by-step surface wetting for the modified particle lithography method.

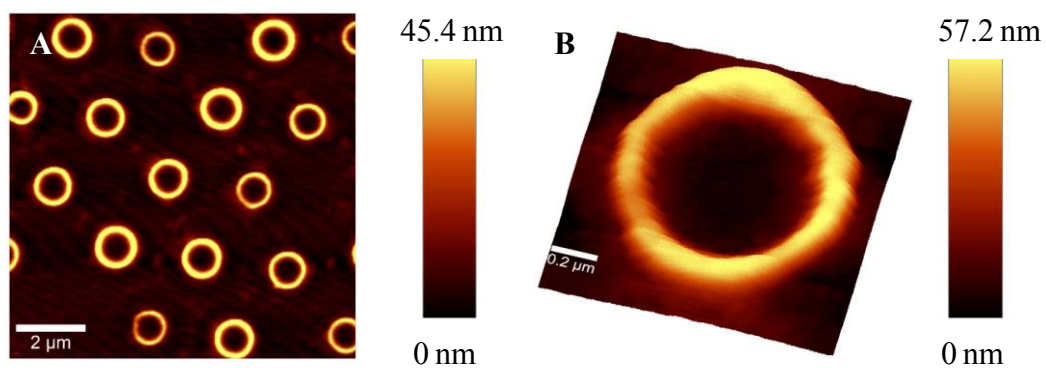


Figure 4. 4 AFM images of CdSe QDs nanorings fabricated using the modified particle lithography method by employing condensation process.

As shown in Figure 4.4 when the condensation process was implemented to the procedure, the CdSe nanorings formed did not exhibit the line features as previously shown on Figure 4.1. The reintroduction of capillary force by condensation into the system was able to remove the QDs that were left behind during the drying process. As shown in figure 4.5 the photoluminescence image (A) of the array fabricated using the condensation method also shows no line figures as confirmed by the photoluminescence spectra in (B) of one of the CdSe rings and its background.

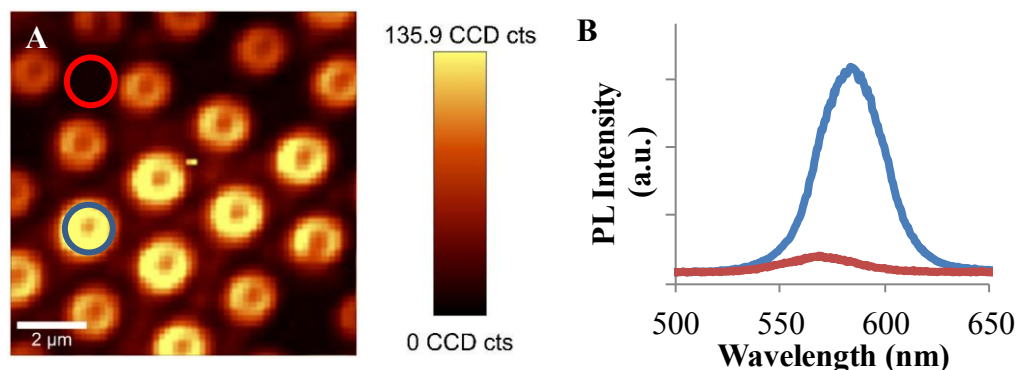


Figure 4. 5 (A) Photoluminescence image of CdSe nanoring arrays and (B) photoluminescence spectra of CdSe nanorings and background signal.

When the condensation process was prolonged to 1 minute, the formation of the nanoring arrays was disrupted. In this case, the water layer introduced during the condensation was significantly larger. It not only removed the non-specific binding CdSe QDs, but also detached the PS MS from the surface. As a result, nanodot arrays were formed instead of nanoring arrays as shown in Figure 4.6.

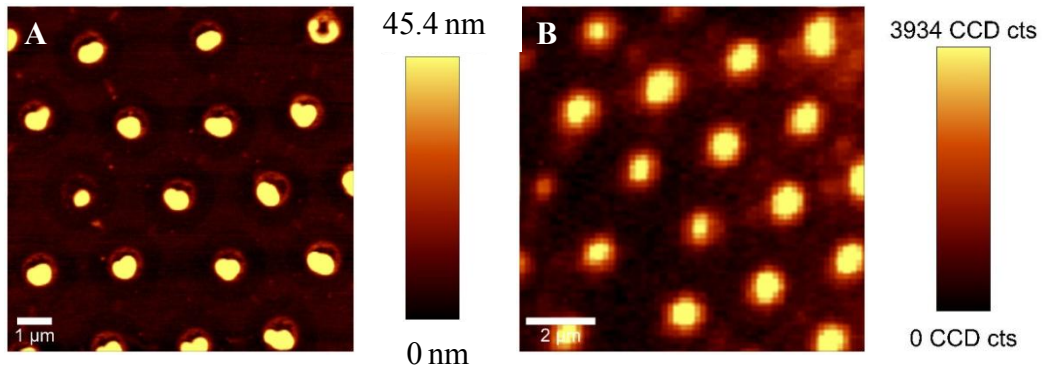


Figure 4. 6 (A) AFM image and (B) photoluminescence image of CdSe nanodots array due to overwetting.

4.4 Employing Laser Photolithography to the CdSe QDs Nanoring Arrays

The photoluminescence of CdSe nanorings can be altered by laser photolithography as described similarly in Chapter II. The blue shift of the photoluminescence can be controlled by changing the laser dwelling time. This allows us to create an array of CdSe nanorings with a range of emission colors as shown in Figure 4.7. Image (A) shows the photoluminescence peak emission of the CdSe nanorings before photolithography with emission at 585 nm. After the photolithography process with increasing laser dwelling time as shown in image (B), the photoluminescence peak emission blue shifted to the lower wavelength region. The longer the laser dwelling time, the more prominent the blue shift became as confirmed in the photoluminescence spectra shown in (C). As seen in Figure 4.7, the photoluminescence of the unaltered rings experienced a minor blue shift from image (A) to (B) due to the minor photobrightening effect caused by rescanning.

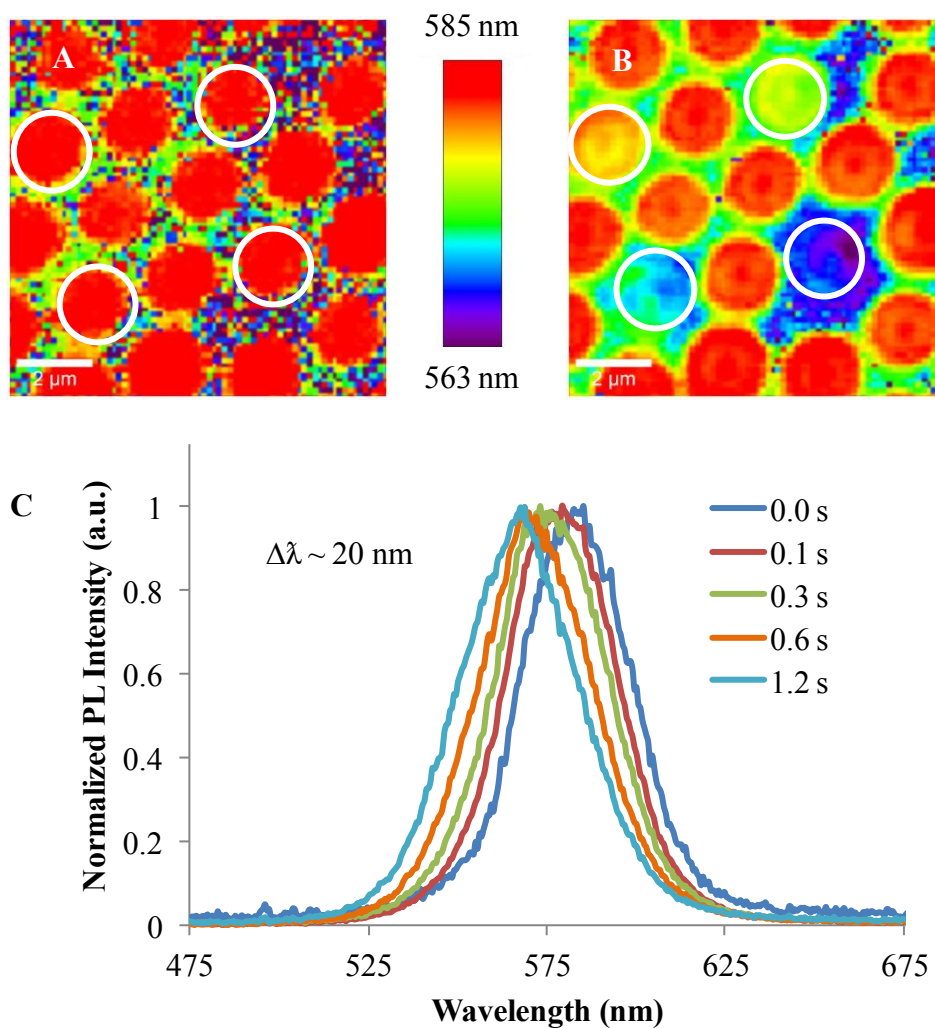


Figure 4. 7 Photoluminescence peak emission of CdSe nanorings area. (A) Before and (B) after laser photolithography with increasing laser dwelling time. (C) Photoluminescence spectra of CdSe rings before photolithography (dark blue at 0.0s) and after photolithography with increasing laser dwelling time (0.1, 0.3, 0.6, 1.2 s integration time) showing the blue shift of the photoluminescence peak.

4.5 Binding of a Thiol Tethered Porphyrin to the CdSe Nanorings

As discussed in Chapter II, the locally photobrightened and photodarkened CdSe QDs created by laser photolithography exhibited a lower density of the capping ligand. Thus, vacancy is created on the surface of the QDs that allowing for the binding of other molecules. In this section a thiol tethered porphyrin molecule, TPy₃PF₄-SC₅SH, which structure is shown in Figure 4.5 was used to probe the binding to the surface of CdSe via the thiol-Cd bond. Photolithography was used to alter the emission of the individual CdSe nanorings as mentioned in the previous section. The sample was then immersed in a solution containing the porphyrin solubilized in dichloromethane (DCM) for 10 minutes, followed by DCM rinsing and drying with nitrogen.

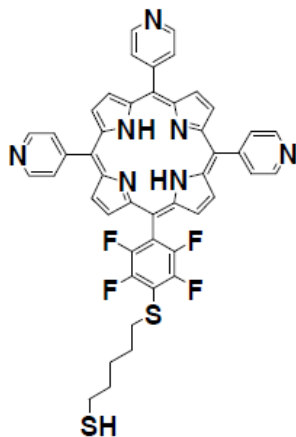


Figure 4. 8 Chemical structure of a free base porphyrin TPy₃PF₄-SC₅SH.

As increasing laser dwelling time was used for photolithography, the photoluminescence peak emission of the altered CdSe nanorings was more blue shifted, as shown in figure 4.9. In comparison to the pristine CdSe rings, the photoluminescence intensity of the altered rings after lithography remained unchanged. However, as the sample is exposed to the porphyrin solution, the photoluminescence intensity of the altered rings decreased as a function of laser integration time (top row). The decrease of the CdSe photoluminescence intensity was accompanied by the increase in the signal of the photoluminescence porphyrin as shown in figure 4.10. When the signal integrated was that of the porphyrin photoluminescence (630 to 730 nm), it can be seen in Figure 4.10 (A) that its intensity increased as a function of laser dwelling time. The decrease in the CdSe photoluminescence intensity and increase of the porphyrin's intensity may give insight about not only the selective binding of the thiol tethered porphyrin to the locally altered CdSe rings, but also the fact that this can be attributed to fluorescence resonance energy transfer (FRET) or charge transfer between the QDs and porphyrin.^{2, 141-143} The porphyrin photoluminescence intensity on the background matrix outside the ring as shown in Figure 4.10 can be attributed to the immobilization of the porphyrin molecule into the porous PVP matrix. The locally altered CdSe QDs nanorings showed an increased propensity to bind new molecules relative to the pristine CdSe nanorings, enabling a facile approach for spatially selective QD surface modification.

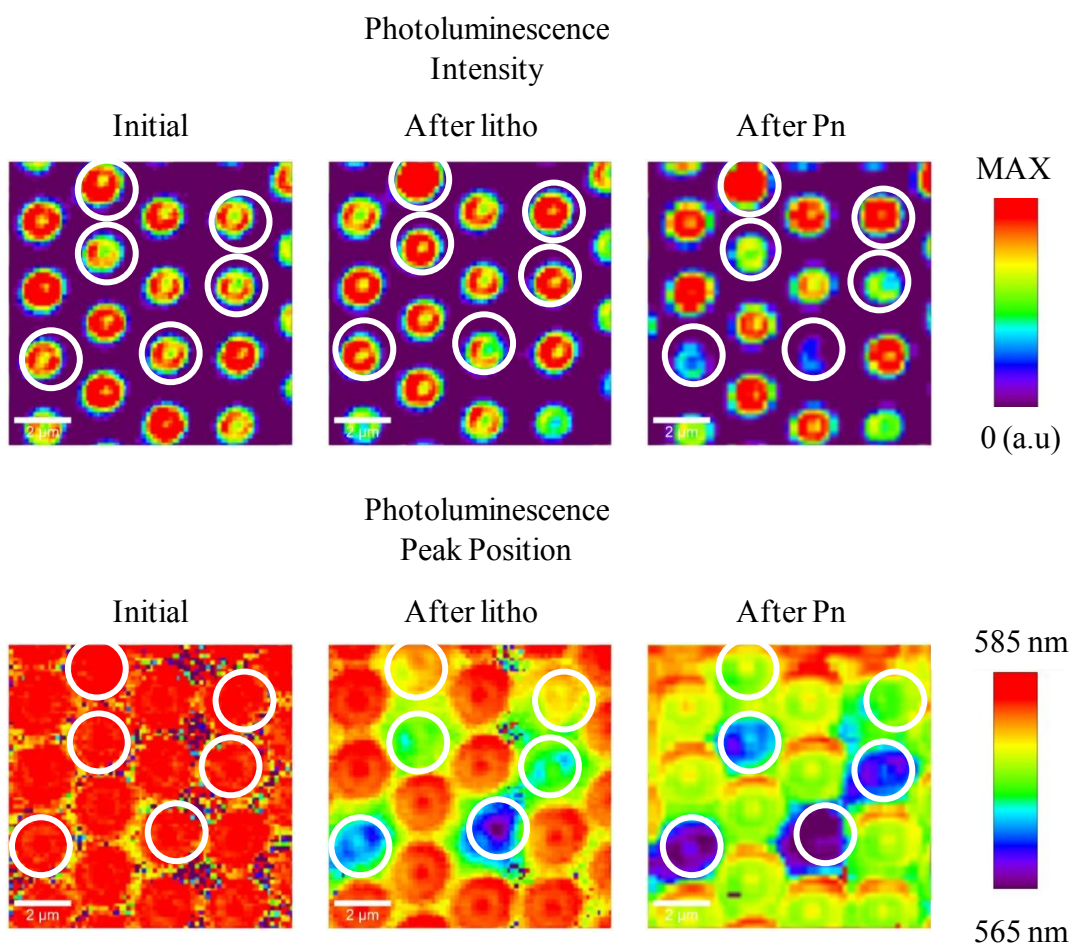


Figure 4. 9 Photoluminescence intensity and peak position images of CdSe nanoring arrays before and after lithography, and after immersion to TPY₃PF₄-SC₅SH. Top row images are photoluminescence images (note that the images are displayed on a different color scale) and bottom row images are photoluminescence peak position.

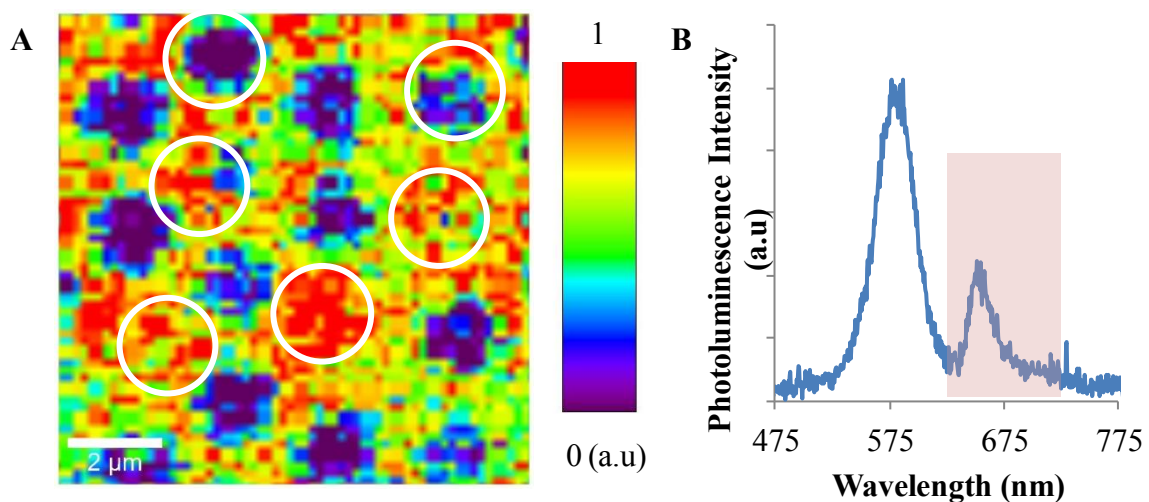


Figure 4. 10 (A) Photoluminescence intensity image of TPy₃PF₄-SC₅SH on CdSe nanoring arrays. (B) Photoluminescence spectra of TPy₃PF₄-SC₅SH and CdSe nanoring arrays. Image (A) was taken by integrating the photoluminescence signal from 630-730 nm.

4.6 Conclusions

The modification of the particle lithography procedure for the fabrication of CdSe nanoring arrays via repetitive condensation was shown to successfully create a clean array of CdSe nanorings with minimal non-specific binding issue. The condensation process reintroduced the capillary force by creating a thin layer of water into the system. That thin layer of water was then able to reduce the non-specific binding CdSe QDs that were left behind during the drying process. A prolonged condensation period can create an “overwetting” case, where a significant amount of water is reintroduced into the system therefore disrupting the formation of the array.

Photopatterning by photolithography was then used to alter the photoluminescence of the fabricated CdSe nanoring arrays. By altering the laser dwelling time, the extent of the photoluminescence blue shift can be controlled. This allowed for the modification of each CdSe nanoring structure to create an array that exhibited different colors of emission. As previously discussed in Chapter II, these locally altered CdSe QDs had a lower capping ligand density as compared to the pristine CdSe QDs. The vacancies created by desorption of the oxidized capping ligand allowed for selective binding of a molecule. In this case, we have shown that a pentathiol tethered porphyrin has a higher binding selectivity to the locally modified CdSe nanorings as compared to those of pristine CdSe nanorings.

CHAPTER V

SUMMARY AND OUTLOOK

5.1 Summary

In this dissertation, the development of CdSe semiconductor QDs and Au NPs as building blocks for nanomaterials based devices was demonstrated. The use of unconventional and inexpensive methods to integrate these nanomaterials on a solid support was explored. The immobilization of these nanomaterials was designed for the study of their fundamental chemical and physical processes as well as their applications.

We began in Chapter II, with the investigation of CdSe QDs for the development of a highly sensitive Ag^+ detection, by exploring the cation exchange reactions between Ag^+ and Cd^{2+} . The water-soluble CdSe QDs were immobilized by electrostatic interactions between the negatively charged 11-mercaptopundecanoic acid (11-MUA) capping ligand and the positively charged substrate modified with polyelectrolytes, PDDA. It was found that the CdSe QDs that were lithographically altered by native ligand removal or surface oxidation, exhibited a different quenching efficiency compared to the pristine QDs, when reacted with an ethanolic solution containing Ag^+ . The locally photobrightened CdSe QDs were found to be quenched more efficiently by the Ag^+ . As confirmed by XPS measurements, the quenching of the photoluminescence was due to the cation exchange between Cd^{2+} and Ag^+ . As previously shown, the locally photobrightened CdSe QDs exhibited a lower ligand density due to the removal of the

oxidized native 11-MUA ligand by exposure to a laser. Therefore it was not surprising that the cation exchange efficiency for these QDs was higher than for the pristine QDs. Desorption of the oxidized 11-MUA ligand resulted in vacancies on the CdSe surface, providing a greater accessibility of the Ag^+ to react with Cd^{2+} . We have also found that the locally photodarkened CdSe QDs exhibited a less efficient cation exchange reactions compared to the pristine QDs, because of the formation of the Se_2O_3 layer on the surface of the QDs, inhibiting the cation exchange process.

Other promising nanomaterials such as Au NPs were examined. They provide an attractive alternative to toxic QDs for chemical sensing, as they are nominally benign. Chapter III focused on to the effort of fabricating Au NP patterned arrays by unconventional lithographic methods. First, the fabrication of Au nanostructure arrays was examined using particle lithography. Here we systematically examined the role of environmental conditions on the fabrication process. It was found that the relative humidity played a crucial role in the formation of these structures. It was shown how the combination of relative humidity and the relative Au NPs concentration to the PS microspheres could be used to alter the morphology of the nanostructured arrays. Uniform nanoring structures could be assembled at 45% RH by using concentrations of 40×10^{11} Au NPs/mL, while the lower Au NPs concentrations of 7×10^{11} Au NPs/mL nanoring arrays would form at a lower RH of 30%. For example, when the RH was increased to 65%, and the Au NP concentrations were used, we observed that the morphology of the nanostructures was altered from nanorings into nanodonuts. The higher RH value combined with the lower Au NPs resulted in higher water content of the

system, which led to a slower evaporation process of the capillary bridge and thus separation of the PS microspheres from the substrate. An alternate method of nanoparticle patterning by microcontact printing with a PDMS stamp and PS mask to direct assembly via APTES as a molecular linker was also successfully implemented to create patterned arrays of Au NPs. Au NPs were selectively immobilized on the area unprotected by the PS mask. This method was shown to be a simple yet robust technique to create pattern array of Au NPs.

Using particle lithography to pattern nanostructured arrays, it was found to be quite versatile for the fabrication of nanomaterials with similar surface affinities. In Chapter IV, particle lithography was used to fabricate uniform nanoring arrays composed of CdSe QDs. To reduce the non-specific binding of CdSe QDs, capillary forces were reintroduced into the system by multiple cycles of condensation. Combining this approach with directed photopatterning (described in Chapter II), the emission of CdSe nanoring could be individually tuned. This provides a facile method to fabricate CdSe nanostructured arrays with specific optical and chemical characteristics, on the same platform. It also has an advantage over the directed assembly of different QDs with different sizes onto the same substrate that can be relatively more complicated and noneconomical. This post-synthetic photochemical modification therefore could be foreseen for the development of some QD based devices, such as: QD based light emitting diodes (LED), where each emitted color can be represented by originally the same QDs, tuned individually by photopatterning.

5.2 Outlook

The Au nanostructure arrays fabricated by particle lithography as described in Chapter III are great building blocks for plasmonic based devices. Therefore there are great deals of effort in trying to understand not just the fabrication and integration of these nanostructured arrays, but also the fundamental details on their optical and electronic properties. Also found in the literature, the LSPR of the Au nanostructure arrays was sensitive to the array's dimensions and morphologies.¹²⁴⁻¹²⁶ Now that we have successfully fabricated the versatile nanostructure arrays, a closer look at their LSPR will be needed. Some work in the past conducted by Link and co-workers on the LSPR of ring structures composed of Au NPs, have shown that small inter-particle distances in nanoparticle assemblies behaved similarly to continuous plasmonic structures because of near-field plasmonic coupling.⁶⁹ Because of the small inter-particle distance in the previously shown nanoring arrays, a strong near-field coupling is therefore expected, hence their LSPR would exhibit those of continuous plasmonic structures.

Aizpura and co-workers have also shown both experimental and simulation study on the LSPR of Au nanorings using the boundary element method (BEM), previously described in Chapter III. They found that as compared to solid gold particles of similar size, nanorings exhibited a redshifted localized surface plasmon that can be tuned over an extended wavelength range by varying the ratio of the ring thickness to its radius due to the coupling between the inner and outer wall of the ring structure. The electric field associated with these plasmons exhibited uniform enhancement and polarization in the

ring cavity, with a maximum enhancement factor, $|E|/|E_{inc}|$, of ~ 50 at its maximum at the upper and lower ends of the ring.¹²⁴ The unique electrical and optical properties that Au nanorings possess make them suitable for applications in sensing and surface enhanced Raman spectroscopy (SERS) and surface enhanced infra-red absorption (SEIRA). The large field enhancement inside the ring cavity as well as the upper and lower ends of the ring, will translate into a greater enhancement in Raman signal and/or photoluminescence signal of a fluorophore. Also found, that the enhancement of the dipole was greater at a junction of nanoparticles dimers or trimers (hot spots) due to near-field enhancement.¹⁴⁴ The local field enhancement was also observed on the split ring structure studied by Cooper and co-workers.¹⁴⁵ In their work, the near-field coupling facilitated by the junctions in the split ring structure was able to show a maximum field enhancement of 132. This local field enhancement will allow for maximum SERS and SEIRA enhancements.

Scanning probe lithography (SPL) by AFM can be implemented to alter the morphology of the pre-fabricated nanostructures, to mimic the metal particle junction's hot spots. With this, the modification of the Au nanoring's morphology can be accomplished post-fabrication by employing AFM nanoshaving. As shown in Figure 5.1, a sharp and durable contact mode made of diamond-like-carbon (DLC) was used to alter the morphology of a single Au nanoring. The same DLC tip was used to perform the scanning and nanoshaving experiment. All AFM imaging and SPL for this experiment was performed by using contact mode in air. A much lower set point of 0.1 V was used to image the nanostructures as compared to the 5 V used to perform nanoshaving

lithography, to avoid damage of the nanostructures. The split ring structure shown in Figure 5.1 resembles one shown by Cooper and co-workers¹⁴⁵ fabricated via e-beam lithography. Again, the particle lithography method combined with AFM nanoshaving serve as a simpler and more cost effective alternative for the fabrication and manipulation of nanostructures, avoiding the use of e-beam lithography.

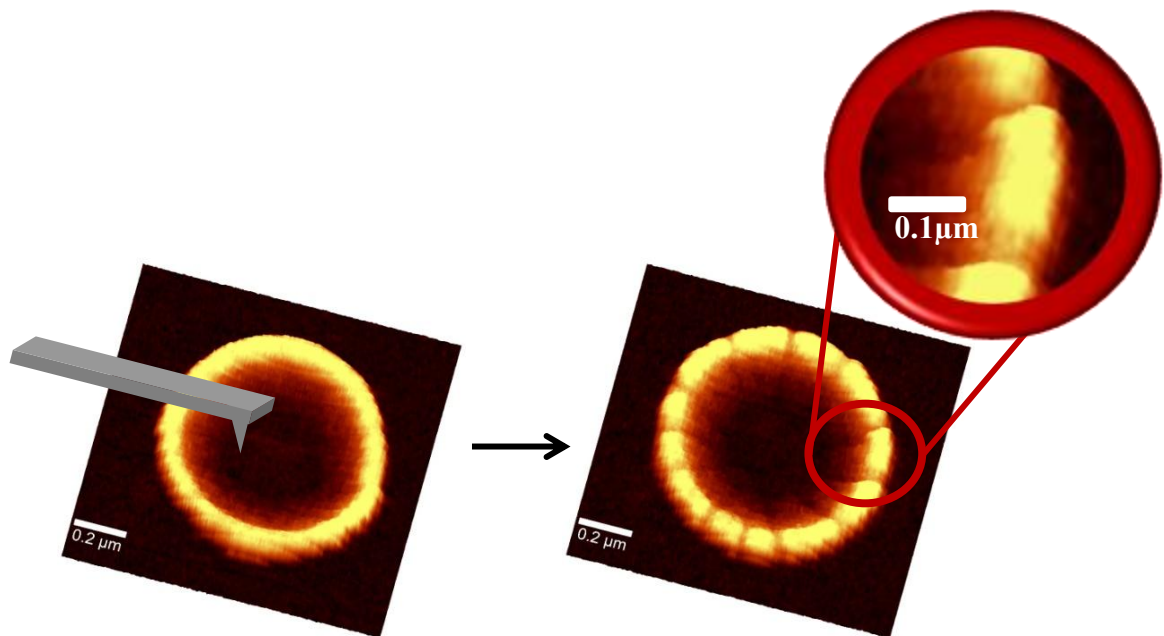


Figure 5. 1 AFM contact mode images of Au nanoring structure before and after AFM nanoshaving.

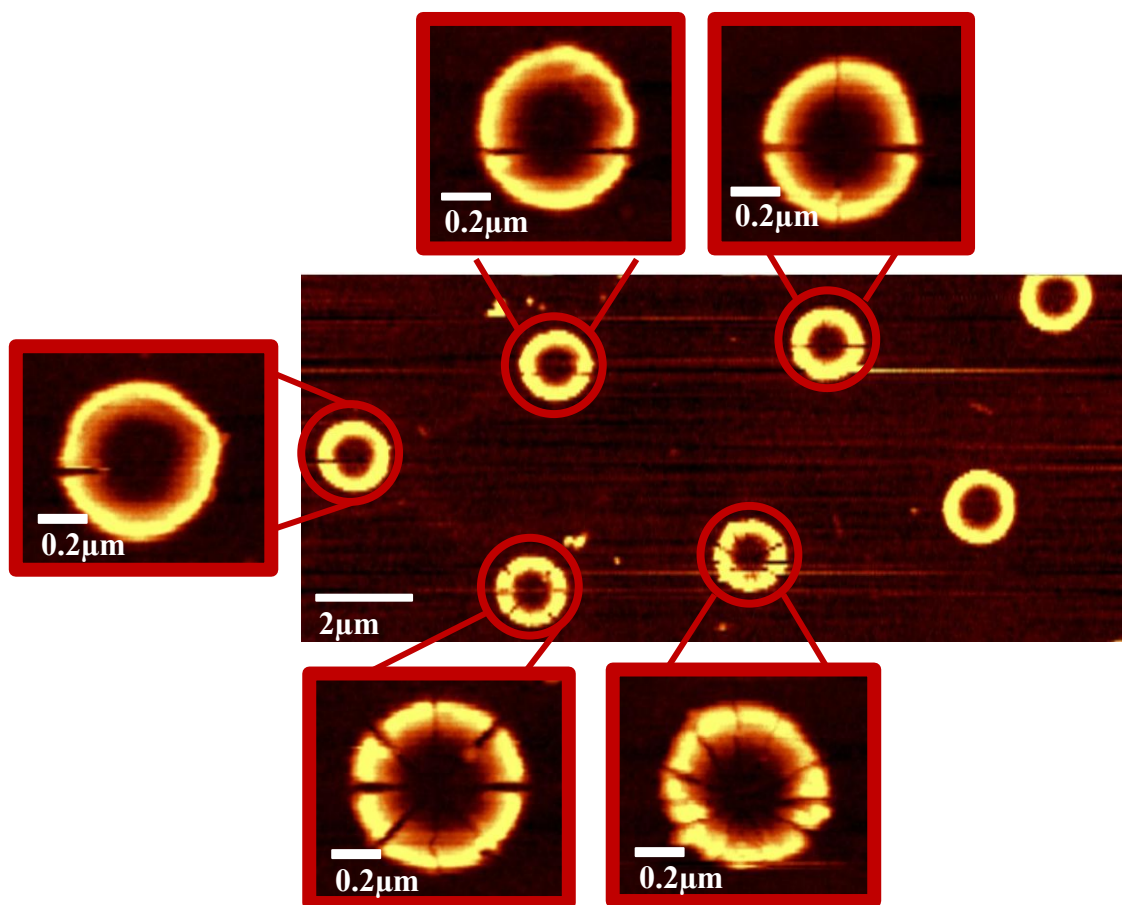


Figure 5. 2 Au nanostructure arrays after AFM nanoshaving, showing different morphologies of the structures as the individual ring is partitioned into an increasing number of segments.

By tuning the parameters of the nanoshaving, an array consisting of Au nanorings with different morphologies previously modified by AFM nanoshaving, was created, as shown in Figure 5.2. The fabricated Au nanostructure arrays can serve as a platform to study the effects of morphology upon their LSPR near-field coupling. The LSPR of each individual split-nanoring can be observed and compared to those of

unmodified continuous ring structure within a single platform. The study of the LSPR of asymmetric metallic nanostructures has also been exploited for the study of the plasmonic dark mode, which can only be observed when the symmetry of the structure is broken.^{41, 146-149} The previously described AFM nanoshaving method can be easily tuned to create an asymmetric nanostructure, similar to those fabricated by Lahiri and co-workers using e-beam lithography.¹⁴⁸ With this, the fabricated Au nanostructure array serves as an innovative platform for the fundamental LSPR study of Au nanostructures, with promising potential for sensing, surface enhanced Raman spectroscopy (SERS), and surface enhanced infra-red absorption (SEIRA).

REFERENCES

1. Kulakovich, O.; Strekal, N.; Yaroshevich, A.; Maskevich, S.; Gaponenko, S.; Nabiev, I.; Woggon, U.; Artemyev, M. Enhanced luminescence of CdSe quantum dots on gold colloids. *Nano Lett* 2002, 2, 1449-1452.
2. Chan, Y. H.; Chen, J. X.; Wark, S. E.; Skiles, S. L.; Son, D. H.; Batteas, J. D. Using patterned arrays of metal nanoparticles to probe plasmon enhanced Luminescence of CdSe Quantum Dots. *Acs Nano* 2009, 3, 1735-1744.
3. Zheng, J. W.; Zhu, Z. H.; Chen, H. F.; Liu, Z. F. Nanopatterned assembling of colloidal gold nanoparticles on silicon. *Langmuir* 2000, 16, 4409-4412.
4. Willets, K. A.; Van Duyne, R. P. Localized surface plasmon resonance spectroscopy and sensing. *Annu Rev Phys Chem* 2007, 58, 267-297.
5. Shipway, A. N.; Katz, E.; Willner, I. Nanoparticle arrays on surfaces for electronic, optical, and sensor applications. *Chemphyschem* 2000, 1, 18-52.
6. Thakar, R.; Chen, Y. C.; Snee, P. T. Efficient emission from core/(doped) shell nanoparticles: Applications for chemical sensing. *Nano Lett* 2007, 7, 3429-3432.
7. Kamat, P. V. Quantum dot solar cells: Semiconductor nanocrystals as light harvesters. *J Phys Chem C* 2008, 112, 18737-18753.
8. Hyun, B. R.; Zhong, Y. W.; Bartnik, A. C.; Sun, L. F.; Abruna, H. D.; Wise, F. W.; Goodreau, J. D.; Matthews, J. R.; Leslie, T. M.; Borrelli, N. F. Electron injection from colloidal PbS quantum dots into titanium dioxide nanoparticles. *Acs Nano* 2008, 2, 2206-2212.

9. Kairdolf, B. A.; Smith, A. M.; Stokes, T. H.; Wang, M. D.; Young, A. N.; Nie, S. Semiconductor quantum dots for bioimaging and biodiagnostic applications. *Annu Rev Anal Chem (Palo Alto Calif)* 2013, 6, 143-62.
10. Zang, L.; Che, Y. K.; Moore, J. S. One-dimensional self-assembly of planar pi-conjugated molecules: Adaptable building blocks for organic nanodevices. *Accounts Chem Res* 2008, 41, 1596-1608.
11. Gong, X. C.; Milic, T.; Xu, C.; Batteas, J. D.; Drain, C. M. Preparation and characterization of porphyrin nanoparticles. *J Am Chem Soc* 2002, 124, 14290-14291.
12. O'Reilly, R. K.; Hawker, C. J.; Wooley, K. L. Cross-linked block copolymer micelles: Functional nanostructures of great potential and versatility. *Chem Soc Rev* 2006, 35, 1068-1083.
13. Friend, R. H.; Gymer, R. W.; Holmes, A. B.; Burroughes, J. H.; Marks, R. N.; Taliani, C.; Bradley, D. D. C.; Dos Santos, D. A.; Bredas, J. L.; Logdlund, M.; Salaneck, W. R. Electroluminescence in conjugated polymers. *Nature* 1999, 397, 121-128.
14. Yang, W. R.; Ratinac, K. R.; Ringer, S. P.; Thordarson, P.; Gooding, J. J.; Braet, F. Carbon nanomaterials in biosensors: should you use nanotubes or graphene? *Angew Chem Int Edit* 2010, 49, 2114-2138.
15. Wang, X. R.; Ouyang, Y. J.; Li, X. L.; Wang, H. L.; Guo, J.; Dai, H. J. Room-temperature all-semiconducting sub-10-nm graphene nanoribbon field-effect transistors. *Phys Rev Lett* 2008, 100.

16. Anikeeva, P. O.; Halpert, J. E.; Bawendi, M. G.; Bulovic, V. Quantum dot light-emitting devices with electroluminescence tunable over the entire visible spectrum. *Nano Lett* 2009, 9, 2532-2536.
17. Chen, X.; Mao, S. S. Titanium dioxide nanomaterials: Synthesis, properties, modifications, and applications. *Chem Rev* 2007, 107, 2891-2959.
18. Kamat, P. V.; Tvrdy, K.; Baker, D. R.; Radich, J. G. Beyond photovoltaics: semiconductor nanoarchitectures for liquid-junction solar cells. *Chem Rev* 2010, 110, 6664-6688.
19. Huang, X. H.; Jain, P. K.; El-Sayed, I. H.; El-Sayed, M. A. Plasmonic photothermal therapy (phtt) using gold nanoparticles. *Laser Med Sci* 2008, 23, 217-228.
20. Medintz, I. L.; Clapp, A. R.; Mattoussi, H.; Goldman, E. R.; Fisher, B.; Mauro, J. M. Self-assembled nanoscale biosensors based on quantum dot FRET donors. *Nat Mater* 2003, 2, 630-638.
21. Gates, B. D.; Xu, Q. B.; Stewart, M.; Ryan, D.; Willson, C. G.; Whitesides, G. M. New approaches to nanofabrication: Molding, printing, and other techniques. *Chem Rev* 2005, 105, 1171-1196.
22. Manfrinato, V. R.; Zhang, L. H.; Su, D.; Duan, H. G.; Hobbs, R. G.; Stach, E. A.; Berggren, K. K. Resolution limits of electron-beam lithography toward the atomic scale. *Nano Lett* 2013, 13, 1555-1558.
23. Gates, B. D.; Xu, Q. B.; Love, J. C.; Wolfe, D. B.; Whitesides, G. M. Unconventional nanofabrication. *Annu Rev Mater Res* 2004, 34, 339-372.

24. Kotov, N. A.; Dekany, I.; Fendler, J. H. Layer-by-layer self-assembly of polyelectrolyte-semiconductor nanoparticle composite films. *J Phys Chem-US* 1995, 99, 13065-13069.
25. Carosio, F.; Laufer, G.; Alongi, J.; Camino, G.; Grunlan, J. C. Layer-by-layer assembly of silica-based flame retardant thin film on PET fabric. *Polym Degrad Stabil* 2011, 96, 745-750.
26. Shen, Y. J.; Lee, Y. L. Assembly of CdS quantum dots onto mesoscopic TiO₂ films for quantum dot-sensitized solar cell applications. *Nanotechnology* 2008, 19.
27. Kongkanand, A.; Tvrdy, K.; Takechi, K.; Kuno, M.; Kamat, P. V. Quantum dot solar cells. Tuning photoresponse through size and shape control of CdSe-TiO₂ architecture. *J Am Chem Soc* 2008, 130, 4007-4015.
28. Guijarro, N.; Lana-Villarreal, T.; Mora-Sero, I.; Bisquert, J.; Gomez, R. CdSe quantum dot-sensitized TiO₂ electrodes: effect of quantum dot coverage and mode of attachment. *J Phys Chem C* 2009, 113, 4208-4214.
29. Ballarin, B.; Cassani, M. C.; Scavetta, E.; Tonelli, D. Self-assembled gold nanoparticles modified ITO electrodes: The monolayer binder molecule effect. *Electrochim Acta* 2008, 53, 8034-8044.
30. Tseng, J. Y.; Lin, M. H.; Chau, L. K. Preparation of colloidal gold multilayers with 3-(mercaptopropyl)-trimethoxysilane as a linker molecule. *Colloid Surface A* 2001, 182, 239-245.

31. Ftouni, J.; Penhoat, M.; Girardon, J. S.; Addad, A.; Payen, E.; Rolando, C. Immobilization of gold nanoparticles on fused silica capillary surface for the development of catalytic microreactors. *Chem Eng J* 2013, 227, 103-110.
32. Quist, A. P.; Pavlovic, E.; Oscarsson, S. Recent advances in microcontact printing. *Anal Bioanal Chem* 2005, 381, 591-600.
33. Anker, J. N.; Hall, W. P.; Lyandres, O.; Shah, N. C.; Zhao, J.; Van Duyne, R. P. Biosensing with plasmonic nanosensors. *Nat Mater* 2008, 7, 442-453.
34. Santhanam, V.; Andres, R. P. Microcontact printing of uniform nanoparticle arrays. *Nano Lett* 2004, 4, 41-44.
35. Kraus, T.; Malaquin, L.; Schmid, H.; Riess, W.; Spencer, N. D.; Wolf, H. Nanoparticle printing with single-particle resolution. *Nat Nanotechnol* 2007, 2, 570-576.
36. Jones, R. L.; Harrod, B. L.; Batteas, J. D. Intercalation of 3-Phenyl-1-propanal into OTS SAMs on Silica Nanoasperities to Create Self-Repairing Interfaces for MEMS Lubrication. *Langmuir* 2010, 26, 16355-16361.
37. Xia, D. Y.; Brueck, S. R. J. A facile approach to directed assembly of patterns of nanoparticles using interference lithography and spin coating. *Nano Lett* 2004, 4, 1295-1299.
38. Faustini, M.; Capobianchi, A.; Varvaro, G.; Grosso, D. Highly controlled dip-coating deposition of fct FePt nanoparticles from layered salt precursor into nanostructured thin films: an easy way to tune magnetic and optical properties. *Chem Mater* 2012, 24, 1072-1079.

39. Jung, B. G.; Min, S. H.; Kwon, C. W.; Park, S. H.; Kim, K. B.; Yoon, T. S. Colloidal nanoparticle-layer formation through dip-coating: effect of solvents and substrate withdrawing speed. *J Electrochem Soc* 2009, 156, K86-K90.
40. Lusker, K. L.; Li, J. R.; Garno, J. C. Nanostructures of functionalized gold nanoparticles prepared by particle lithography with organosilanes. *Langmuir* 2011, 27, 13269-13275.
41. Cai, Y. J.; Li, Y.; Nordlander, P.; Cremer, P. S. Fabrication of elliptical nanorings with highly tunable and multiple plasmonic resonances. *Nano Lett* 2012, 12, 4881-4888.
42. Haynes, C. L.; Van Duyne, R. P. Nanosphere lithography: A versatile nanofabrication tool for studies of size-dependent nanoparticle optics. *J Phys Chem B* 2001, 105, 5599-5611.
43. Bruchez, M.; Moronne, M.; Gin, P.; Weiss, S.; Alivisatos, A. P. Semiconductor nanocrystals as fluorescent biological labels. *Science* 1998, 281, 2013-2016.
44. Onclin, S.; Ravoo, B. J.; Reinhoudt, D. N. Engineering silicon oxide surfaces using self-assembled monolayers. *Angew Chem Int Edit* 2005, 44, 6282-6304.
45. Fischer, U. C.; Zingsheim, H. P. Sub-microscopic pattern replication with visible-light. *J Vac Sci Technol* 1981, 19, 881-885.
46. Deckman, H. W.; Dunsmuir, J. H. Natural lithography. *Appl Phys Lett* 1982, 41, 377-379.
47. Alivisatos, A. P. Semiconductor clusters, nanocrystals, and quantum dots. *Science* 1996, 271, 933-937.

48. Vossmeier, T.; Katsikas, L.; Giersig, M.; Popovic, I. G.; Diesner, K.; Chemseddine, A.; Eychmuller, A.; Weller, H. CdS nanoclusters - synthesis, characterization, size-dependent oscillator strength, temperature shift of the excitonic-transition energy, and reversible absorbency shift. *J Phys Chem-US* 1994, 98, 7665-7673.
49. Costa-Fernandez, J. M.; Pereiro, R.; Sanz-Medel, A. The use of luminescent quantum dots for optical sensing. *Trac-Trend Anal Chem* 2006, 25, 207-218.
50. Chan, W. C. W.; Nie, S. M. Quantum dot bioconjugates for ultrasensitive nonisotopic detection. *Science* 1998, 281, 2016-2018.
51. Medintz, I. L.; Uyeda, H. T.; Goldman, E. R.; Mattoussi, H. Quantum dot bioconjugates for imaging, labelling and sensing. *Nat Mater* 2005, 4, 435-446.
52. Robel, I.; Subramanian, V.; Kuno, M.; Kamat, P. V. Quantum dot solar cells. Harvesting light energy with CdSe nanocrystals molecularly linked to mesoscopic TiO₂ films. *J Am Chem Soc* 2006, 128, 2385-2393.
53. Colvin, V. L.; Schlamp, M. C.; Alivisatos, A. P. Light-Emitting-Diodes Made from Cadmium Selenide Nanocrystals and a Semiconducting Polymer. *Nature* 1994, 370, 354-357.
54. Coe, S.; Woo, W. K.; Bawendi, M.; Bulovic, V. Electroluminescence from single monolayers of nanocrystals in molecular organic devices. *Nature* 2002, 420, 800-803.

55. Mattoussi, H.; Radzilowski, L. H.; Dabbousi, B. O.; Thomas, E. L.; Bawendi, M. G.; Rubner, M. F. Electroluminescence from heterostructures of poly(phenylene vinylene) and inorganic CdSe nanocrystals. *J Appl Phys* 1998, 83, 7965-7974.
56. Yang, H. S.; Holloway, P. H. Electroluminescence from hybrid conjugated polymer - CdS : Mn/ZnS core/shell nanocrystals devices. *J Phys Chem B* 2003, 107, 9705-9710.
57. Sun, Q.; Wang, Y. A.; Li, L. S.; Wang, D. Y.; Zhu, T.; Xu, J.; Yang, C. H.; Li, Y. F. Bright, multicoloured light-emitting diodes based on quantum dots. *Nat Photonics* 2007, 1, 717-722.
58. Caruge, J. M.; Halpert, J. E.; Wood, V.; Bulovic, V.; Bawendi, M. G. Colloidal quantum-dot light-emitting diodes with metal-oxide charge transport layers. *Nat Photonics* 2008, 2, 247-250.
59. Cho, K. S.; Lee, E. K.; Joo, W. J.; Jang, E.; Kim, T. H.; Lee, S. J.; Kwon, S. J.; Han, J. Y.; Kim, B. K.; Choi, B. L.; Kim, J. M. High-performance crosslinked colloidal quantum-dot light-emitting diodes. *Nat Photonics* 2009, 3, 341-345.
60. Aldana, J.; Wang, Y. A.; Peng, X. G. Photochemical instability of CdSe nanocrystals coated by hydrophilic thiols. *J Am Chem Soc* 2001, 123, 8844-8850.
61. Brus, L. Noble Metal Nanocrystals: Plasmon Electron Transfer Photochemistry and Single-Molecule Raman Spectroscopy. *Accounts Chem Res* 2008, 41, 1742-1749.
62. Novotny, L. I. H., B. *Principles of Nano-Optics*. Cambridge University Pres: Cambridge, UK, 2006.

63. Hohenester, U.; Trugler, A. MNPBEM - A Matlab toolbox for the simulation of plasmonic nanoparticles. *Comput Phys Commun* 2012, 183, 370-381.
64. McLellan, J. M.; Li, Z. Y.; Siekkinen, A. R.; Xia, Y. N. The SERS activity of a supported ag nanocube strongly depends on its orientation relative to laser polarization. *Nano Lett* 2007, 7, 1013-1017.
65. Campion, A.; Kambhampati, P. Surface-enhanced Raman scattering. *Chem Soc Rev* 1998, 27, 241-250.
66. Kneipp, K.; Kneipp, H.; I, I.; Dasari, R. R.; Feld, M. S. Ultrasensitive chemical analysis by Raman spectroscopy. *Chem Rev* 1999, 99, 2957-+.
67. Chan, Y. H.; Chen, J. X.; Liu, Q. S.; Wark, S. E.; Son, D. H.; Batteas, J. D. Ultrasensitive copper(II) detection using plasmon-enhanced and photo-brightened luminescence of CdSe quantum dots. *Anal Chem* 2010, 82, 3671-3678.
68. Turkevich, J.; Stevenson, P. C.; Hillier, J. A study of the nucleation and growth processes in the synthesis of colloidal gold. *Discuss Faraday Soc* 1951, 55-&.
69. Chang, W. S.; Slaughter, L. S.; Khanal, B. P.; Manna, P.; Zubarev, E. R.; Link, S. One-dimensional coupling of gold nanoparticle plasmons in self-assembled ring superstructures. *Nano Lett* 2009, 9, 1152-1157.
70. Prodan, E.; Radloff, C.; Halas, N. J.; Nordlander, P. A hybridization model for the plasmon response of complex nanostructures. *Science* 2003, 302, 419-422.
71. Binnig, G.; Quate, C. F.; Gerber, C. Atomic Force Microscope. *Phys Rev Lett* 1986, 56, 930-933.

72. Binning, G.; Rohrer, H.; Gerber, C.; Weibel, E. Surface studies by scanning tunneling microscopy. *Phys Rev Lett* 1982, 49, 57-61.
73. Sidles, J. A.; Garbini, J. L.; Bruland, K. J.; Rugar, D.; Zuger, O.; Hoen, S.; Yannoni, C. S. Magnetic-resonance force microscopy. *Rev Mod Phys* 1995, 67, 249-265.
74. Rugar, D.; Mamin, H. J.; Guethner, P.; Lambert, S. E.; Stern, J. E.; Mcfadyen, I.; Yogi, T. Magnetic force microscopy - general-principles and application to longitudinal recording media. *J Appl Phys* 1990, 68, 1169-1183.
75. Krauss, T. D.; Brus, L. E. Charge, polarizability, and photoionization of single semiconductor nanocrystals. *Phys Rev Lett* 1999, 83, 4840-4843.
76. Katzenmeyer, A. M.; Aksyuk, V.; Centrone, A. Nanoscale infrared spectroscopy: Improving the spectral range of the photothermal induced resonance technique. *Anal Chem* 2013, 85, 1972-1979.
77. Gu, J. H.; Yam, C. M.; Li, S.; Cai, C. Z. Nanometric protein arrays on protein-resistant monolayers on silicon surfaces. *J Am Chem Soc* 2004, 126, 8098-8099.
78. Piner, R. D.; Zhu, J.; Xu, F.; Hong, S. H.; Mirkin, C. A. "Dip-pen" nanolithography. *Science* 1999, 283, 661-663.
79. Ngunjiri, J.; Garino, J. C. AFM-based lithography for nanoscale protein assays. *Anal Chem* 2008, 80, 1361-1369.
80. Xu, S.; Laibinis, P. E.; Liu, G. Y. Accelerating the kinetics of thiol self-assembly on gold - A spatial confinement effect. *J Am Chem Soc* 1998, 120, 9356-9361.

81. Xiao, X. D.; Liu, G. Y.; Charych, D. H.; Salmeron, M. Preparation, Structure, and Mechanical Stability of Alkylsilane Monolayers on Mica. *Langmuir* 1995, 11, 1600-1604.
82. Shi, J. J.; Chen, J. X.; Cremer, P. S. Sub-100 nm Patterning of supported bilayers by nanoshaving lithography. *J Am Chem Soc* 2008, 130, 2718-+.
83. Michalet, X.; Pinaud, F. F.; Bentolila, L. A.; Tsay, J. M.; Doose, S.; Li, J. J.; Sundaresan, G.; Wu, A. M.; Gambhir, S. S.; Weiss, S. Quantum dots for live cells, in vivo imaging, and diagnostics. *Science* 2005, 307, 538-544.
84. Park, J. H.; Gu, L.; von Maltzahn, G.; Ruoslahti, E.; Bhatia, S. N.; Sailor, M. J. Biodegradable luminescent porous silicon nanoparticles for in vivo applications. *Nat Mater* 2009, 8, 331-336.
85. Zhang, C. Y.; Yeh, H. C.; Kuroki, M. T.; Wang, T. H. Single-quantum-dot-based DNA nanosensor. *Nat Mater* 2005, 4, 826-831.
86. Medintz, I. L.; Clapp, A. R.; Brunel, F. M.; Tiefenbrunn, T.; Uyeda, H. T.; Chang, E. L.; Deschamps, J. R.; Dawson, P. E.; Mattoussi, H. Proteolytic activity monitored by fluorescence resonance energy transfer through quantum-dot-peptide conjugates. *Nat Mater* 2006, 5, 581-589.
87. Lundstrom, T.; Schoenfeld, W.; Lee, H.; Petroff, P. M. Exciton storage in semiconductor self-assembled quantum dots. *Science* 1999, 286, 2312-2314.
88. Craig, N. J.; Taylor, J. M.; Lester, E. A.; Marcus, C. M.; Hanson, M. P.; Gossard, A. C. Tunable nonlocal spin control in a coupled-quantum dot system. *Science* 2004, 304, 565-567.

89. Latta, C.; Hogele, A.; Zhao, Y.; Vamivakas, A. N.; Maletinsky, P.; Kroner, M.; Dreiser, J.; Carusotto, I.; Badolato, A.; Schuh, D.; Wegscheider, W.; Atature, M.; Imamoglu, A. Confluence of resonant laser excitation and bidirectional quantum-dot nuclear-spin polarization. *Nat Phys* 2009, 5, 758-763.
90. Beaulac, R.; Schneider, L.; Archer, P. I.; Bacher, G.; Gamelin, D. R. Light-Induced Spontaneous Magnetization in Doped Colloidal Quantum Dots. *Science* 2009, 325, 973-976.
91. Wiersig, J.; Gies, C.; Jahnke, F.; Assmann, M.; Berstermann, T.; Bayer, M.; Kistner, C.; Reitzenstein, S.; Schneider, C.; Hofling, S.; Forchel, A.; Kruse, C.; Kalden, J.; Hommel, D. Direct observation of correlations between individual photon emission events of a microcavity laser. *Nature* 2009, 460, 245-U108.
92. Sukhovatkin, V.; Hinds, S.; Brzozowski, L.; Sargent, E. H. Colloidal Quantum-Dot Photodetectors Exploiting Multiexciton Generation. *Science* 2009, 324, 1542-1544.
93. Dabbousi, B. O.; RodriguezViejo, J.; Mikulec, F. V.; Heine, J. R.; Mattoussi, H.; Ober, R.; Jensen, K. F.; Bawendi, M. G. (CdSe)ZnS core-shell quantum dots: Synthesis and characterization of a size series of highly luminescent nanocrystallites. *J Phys Chem B* 1997, 101, 9463-9475.
94. Leatherdale, C. A.; Woo, W. K.; Mikulec, F. V.; Bawendi, M. G. On the absorption cross section of CdSe nanocrystal quantum dots. *J Phys Chem B* 2002, 106, 7619-7622.

95. Murphy, C. J. Optical sensing with quantum dots. *Anal Chem* 2002, 74, 520a-526a.
96. Tagliazucchi, M.; Tice, D. B.; Sweeney, C. M.; Morris-Cohen, A. J.; Weiss, E. A. Ligand-controlled rates of photoinduced electron transfer in hybrid CdSe nanocrystal/poly(viologen) Films. *Acs Nano* 2011, 5, 9907-9917.
97. Morris-Cohen, A. J.; Vasilenko, V.; Amin, V. A.; Reuter, M. G.; Weiss, E. A. model for adsorption of ligands to colloidal quantum dots with concentration-dependent surface structure. *Acs Nano* 2012, 6, 557-565.
98. Robinson, R. D.; Sadtler, B.; Demchenko, D. O.; Erdonmez, C. K.; Wang, L. W.; Alivisatos, A. P. Spontaneous superlattice formation in nanorods through partial cation exchange. *Science* 2007, 317, 355-358.
99. Burgess, J. *Metal Ions in Solutions*. Ellis Horwood: Sussex, UK, 1978.
100. *Pure Substances, Part 1: Elements and Compounds from AgBr to Ba₃N₂, vol. 19 of Landolt-Bo`rnstein Group IV Physical Chemistry*. Springer-Verlag, Heidelberg, Germany, 1999.
101. Moon, G. D.; Ko, S.; Xia, Y. N.; Jeong, U. Chemical transformations in ultrathin chalcogenide nanowires. *Acs Nano* 2010, 4, 2307-2319.
102. Hankare, P. P.; Bhuse, V. M.; Garadkar, K. M.; Delekar, S. D.; Mulla, I. S. Low temperature route to grow polycrystalline cadmium selenide and mercury selenide thin films. *Mater Chem Phys* 2003, 82, 711-717.

103. Jeong, U.; Kim, J. U.; Xia, Y. N. Monodispersed spherical colloids of Se@CdSe: Synthesis and use as building blocks in fabricating photonic crystals. *Nano Lett* 2005, 5, 937-942.
104. Kang, M. S.; Sahu, A.; Frisbie, C. D.; Norris, D. J. Influence of silver doping on electron transport in thin films of PbSe nanocrystals. *Adv Mater* 2012.
105. Dloczik, L.; Konenkamp, R. Nanostructure transfer in semiconductors by ion exchange. *Nano Lett* 2003, 3, 651-653.
106. Liang, J. G.; Ai, X. P.; He, Z. K.; Pang, D. W. Functionalized CdSe quantum dots as selective silver ion chemodosimeter. *Analyst* 2004, 129, 619-622.
107. O'Sullivan, C.; Gunning, R. D.; Sanyal, A.; Barrett, C. A.; Geaney, H.; Laffir, F. R.; Ahmed, S.; Ryan, K. M. Spontaneous Room Temperature Elongation of CdS and Ag₂S Nanorods via Oriented Attachment. *J Am Chem Soc* 2009, 131, 12250-12257.
108. Chen, J. X.; Chan, Y. H.; Yang, T. L.; Wark, S. E.; Son, D. H.; Batteas, J. D. Spatially selective optical tuning of quantum dot thin film luminescence. *J Am Chem Soc* 2009, 131, 18204-+.
109. Yang, T. L.; Jung, S. Y.; Mao, H. B.; Cremer, P. S. Fabrication of phospholipid bilayer-coated microchannels for on-chip immunoassays. *Anal Chem* 2001, 73, 165-169.
110. Aldana, J.; Lavelle, N.; Wang, Y. J.; Peng, X. G. Size-dependent dissociation pH of thiolate ligands from cadmium chalcogenide nanocrystals. *J Am Chem Soc* 2005, 127, 2496-2504.

111. Munro, A. M.; Jen-La Plante, I.; Ng, M. S.; Ginger, D. S. Quantitative study of the effects of surface ligand concentration on CdSe nanocrystal photoluminescence. *J Phys Chem C* 2007, 111, 6220-6227.
112. Katari, J. E. B.; Colvin, V. L.; Alivisatos, A. P. X-Ray Photoelectron-spectroscopy of Cdse nanocrystals with applications to studies of the nanocrystal surface. *J Phys Chem-Us* 1994, 98, 4109-4117.
113. Chan, E. M.; Marcus, M. A.; Fakra, S.; ElNaggar, M.; Mathies, R. A.; Alivisatos, A. P. Millisecond kinetics of nanocrystal cation exchange using microfluidic x-ray absorption spectroscopy. *J Phys Chem A* 2007, 111, 12210-12215.
114. Sahu, A.; Kang, M. S.; Kompch, A.; Notthoff, C.; Wills, A. W.; Deng, D.; Winterer, M.; Frisbie, C. D.; Norris, D. J. Electronic impurity doping in CdSe nanocrystals. *Nano Lett* 2012, 12, 2587-2594.
115. Wang, L. F.; Rong, W. B.; Sun, L. N.; Chen, L. G.; Shao, B. Capillary forces between submillimeter spheres and flat surfaces at constant liquid volumes. *Chinese Phys Lett* 2009, 26.
116. Spinicelli, P.; Buil, S.; Quelin, X.; Mahler, B.; Dubertret, B.; Hermier, J. P. bright and grey states in CdSe-CdS nanocrystals exhibiting strongly reduced blinking. *Phys Rev Lett* 2009, 102.
117. Maier, S. A. *Plasmonics: Fundamentals and Applications*. 1st ed.; Springer: New York, 2007.
118. Lal, S.; Link, S.; Halas, N. J. Nano-optics from sensing to waveguiding. *Nat Photonics* 2007, 1, 641-648.

119. Bardhan, R.; Grady, N. K.; Halas, N. J. Nanoscale control of near-infrared fluorescence enhancement using Au nanoshells. *Small* 2008, 4, 1716-1722.
120. Haes, A. J.; Chang, L.; Klein, W. L.; Van Duyne, R. P. Detection of a biomarker for Alzheimer's disease from synthetic and clinical samples using a nanoscale optical biosensor. *J Am Chem Soc* 2005, 127, 2264-2271.
121. Link, S.; El-Sayed, M. A. Size and temperature dependence of the plasmon absorption of colloidal gold nanoparticles. *J Phys Chem B* 1999, 103, 4212-4217.
122. Michaels, A. M.; Nirmal, M.; Brus, L. E. Surface enhanced Raman spectroscopy of individual rhodamine 6G molecules on large Ag nanocrystals. *J Am Chem Soc* 1999, 121, 9932-9939.
123. Mock, J. J.; Barbic, M.; Smith, D. R.; Schultz, D. A.; Schultz, S. Shape effects in plasmon resonance of individual colloidal silver nanoparticles. *J Chem Phys* 2002, 116, 6755-6759.
124. Aizpurua, J.; Hanarp, P.; Sutherland, D. S.; Kall, M.; Bryant, G. W.; de Abajo, F. J. G. Optical properties of gold nanorings. *Phys Rev Lett* 2003, 90.
125. Halpern, A. R.; Corn, R. M. Lithographically patterned electrodeposition of gold, silver, and nickel nanoring arrays with widely tunable near-infrared plasmonic resonances. *Acs Nano* 2013, 7, 1755-1762.
126. Walsh, G. F.; Dal Negro, L. Engineering plasmon-enhanced Au light emission with planar arrays of nanoparticles. *Nano Lett* 2013, 13, 786-792.
127. Frens, G. Controlled nucleation for regulation of particle-size in monodisperse gold suspensions. *Nature-Phys Sci* 1973, 241, 20-22.

128. Ivanov, M. R.; Haes, A. J. Anionic functionalized gold nanoparticle continuous full filling separations: Importance of sample concentration. *Anal Chem* 2012, 84, 1320-1326.
129. Haiss, W.; Thanh, N. T. K.; Aveyard, J.; Fernig, D. G. Determination of size and concentration of gold nanoparticles from UV-Vis spectra. *Anal Chem* 2007, 79, 4215-4221.
130. Zeng, Y.; Grandner, S.; Oliveira, C. L. P.; Thunemann, A. F.; Paris, O.; Pedersen, J. S.; Klapp, S. H. L.; von Klitzing, R. Effect of particle size and Debye length on order parameters of colloidal silica suspensions under confinement. *Soft Matter* 2011, 7, 10899-10909.
131. Chen, J. X.; Liao, W. S.; Chen, X.; Yang, T. L.; Wark, S. E.; Son, D. H.; Batteas, J. D.; Cremer, P. S. Evaporation-induced assembly of quantum dots into nanorings. *Acs Nano* 2009, 3, 173-180.
132. de Abajo, F. J. G.; Howie, A. Retarded field calculation of electron energy loss in inhomogeneous dielectrics. *Phys Rev B* 2002, 65.
133. Myroshnychenko, V.; Rodriguez-Fernandez, J.; Pastoriza-Santos, I.; Funston, A. M.; Novo, C.; Mulvaney, P.; Liz-Marzan, L. M.; de Abajo, F. J. G. Modelling the optical response of gold nanoparticles. *Chem Soc Rev* 2008, 37, 1792-1805.
134. Dombi, P.; Horl, A.; Racz, P.; Marton, I.; Trugler, A.; Krenn, J. R.; Hohenester, U. Ultrafast strong-field photoemission from plasmonic nanoparticles. *Nano Lett* 2013, 13, 674-678.

135. Radha, B.; Kulkarni, G. U. Dewetting assisted patterning of polystyrene by soft lithography to create nanotrenches for nanomaterial deposition. *Acs Appl Mater Inter* 2009, 1, 257-260.
136. Nirmal, M.; Dabbousi, B. O.; Bawendi, M. G.; Macklin, J. J.; Trautman, J. K.; Harris, T. D.; Brus, L. E. Fluorescence intermittency in single cadmium selenide nanocrystals. *Nature* 1996, 383, 802-804.
137. Cordero, S. R.; Carson, P. J.; Estabrook, R. A.; Strouse, G. F.; Buratto, S. K. Photo-activated luminescence of CdSe quantum dot monolayers. *J Phys Chem B* 2000, 104, 12137-12142.
138. Liu, L. P.; Peng, Q.; Li, Y. D. An effective oxidation route to blue emission CdSe quantum dots. *Inorg Chem* 2008, 47, 3182-3187.
139. Peterson, J. J.; Krauss, T. D. Photobrightening and photodarkening in PbS quantum dots. *Phys Chem Chem Phys* 2006, 8, 3851-3856.
140. Yu, W. W.; Qu, L. H.; Guo, W. Z.; Peng, X. G. Experimental determination of the extinction coefficient of CdTe, CdSe, and CdS nanocrystals. *Chem Mater* 2003, 15, 2854-2860.
141. Medintz, I. L.; Mattoussi, H. Quantum dot-based resonance energy transfer and its growing application in biology. *Phys Chem Chem Phys* 2009, 11, 17-45.
142. Zenkevich, E.; Cichos, F.; Shulga, A.; Petrov, E. P.; Blaudeck, T.; von Borczyskowski, C. Nanoassemblies designed from semiconductor quantum dots and molecular arrays. *J Phys Chem B* 2005, 109, 8679-8692.

143. Zenkevich, E. I.; Sagun, E. I.; Knyukshto, V. N.; Stasheuski, A. S.; Galievsky, V. A.; Stupak, A. P.; Blaudeck, T.; von Borczyskowski, C. Quantitative analysis of singlet oxygen (O-1(2)) generation via energy transfer in nanocomposites based on semiconductor quantum dots and porphyrin ligands. *J Phys Chem C* 2011, 115, 21535-21545.
144. Jiang, J.; Bosnick, K.; Maillard, M.; Brus, L. Single molecule Raman spectroscopy at the junctions of large Ag nanocrystals. *J Phys Chem B* 2003, 107, 9964-9972.
145. Clark, A. W.; Cooper, J. M. Optical Properties of Multiple-Split Nanophotonic Ring Antennae. *Advanced Materials* 2010, 22, 4025-4029.
146. Hao, F.; Nordlander, P.; Sonnefraud, Y.; Van Dorpe, P.; Maier, S. A. Tunability of subradiant dipolar and fano-type plasmon resonances in metallic ring/disk cavities: Implications for nanoscale optical sensing. *Acs Nano* 2009, 3, 643-652.
147. Nordlander, P. The Ring: A Leitmotif in plasmonics. *Acs Nano* 2009, 3, 488-492.
148. Lahiri, B.; Holland, G.; Aksyuk, V.; Centrone, A. Nanoscale imaging of plasmonic hot spots and dark modes with the photothermal-induced resonance technique. *Nano Lett* 2013.
149. Wang, H.; Wu, Y. P.; Lassiter, B.; Nehl, C. L.; Hafner, J. H.; Nordlander, P.; Halas, N. J. Symmetry breaking in individual plasmonic nanoparticles. *P Natl Acad Sci USA* 2006, 103, 10856-10860.